



MEMS Floating Element Sensor Array for Wall Shear Stress Measurement under a Turbulent Boundary Layer

A dissertation submitted by

Zhengxin Zhao

in partial fulfillment of the requirements for the degree of

Doctor of Philosophy
in
Mechanical Engineering

Tufts University

February 2014

© 2014, Zhengxin Zhao

Adviser: Robert D. White

Abstract

A MEMS floating element shear stress sensor array has been designed as a $1\text{ cm} \times 1\text{ cm}$ chip. The array consists of 256 individual floating elements which are separated into 16 groups with a pitch of approximately 2 mm . Bumps were included on the surface of the device in order to increase interaction with the flow. Although this does increase hydrodynamic forces, it appears to primarily increase pressure gradient sensitivity rather than shear stress sensitivity.

The device was fabricated on a glass substrate using four layers of surface micromachining including copper & nickel electroplating. The chips were packaged either in a ceramic package or on a printed circuit board. A capacitance to voltage readout and a capacitance to digital converter IC were used to measure the differential capacitance change resulting from flow forces.

The sensors chips with half the elements acting in parallel were flushed mounted into the flow channels of a laminar flowcell at Tufts University and an indraft windtunnel at the NASA Ames Research Center. Experimental characterization of a chip in a ceramic package determined that the sensitivity to shear stress was 77 aF/Pa . The achieved resolution was limited by white noise with a level of 0.24 Pa/rtHz at low frequencies (below 1.5 Hz), and linearity was demonstrated to larger than 13 Pa . A second sensor packaged in a printed circuit board was tested under a turbulent boundary layer in the

indraft windtunnel. The sensor sensitivity was 90 aF/Pa , and resolution was 1 Pa/rtHz at low frequencies (below 1.5 Hz). Orientation dependence of the sensor output was verified, demonstrating the ability to measure direction as well as magnitude of the shear stress.

In addition to the demonstration of a MEMS shear stress sensor array, a major finding of this work is that pressure gradient sensitivity for these devices can be high. An experimental methodology was conceived and demonstrated that allows independent determination of pressure gradient and shear stress sensitivity. It is particularly important to accurately measure pressure gradient effects when calibrating these devices in a laminar flow cell. If this effect is neglected the calibrated shear stress sensitivity may exhibit large errors. For the device described here, neglecting pressure gradient effects would lead the researcher to erroneously conclude that sensitivity is 173 aF/Pa , rather than the correct value of 77 aF/Pa .

Acknowledgements

First of all, I would like to thank my advisor, Professor Robert White. Four year ago, he opened a door to me when I got lost. Because of him, I find what I am interested in and have started a very attractive and challengeable research. His professional guidance has a significant impact on the various aspects, including the plentiful technical skills as well as the personalities. What is more important is that, I have concluded that MEMS is what I love to devote in the future, indeed.

Second, I would like to thank Spirit AeroSystems, Inc [Wichita, KS] for supporting this project financially, and specifically thank Judy Gallman for the help at the contract extension, patent filing, and spending numerous hours on the monthly teleconference for the project progress.

I would also like to thank the other two Professors, Professor Bebrouz Abedian at Mechanical Engineering and Professor Sameer Sonkusale at Electrical and Computer Engineering, to serve as the committee members, recommendations on the research work and review this dissertation.

Next, I would like to thank everybody in our research group, Joshua Krause, Shuangqin (Susan) Liu, Minchul Shin, John Burns, Eric Schmitt, etc. They are resourceful co-workers and wonderful friends. They have helped me in the different period of time and different areas since my first day joining the group.

Additionally, I would like to thank a large number of people at 200 Boston Ave, Anderson hall, and Bray laboratory who have assisted me. For instance, the microfab users at Tufts MicroNano Fab, Jim Hoffman (machine shop coordinator), Lorin Polidora (ME Administrator), and other ME/EE graduate students.

I finally would like to thank my family, specially my parents, and my girlfriend. Their persistent support and loves throughout my educational pursuit have meant a lot to me and driven to me to success.

In the end, I offer my regards and blessings to all of those who supported me any time during the process.

Contents

Abstract.....	ii
Acknowledgements.....	iv
Chapter 1 Introduction.....	1
1.1 Contribution.....	3
1.2 Thesis Overview.....	4
Chapter 2 Background.....	6
2.1 Shear Stress Measurement.....	7
2.1.1 Non-MEMS Technology.....	7
2.1.2 MEMS Technology.....	12
2.2 Turbulent Boundary layer.....	25
2.2.1 Turbulence Boundary Layer Thickness.....	25
2.2.2 Drag Coefficient and Skin Friction Coefficient.....	27
2.2.3 Kolmogorov Microscales.....	28
Chapter 3 Design.....	30
3.1 Physical Description.....	31
3.2 Sensor Model and Design.....	33
3.2.1 Mechanical modeling.....	33
3.2.2 Electrostatic modeling.....	38
3.2.3 Electromechanical modeling.....	41
3.2.4 Bump Design and Modeling.....	41
3.2.5 Array Design.....	44
3.3 Fluid Force Modeling.....	46
Chapter 4 Fabrication.....	49
4.1 Metal Layers.....	50
4.2 Sacrificial Layer.....	54
4.3 Structure_1 Layer: Floating Element.....	61
4.4 Structure_2 Layer: Bump.....	68
4.5 Dice and Release.....	71
4.6 Dimple Layer (optional).....	74

4.7	SEM Images	76
Chapter 5	Packaging	80
5.1	Packaging	81
5.1.1	CPGA Packaging Process	81
5.1.2	PCB Packaging Process	86
5.2	Electronics	94
5.2.1	MS3110	94
5.2.2	AD7747	97
5.2.3	Microcontroller and DAC	98
5.2.4	AD7745	100
5.3	Probe Assembly	102
Chapter 6	Characterization	105
6.1	Electromechanical Calibration	106
6.1.1	LDV Measurement	106
6.1.2	C-V Measurement	108
6.2	Laminar Flow Test.....	110
6.2.1	Flowcell Design	110
6.2.2	Experimental Setup	115
6.2.3	Flow Measurement.....	120
6.2.4	Shear Stress Measurement	133
6.3	Turbulent Boundary Layer Test.....	138
6.3.1	Experimental Setup	138
6.3.2	Shear Stress Measurement	140
Chapter 7	Conclusion	146
7.1	Hardware Contributions	147
7.2	Operational Conclusions	148
7.3	Future Work.....	150
7.3.1	Design	151
7.3.2	Fabrication.....	155
7.3.3	Packaging	156
7.3.4	Characterization	157
7.3.5	Feedback control	158
Appendix A	Mask Layout	159
Appendix B	Fabrication Runsheet.....	162
Appendix C	CAD Drawing.....	166
Appendix D	CPGA Pinout	168
Bibliography	170

List of Figures

Figure 2.1. The Pitot tubes plugged into the flow channel [11].....	8
Figure 2.2. (Top) Schematic of oil film Interferometry setup [14]. (Bottom) Interferograms of an oil film thinning beneath a turbulent boundary layer [2].....	11
Figure 2.3. (Left) “Classical” fence sensor with a fence fully connected to the body. (Right) Fence sensor connected to the body by two beams [21].....	15
Figure 2.4. (Top) Top view and cross-sectional view of first MEMS-based floating element sensor by Schmidt et al. (Bottom) Schematic illustration of differential capacitance readout [22].....	17
Figure 2.5. Schematic diagram illustrating the photodiode floating element sensing principle by Padmanabhan et al [32].	18
Figure 2.6. Top view of floating element with comb fingers by Pan et al [23].	20
Figure 2.7. Schematic top view of the cantilever-based floating element by Zhe et al [26].....	21
Figure 2.8. Schematic top view geometries of the differential capacitive shear stress sensor by Chandreskaran et al [27]	22
Figure 2.9. Schematic turbulent boundary layer over a flat plate [35]	26
Figure 3.1. Diagram of the mechanical structure of the floating element sensor.	32
Figure 3.2. Schematic in-plane motion of floating element: (left) initial position and (right) deflected.	32
Figure 3.3. Diagram of mechanical model of floating element.	34

Figure 3.4. (Left) Deflection shape of the folded-beam suspension; (Right) Schematic bending moment diagram of the top beam.....	34
Figure 3.5. FEA simulation and of a floating element at COMSOL model	36
Figure 3.6. Schematic description of flow velocity profile and shear stress on Couette flow [39].	37
Figure 3.7. The change of electric field after the movable finger displaces by Δx into the slot.	39
Figure 3.8. Capacitance between two fingers: (left) COMSOL model of electric field including fringe field, (right) fringe effect on the change of capacitance (right).	40
Figure 3.9. COMSOL model: (top) 3D velocity profile of laminar duct flow, (middle) 2D velocity profile along the bump, (bottom) pressure distribution around the bump.	42
Figure 3.10. Layout of the 1 cm^2 array chip. 256 elements are arranged into 16 groups of 16 elements. Each group is independently addressable.	45
Figure 3.11. Simple model of the flow interaction with the shear sensor including pressure gradient and surface shear.	47
Figure 4.1. (Left) Fabrication process of metal layer: schematic in side view and (right) microscope images from top view.	53
Figure 4.2. Over developing of liftoff resist caused AZ9245 peeled off.	55
Figure 4.3. Misalignment due to twice sacrificial layer lithography.	56
Figure 4.4. The holder for wafer and anode sheet in the plating solution.	58
Figure 4.5. Fabrication process of sacrificial layer: schematic in sideview (left) and microscope images from top view (right).	60
Figure 4.6. Edge bead of AZ9260 at a spin speed of 1500 rpm.	62
Figure 4.7. Layout design of edge bead removal (EBR) mask.	62
Figure 4.8. Surface profiles of wafer edge after the two different edge bead removals: (top) acetone swab and (bottom) EBR mask exposure/developing.	63

Figure 4.9. Photoresist of comb finger at the different exposure time and same developing time: exposure time goes from short to long from (a.1) to (a.4).	64
Figure 4.10. (Top) Fabrication process of floating element layer: schematic in side view and (bottom) microscope images from top view.	67
Figure 4.11. The photoresist did not spread out uniformly on $8\mu m$ floating element structure of the wafer edge.	69
Figure 4.12. (Top) Fabrication process of bump layer: schematic from side view and (bottom) microscope images from top view.	70
Figure 4.13. After releasing, (top) schematic in sideview and (bootom) overview of a group of floating element with bump.	73
Figure 4.14. Explanation of interface reaction between Ti and Au caused by the nickel plating process.	73
Figure 4.15. Schematic of fabrication process of dimple layer.	75
Figure 4.16. SEM images of a released sensor chip: multiple elements in one group, a single element, a beam attached to anchor with an air gap underneath, comb fingers, and a bump (from first to end).	79
Figure 5.1. Schematics of CPGA used in MEMS floating element shear stress sensor (measurements are in inches). [Specturm Semiconductor Materials, San Jose, CA].	82
Figure 5.2. (Left) A finished sensor chip packaged and potted in a ceramic pin grid array package. A dashed line indicates the line along which a stylus profilometer scan was taken. (Right) The measured height of the surface topology along the indicated scan line.	84
Figure 5.3. Schematics and photos of the CPGA packaging process	85
Figure 5.4. The situations of using different viscous epoxy as adhesion to the MEMS chip: (a) over fill, (b) full fill, (c) under fill.	88
Figure 5.5. A photo of conductive ink drawing setup [42].	89
Figure 5.6. Surface profile at the cross-section of a conductive ink line [42].	91
Figure 5.7. (Left) Conductive ink connections of two pads and (right) an	

overview of a completed PCB package.	92
Figure 5.8. PCB packaging process using conductive ink: (left) cross-section schematics and (right) photos from top view.	93
Figure 5.9. (Top) Front and back photos of the MS3110 electronics board and (bottom) schematic of MEMS chip and MS3110 chip system. ...	95
Figure 5.10. Photos of AD7747 electronics printed circuit board.	98
Figure 5.11. Readout electronics used an AD7747 capacitance to digital converter to perform differential capacitance measurements on the MEMS chip. Communication was via I2C to a microcontroller which then communicates over USB.	99
Figure 5.12. Interface of the box with the microcontroller and DAC board inside.	100
Figure 5.13. Front and back side of the circular AD7745 electronics	102
Figure 5.14. Assembly of MEMS chip and AD7745 electronics into an Al tube as small as possible.	104
Figure 6.1 Displacement response of a single floating element using Laser Doppler Vibrometry and first four modal frequencies are found.	107
Figure 6.2. The change of capacitance as a function of driven voltage on one side of one floating element group.....	109
Figure 6.3. A schematic of a disassembled Flowcell.	110
Figure 6.4. Diagram of the laminar flow cell test apparatus.....	111
Figure 6.5. (Top) Measured pressure as a function of distance down the duct for different flow rates in the $h_f = 0.30 \text{ mm}$ high duct. (Bottom) Measured pressure gradient as a function of flow rate (symbols) compared to the Poiseuille flow model (lines), Eq. (6.6), plotted for the three duct heights.....	114
Figure 6.6. The laminar flow experimental setup of the MS3110 electronics: (top) inside faraday cage, (bottom) outside faraday cage.....	116
Figure 6.7. The laminar flow experimental setup of AD7747 electronics: (top)	

inside faraday cage, (bottom) outside faraday cage.....	118
Figure 6.8. (Top) the sensor is flush mounted on a plate and modeling clay seals the edges, and (bottom) entire setup for the probe sensor.	119
Figure 6.9. Measurement of 10 groups of floating element sensor arrays on a CPGA with MS3110 electronics in the 0.30 mm high laminar flowcell: (a) time domain voltage data at each flow rate, (b) change of voltage averaged at each flow rate in one cycle with linear fitting, (c) repeatability in five cycles, (d) and converted capacitance plot according to the MS3110 transfer function.....	123
Figure 6.10. Flow rate measured in the digital flow controller response from 0 CFH to 40 CFH in steps of 5 CFH.....	125
Figure 6.11. Measurement of 8 groups of floating element sensor arrays on a CPGA with AD7747 electronics in the 0.30 mm high laminar flowcell: (a) time domain capacitance data at each flow rate, (b) change of capacitance averaged at each flow rate in one cycle with linear fitting, and (c) repeatability in five cycles.	128
Figure 6.12. Measurement of the probe sensor (8 active groups) with AD7745 electronics in the 0.30 mm high laminar flowcell: (a) time domain capacitance data at each flow rate, (b) change of capacitance averaged at each flow rate in one cycle with linear fitting, and (c) repeatability in five cycles.	131
Figure 6.13. Measured change in capacitance vs. flow rate for all three channel heights. Best-fit lines are also shown.....	134
Figure 6.14. Comparison of shear stress measured by the MEMS sensor (y-axis) to shear stress computed from the volume flow rate (x-axis). All 24 non-zero flow conditions are plotted as open circles. The dashed line is the unit line, indicative of an accurate measurement. The plot on the left assumes no pressure gradient sensitivity. The plot on the right corrects for the pressure gradient using the measured sensitivity as in Eq. (6.11) and (6.12).	135

Figure 6.15. Photographs of the flow facility and the test section. (Top) The MEMS sensor is flush mounted in a nickel painted acrylic plate in the floor of the test section, 65 *cm* from the end of the contraction. (Bottom) A pitot probe is used to measure the free stream velocity and boundary layer profile. 139

Figure 6.16. The top panels in each plot show the free stream velocity measured by the pitot/static probe. The bottom panels show a comparison between the measured shear stress from the MEMS sensor, and the shear stress computed from the velocity using the correlation (a) MEMS sensor oriented with the flow. (b) MEMS sensor oriented opposite to the flow direction. (c) MEMS sensor oriented in the cross-flow direction. 143

Figure 7.1. (Left) Current floating element. (Right) New floating element design: a straight capacitor substitutes the comb finger..... 151

Figure 7.2. (Left) 25 μm gap between neighbor elements in current group layout. (Right) New group design with all elements connected laterally..... 154

Figure 7.3. Fabrication improvement at the sacrificial layer: reduce one lithography step..... 155

Figure 7.4. (Left) Prediction of pressure gradient and (right) shear stress as a function of flow rate at 0.2 *mm* duct height. 158

Figure 7.5. Separation of comb finger for the feedback control application. 158

List of Tables

Table 2.1 Comparison of the floating element shear stress sensors discussed above	24
Table 2.2. Typical situation of a commercial airliner in cruise	29
Table 3.1. Sensitivity effect of the bump of 20 μm diameter and 12 μm height in the laminar duct flow below 40 <i>CFH</i> flow rate.	43
Table 3.2. Design dimensions of the floating element with bump sensor array-on-a-chip.....	44
Table 4.1. Design and as-manufactured dimensions of the floating element with bump sensor.	76
Table 6.1. Characterization comparison of various packaging and electronics schemes at the labminal flowcell test.	132
Table 6.2. Flow conditions for tunnel testing: The measured flow speed is shown. The predicted skin friction and boundary layer thickness are computed using $1/7^{\text{th}}$ power law correlations.	140

Chapter 1

Introduction

The measurement of wall shear stress is important in many flow testing and device applications. Examples include drag measurement on air, space, land, and transportation vehicles both in test environment such as wind tunnels, and in operation.

The cost of fuel is, by far, the most significant expenditure when considering total aircraft operating costs. As the price of fuel increases, the percentage of the total cost that it represents increases as well. In an aircraft, drag is overcome by thrust which is provided by burning fuel. If the drag is reduced, the required fuel burn will decrease. Aerodynamic drag is also a significant factor in a car's ability to accelerate. At very high speed, the ratio of the engine's power output to the body's drag becomes more important than the power-to-weight ratio, which is important at lower speeds where drag is not significant. Assuming that that car has a certain engine, the only way to increase the top speed would be to improve the aerodynamics by reducing the skin-friction. Furthermore, much effort has been devoted to pressure

measurement in wind tunnel testing and/or airfoil research, viscous drag, however, has not received the same level of attention. This has resulted, in part, from our inability to quickly and accurately measure skin friction [1-6].

The measurement of surface shear stress is also important in industrial flow applications for fluid handling and manufacturing operations such as extrusion, and for biomedical devices in such applications as tissue engineering, where tissue development may depend on local shear stress. For instance, a flow chamber that is able to generate a controlled wall shear stress, has been designed and used to study the effect of hemodynamic forces on the vascular endothelial structure and cellular function in blood flow [7].

Flow regimes of interest may be as diverse as subsonic and supersonic turbulent boundary layer, turbulent pipe flows, and laminar flow in micro-channels. Skin-friction is always a critical parameter to the fundamental understanding of turbulent flow, and for design. A turbulent boundary layer over a flat plate will occur usually when Reynolds number is larger than 5×10^5 . For very high Reynolds numbers, the Kolmogorov microscales characterize the smallest scales of turbulence. Their length and time scales are typically on the order of micron and microsecond [8], which will require the precise spatial and time resolutions on the measurement sensors. For some applications, particularly in turbulent boundary layer flows for aeroacoustic and structural acoustic applications, it may be important to capture the fluctuating shear stresses as well as the mean.

1.1 Contribution

This thesis has resulted in several advances compared to the existing technologies, related to shear stress sensor design, sensor fabrication, and turbulent boundary layer characterization as discussed below.

1) Array

A unique topology of 16 separately addressable arrays on a chip increases system robustness and opens the possibility of measurement of the spatial variation of shear with approximately 2 *mm* spatial resolution.

2) Accuracy

Shear stress measurement error associated with pressure gradients in the flow has been noted by some authors in the recent decade [1] but not quantified. As far as we are aware, this research gives the first result experimentally distinguishing the shear stress and pressure gradient effects for a floating element sensor. The characterization of the sensitivity to pressure gradient should be considered whenever the calibration of a MEMS floating element sensor is attempted.

3) Packaging

The designed sensor has been fabricated and packaged in a low cost, easily implemented process that reduces the package dimensions and the required infrastructure. The essential package is a small cylinder with 25 *mm* diameter and 13 *mm* height, including the MEMS chip on the top side and the electronics circuit with a signal output connector on the bottom side. This

probe configuration is one of highest “technology readiness level” shear stress sensor in existence so that it can be easily incorporated into a large number of flow facilities for flow characterization. This is close to being a product.

4) Fabrication

It is the first time that the MEMS shear stress has been fabricated on a glass substrate rather than silicon. The major advantage is the reduction in parasitic capacitance, which may be less than 10% that observed on a silicon substrate. Low parasitic capacitance is expected to reduce the noise level and improve the signal-to-noise ratio (SNR). The use of nickel surface micromachining on a glass substrates for shear sensor fabrication is unique in the literature [2].

1.2 Thesis Overview

This thesis is organized into seven chapters and four appendices. Chapter 1 introduces the motivations and contributions of the thesis project. Chapter 2 reviews the milestones on the road to wall shear stress measurement technologies since 1950, and explains their basic principles and characteristics. It also contains fundamental background on turbulent boundary layers and turbulence which are directly relevant to the measurement targets. Chapter 3 describes the design and mechanical/electrostatic/fluidic modeling of the floating element with surface bumps. Chapter 4 introduces the four layer

nickel surface micromachining. SEM images showing the smallest features and the complete released structure are also presented. Chapter 5 addresses a traditional ceramic packaging method and a unique probe packaging method, as well as their own advantages and disadvantages. Chapter 6 is focused on the characterization, and consists of three parts: (a) calibration of the mechanical and electrical properties, such as the vibration measurement and electrostatic driving, (b) laminar flow testing at Tufts University, (c) turbulent boundary layer testing in the wind tunnels at NASA Ames research center. Chapter 7 summarizes the thesis work, reviews the major contributions and lists the possible directions of future research.

Chapter 2

Background

Chapter 2 has two sections. Section 1 broadly reviews the existing significant technologies for wall shear stress measurement, as well as elaborating the technique (floating element) used in this dissertation. The second section briefly introduces turbulent boundary layer (TBL) theory, and three critical characteristics relevant to measurement: boundary layer thickness, drag coefficient, and Kolmogorov microscales.

2.1 Shear Stress Measurement

Much research has been devoted to development of wall shear stress measurement over the past six decades. The section will review two non-MEMS techniques and three MEMS-based techniques.

2.1.1 Non-MEMS Technology

The major examples of non-MEMS technology include the Pitot tube and oil film interferometry.

2.1.1.1 Pitot Tube

The Pitot tube was invented by the French engineer, Henri Pitot, in the early 18th century, and then was modified into numerous convenient forms to measure the flow pressure and velocity. Between 1920 and 1960, Stanton tube [9] and Preston tube [10] made use of a pitot tube resting on the flow boundaries and measuring the skin friction. In operation, pitot tubes are located on the boundary facing the flow as shown in Figure 2.1, and a series of the dynamic pressure measured by a head tube, which is correlated with the shear stress. The relation between pressure and shear stress is given by [4]:

$$\frac{\Delta p}{\tau_w} = f\left(\frac{U_\infty \cdot D}{\nu}\right) \quad (2.1)$$

where Δp is the pressure difference, τ_w is the shear stress, U_∞ is the free stream velocity, D is the outer diameter of round pitot tube, ν is the kinematic viscosity of flow, f is the calibration function determined by tube experiments.

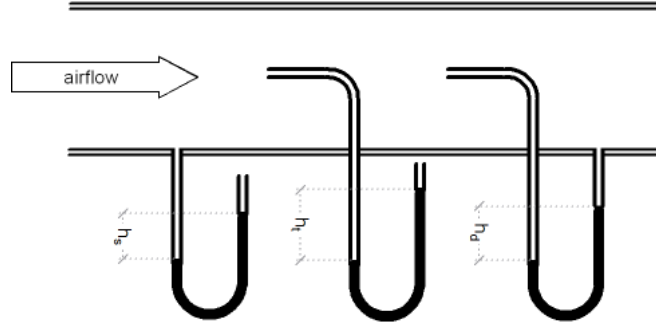


Figure 2.1. The Pitot tubes plugged into the flow channel [11]

In measurement of turbulent boundary layer (TBL) over a flat plate (TBL will be mentioned at the section 2.2), the pitot tube are used to measure the velocity profiles at the multiple locations along the flow direction, the momentum θ and displacement thicknesses δ^* can be computed using [12],

$$\theta = \int_0^{\delta} \frac{u}{U_e} \left(1 - \frac{u}{U_e} \right) dy \quad (2.2)$$

$$\delta^* = \int_0^{\delta} \left(1 - \frac{u}{U_e} \right) dy \quad (2.3)$$

where δ is the turbulent boundary layer thickness (see section 2.2.1), u is the flow velocity using pitot tube, U_e is the edge velocity, y is the distance perpendicular to the flat surface. Then, the surface skin friction as well as the shear stress can be deduced using the momentum integral equation [12],

$$\frac{\tau_w}{\rho U_e^2} = \frac{C_f}{2} = \frac{d\theta}{dx} + \frac{1}{U_e} \frac{dU_e}{dx} (2\theta + \delta^*) - \frac{v_w}{U_e} \quad (2.4)$$

where τ_w is the wall shear, ρ is the density, U_e is the edge velocity, C_f is the skin friction coefficient, v_w is the mass flow through the wall for transpiration flows, and x is the distance along the surface.

Pitot tube is an easy way to set up and measure the wall-shear stress and has been used until now. However, there are some disadvantages of pitot measurement.

- a) The head of tube has to be immersed into the flow region and facing the flow direction to let the flow go inside of a tube, thus, the tip may cause flow disturbances.
- b) The similarity of flow region along the channel is a critical assumption. Actually, the real variation of flow is able to produce the difference on the function f each time. That is why the pitot technique has been recognized as a reliable method only in smooth boundaries.
- c) In order to measure a pressure or velocity profile along one direction, any small misalignment of a set of pitot tubes is able to generate an error on the result.
- d) Spatial and temporal resolutions (e.g. response time) are also the challenges.

2.1.1.2 Oil Film Interferometry

The oil film interferometry (OFI) has been used to measure skin friction since 1975 [13], but was developed to gain wide-scale acceptance and simple form around 1993 at NASA Ames research center [14]. OFI relies on the principle that the thinning rate of a thin oil film on a surface, when subjected to shear, is

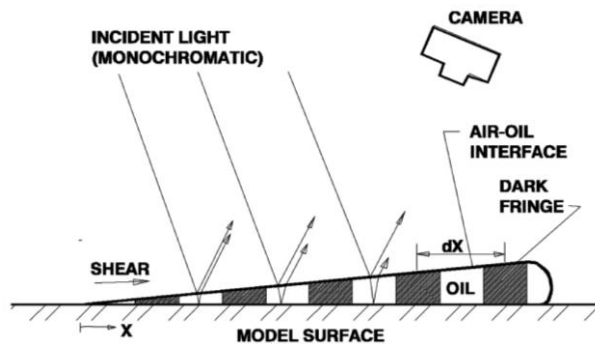
a function of to the magnitude of the shear stress. Therefore, the measurement to shear involves measuring the oil thickness gradient, as well as logging the history of tunnel run conditions, and knowing the properties of the oil.

It is illustrated that, in Figure 2.2, the interference between the partially reflected light at the air-oil interface and the light reflected from the model surface will vary between constructive and destructive as the oil film thickness changes. The spacing of the series of light and dark bands or fringes as shown at the bottom image of Figure 2.2 is proportional to the skin friction.

The governing equation between oil thickness and shear stress is given as

$$\frac{\partial h}{\partial t} + \frac{\partial}{\partial x} \left(\frac{\tau_{w,x} h^2}{2\mu_{oil}} \right) + \frac{\partial}{\partial z} \left(\frac{\tau_{w,z} h^2}{2\mu_{oil}} \right) = 0 \quad (2.5)$$

where h is the oil thickness, t is time, x and z the orthogonal surface coordinates, μ_{oil} is the oil dynamic viscosity. Where Eq. (2.5) is derived in [2]. Figure 2.2 also indicates the essential components of image-based OFI system, included a light source, an oil film, a detector (a camera in the figure), and a suitable model surface.



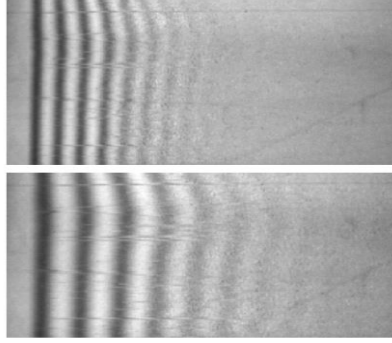


Figure 2.2. (Top) Schematic of oil film Interferometry setup [15]. (Bottom) Interferograms of an oil film thinning beneath a turbulent boundary layer [2]

A significant amount of work has been expended on the implementation of oil film interferometry, such as laser interferometry skin friction (LISF) technique, fringe imaging skin-friction (FISF) technique, and surface imaging skin-friction (SISF) technique. There are some advantages of OFI: in particular, a broad two or three dimensional region of skin friction, and improved spatial resolution (at the pixel level). However, some drawbacks exist [2].

- a) Surface requirement: model surface must be reflective and rough surfaces are unsuitable as well.
- b) Temporal resolution. Oil film interferometry technique requires an amount of time to acquire data over a region and process the data, which reflects the poor temporal resolution and is not susceptible to transient condition. Typically, flow is steady for a time on the order of 1 to 10 minutes, the model must be carefully photographed, and then post processing can be a lengthy process. Thus, only mean

shear is extracted, and only after substantial post processing.

- c) Optical access will be a challenge for the application to flight test experiments.

2.1.2 MEMS Technology

With the advent of microelectromechanical systems (MEMS), a number of sophisticated shear stress sensors have been developed which, in some cases, overcome the lack of spatial and temporal resolution of traditional technologies. MEMS-based hot-wire, surface fence, and floating element sensors are the major examples. These techniques will be reviewed in this section.

MEMS techniques for sensing skin friction are typically classified into two categories: indirect and direct measurement. Briefly speaking, indirect measurement means that the shear stress estimate is extracted from the change of a physical property of the flow, but does not directly measure forces on the wall. For example, hot film sensors are sensitive to the heat flow or temperature, and optical sensors can track modifications to a laser light source to detect motion in the region of interest. On the contrary, the direct measurement sensors respond to momentum transfer, that is, force, at the wall. Typically, the force is determined by measuring deflection (such as floating element), bending, or twisting of a structure. This motion or stress/strain could be measured piezoresistively, piezoelectrically, optically, magnetically, or electrostatically. In this work, we focus on electrostatic sensing, where a

pair of moving plates produce a change in capacitance. The magnitude of the capacitance change directly depends on the magnitude of the force on the structure, and therefore the shear stress.

2.1.2.1 Hot film

Hot-wire as a typical indirect technique has been used for many years, even earlier than MEMS technique exists. However, MEMS-based hot wire/film sensors [16-18] are more accurate and disturb the flow less because of the smaller size. The operation principle of hot wire sensor is that the heat transfer from a heated source to the flow adjacent to the heated region depends on the flow characteristics. The sensor normally consists of a thin conducting (metal, doped silicon, etc) film placed on a substrate, and is flush-mounted to a wall. During operation, the thin film is electrically heated to a temperature greater than the fluid temperature. The heat generated goes convectively from the film to the flow passing over the film, and the change of temperature ΔT is a function of the film resistance [2]:

$$\Delta T = \frac{R_r - R_s}{\alpha R_r} \quad (2.6)$$

where R_r is the resistance at a reference temperature, R_s is the resistance of hot-film, α is the thermal coefficient resistance. A widely used formula relating the hot film and to shear stress is represented by [19]

$$\frac{P}{\Delta T} = A\tau^{1/3} + B \quad (2.7)$$

where P is the power dissipated in the hot film, A and B are the calibration constants.

Hot film technology is able to simultaneously measure the fluctuating shear stress at a small region and be insensitive to alignment of sensor to flow direction (which is also a drawback). However, the limitations are stated as follows [1].

1. Temperature drifting causes a measurement error.
2. Relationship between shear stress and change of temperature is not unique.
3. Reduction in sensitivity and complications in the dynamic response due to the frequency-dependent conductive heat transfer into the substrate.
4. It has no ability to distinguish flow direction.

2.1.2.2 Surface Fence

The surface fence sensor is another indirect measurement of wall shear stress. The sensor usually consists of a flexible thin silicon plate (fence) contacting with a silicon base. As flow impinges against the fence, a bending stress is created. The piezoresistors are placed on the locations of the highest stress and connected to a Wheatstone bridge. Thus, the stress changes the electrical resistance of piezoresistors. The output voltage of the Wheatstone bridge is a measure of the wall shear stress.

All fences were designed similarly across variant variety of researchers, however, Papen et al [20, 21] has reported a stepped fence. In order to concentrate the stress, a central and rectangular slit is cut from the base and

the base is only fixed to the edges (see Figure 2.3). A slot window near a body yields a better sensitivity and resolution than a simple rectangular shape fully connected to the body. The increased surface area results in greater stress and larger sensitivity. All surface fence sensors were fabricated using bulk micromachining on a silicon substrate, and the piezoresistors were fabricated by ion implantation. In 2012, the fence sensor of Savelsberg et al [20] was attached in a cylindrical body with a printed circuit board, which sits inside another larger cylindrical housing to allow an adjustable protruding height. The advantages of this particular package are a) to adapt to the thickness of viscous sublayer of turbulent boundary layer and b) to concentrate the stress due to pressure difference at the base. One drawback of all surface fences is poor spatial resolution because of larger surface area, whose length is typically order of 5-10 *mm*. In addition, as with other indirect sensors, the fence does not respond to shear but to forces generated by flow over the roughness, resulting in calibrations depend on the type of flow being explored.

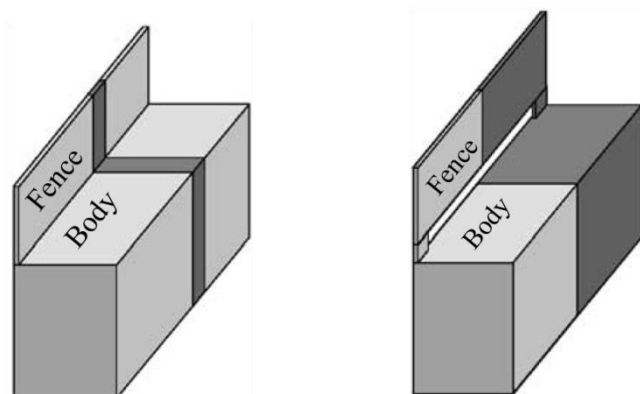


Figure 2.3. (Left) “Classical” fence sensor with a fence fully connected to the body. (Right) Fence sensor connected to the body by two beams [22].

2.1.2.3 Floating element

Floating elements are another approach to the wall shear stress measurement. In this technology, a micromachined plate or shuttle is suspended using micromachined beam tethers. Under the influence of hydrodynamic forces, this “floating element” experiences a lateral deflection. The motion may be detected using capacitance change [23-29], piezoresistance [30, 31], or optical method [32-34]. A number of authors have described these devices in the past.

The earliest work on MEMS floating elements is that of Schmidt et al in 1988 [23]. In Figure 2.4, the sensor is comprised of one shuttle and four tethers as a spring, was fabricated using a Polyimide surface micromachining process on a silicon substrate. Three passivated electrodes are located on the surface of the wafer and a thin conductor is embedded in the floating element. Three parallel plate capacitors are capable to detecting the motion of shuttle. The sense capacitances C_{ps1} and C_{ps2} vary linearly with element deflection as well as wall shear stress, and the changing is measured off-chip using a pair of transresistance amplifiers. For calibration, the sense chip was packaged on a Lucite with epoxy to create a large sensor plate, which assembled with another u shape shim plate and top cover plate to form a flow channel. The first floating element of a differential capacitive scheme performed the linear response to the shear stress up to 12 Pa in the laminar flow, while the resonant frequency and the noise floor were not reported. One drawback of this

packaging process is that the sensor was permanently attached on the Lucite plate every time when it had been calibrated.

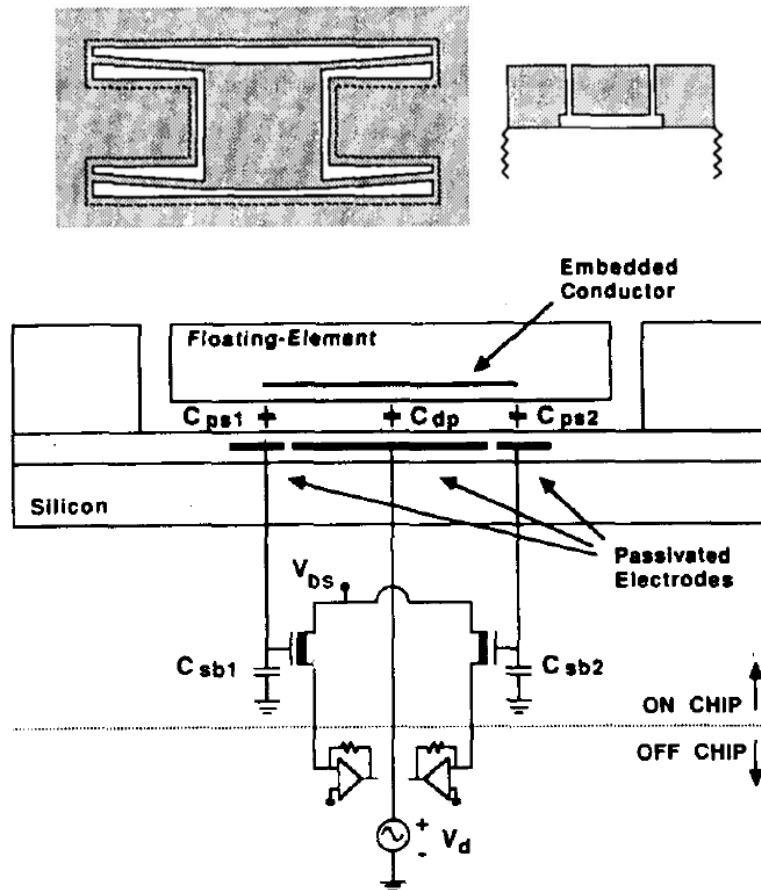


Figure 2.4. (Top) Top view and cross-sectional view of first MEMS-based floating element sensor by Schmidt et al. (Bottom) Schematic illustration of differential capacitance readout [23].

Between 1995 and 1997, major contributions were made by Padmanabhan et al [32-34] with the introduction of the photodiode detection method. Two photodiodes are designed under the floating element which is same as Schmidt in 1988. As shown in Figure 2.5, the sensor is subjected to uniform illumination from a laser source. The photodiodes are able to sense the position of the leading and trailing edges of the center shuttle since the change of exposed area to the incident light results the differential photocurrent.

And the photocurrent is proportional to the magnitude of wall shear stress. This sensor was fabricated using bulk micromachining and wafer bonding process. This unique photodiode optical floating element was reported of a resolution of 10 mPa and the maximum tested shear of 0.9 Pa in the laminar flow cell and a laminar boundary layer of the wind tunnel. A single point was recorded by the research group demonstrating linearity to 10 Pa . Because the optical floating element relies on that there are the same incident light densities for two photodiodes. It has, in fact, an inevitable problem of a non-uniform incident illumination in a high-speed turbulent flow of the change of flow temperature, which is a big issue for the measurement experiments.

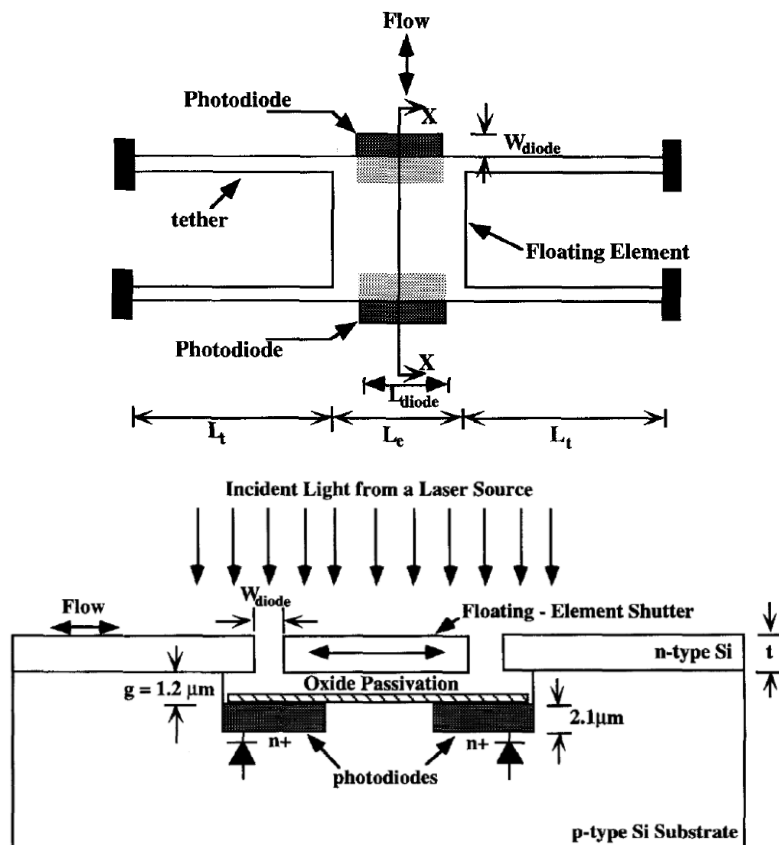


Figure 2.5. Schematic diagram illustrating the photodiode floating element sensing principle by Padmanabhan et al [33].

Two years later (1999), Pan et al, Hyman et al, and Patel et al first introduced the comb finger into the floating element shown in Figure 2.6 to sense the differential capacitance instead of embedded conductor in 1988 [23], which reduced the complexity of fabrication. From that on, the variable and in-plane parallel plates became the common sensing scheme for the future capacitive floating elements, included this thesis work. The principle is based on that a deflection of the floating element in flow direction changes the overlap area between two fingers as well as the capacitance. Sensed differential capacitance between top and bottom combs is proportional to shear stress. More details will be presented in chapter 3. The sensor was fabricated using polysilicon surface micromachining process and packaged with on-chip electronics for force rebalancing [24-26]. Linear response characterized in the laminar flow channel is demonstrated out to 4 Pa (non-linearity occurred at 5 Pa). It was the large promotion to the floating element.

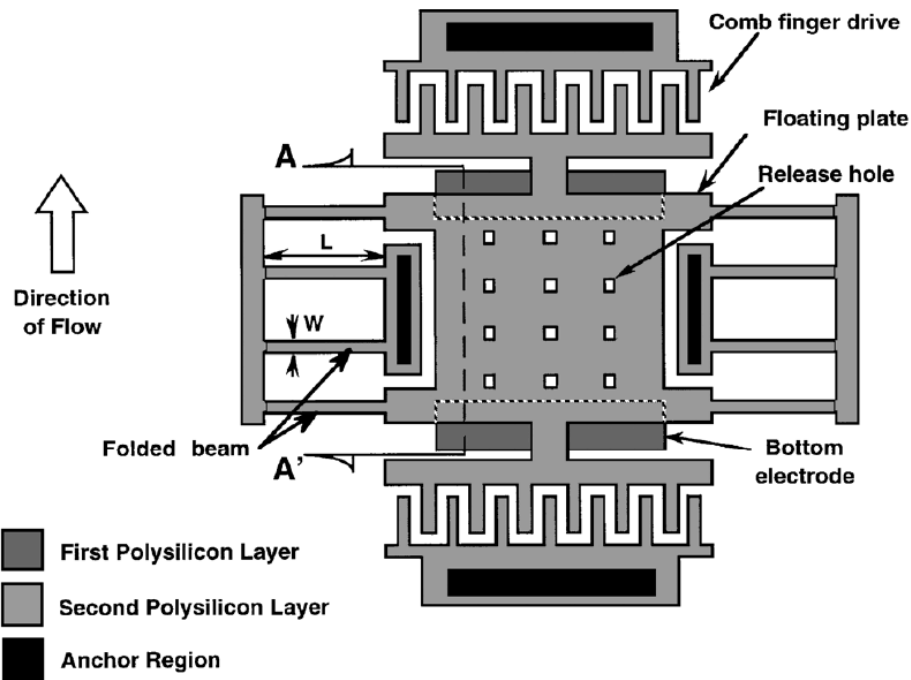


Figure 2.6. Top view of floating element with comb fingers by Pan et al [24].

In more recent work, a cantilever-based floating element was designed by Zhe et al [27]. The design modifies the traditional floating element by replacing the tether beams on the two sides with a long cantilever beam on one side of shuttle. It is another differential capacitive floating element, the change to capacitance, however, is linear to shear stress as long as the deflection is much smaller than the gap t in Figure 2.7. The fabrication process is similar in [33]. MS3110 capacitance readout circuit sensing the change in the differential capacitance achieves $0.04 Pa$ resolution at stresses up to $0.2 Pa$ in a laminar duct flow.

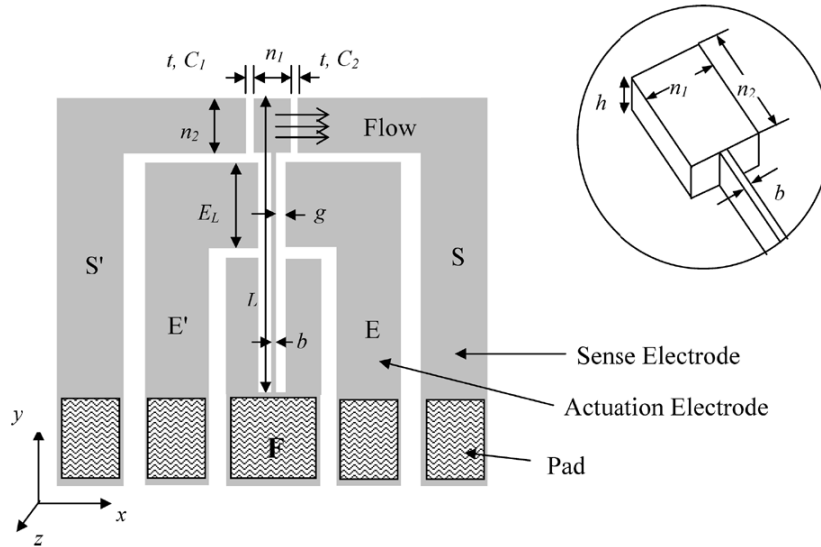


Figure 2.7. Schematic top view of the cantilever-based floating element by Zhe et al [27].

In 2000, Chandreskar, et al [28, 29] also used differential capacitive floating element measurement. The structure difference is to align the comb finger perpendicular to flow direction so that the fingers move in a side way and change the gap rather than overlap length. The calibration is focusing on oscillating shear stress in an acoustic plane wave tube (PWT), and dynamic measurement demonstrated the resolution as high as $15 \mu Pa$ at $1 kHz$ band with linear response up to $1.9 Pa$. It has accomplished nearly highest dynamic range of $102 dB$ over the existing floating element devices.

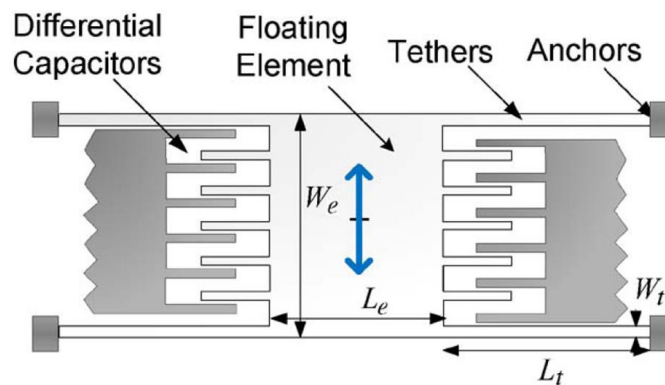


Figure 2.8. Schematic top view geometries of the differential capacitive shear stress sensor by Chandreskaran et al [28]

Notable work by Shajii, et al [30] and Barlian, et al [31] describe the piezoresistive floating elements for measurement in liquid where the other floating element sensors are unsuitable to operate. Both of them have a very similar structure as earliest one [23]. In 1992, Shajii's floating element has been calibrated at high shear stress up to 12 *kPa*, and able to survive at higher stress 100 *kPa* and high temperature between 190°C to 200°C more than 20 hours. When 2007, Barlian et al [31] have designed, fabricated another piezoresistive shear stress for underwater application. More efforts have been devoted on the calibration and de-couple of shear stress (in-plane) and the normal stress (out-of-plan), as well as temperature coefficient of sensitivity. Sensitivity amplification and the reliability were the tasks in future work.

The floating element techniques discussed are summarized and listed in Table 2.1.

MEMS floating elements have the advantages of ease of use, high spatial and temporal resolution, and are a “direct” measurement technology insofar as they respond to momentum transfer at the wall. However, MEMS floating element sensors do suffer from some drawbacks [1].

- a) A potential for sensitivity to pressure gradients
- b) Difficulties with misalignment
- c) Tradeoff between spatial resolution and mean shear stress

- d) Environment effects (temperature, humidity, etc)
- e) A possible lack of robustness to water or particle impingement

Table 2.1 Comparison of the floating element shear stress sensors discussed above

Research group	Schmidt [23]	Shajii [30]	Padmana bhan [33]	Pan [24, 25]	Zhe [27]	Barlian [31]	Chandreskaran [28]
Year	1988	1992	1996	1999	2005	2007	2011
Sensing mode	Capacitance	Piezoresistive	Photodiode	Capacitance	Capacitance	Piezoresistive	Capacitance
Test environment	Laminar flow	Liquid	Laminar flow	Laminar flow	Laminar flow	Arbitrary force	Laminar flow Acoustic wave
Output sensitivity	0.47 mV/Pa	13.7 μ V/V-kPa	0.3 V/Pa	1.02 V/Pa	0.34 mV/Pa	50 μ V/Pa	7.66 mV/Pa
Linearity	12 Pa	12 kPa	0.9 Pa	3.6 Pa	0.2 Pa	0.8 Pa	1.9 Pa
Resolution/ Noise floor			0.01 Pa		0.04 Pa	3.2 mPa	14.9 μ Pa
Dynamic range	40 dB ²		40 dB	37 dB	14 dB	48 dB	102 dB
Spatial resolution	500 μ m	140 μ m	500 μ m	100 μ m	500 μ m	500 μ m	2 mm
Temporal resolution			16 KHz	16 KHz	531 Hz	19 KHz	6.2 KHz

2.2 Turbulent Boundary layer

This section will give a brief introduction of the fundamentals of turbulent boundary layer (TBL) pertaining to understanding of the floating element shear stress sensor in this dissertation. The overview will start with TBL thickness and drag coefficient, followed by the turbulent length and time microscales.

2.2.1 Turbulence Boundary Layer Thickness

Figure 2.9 illustrates a free stream flow is coming at a uniform free stream speed of U_∞ and moving over a flat plate. The boundary layer (between the blue cure and the plate surface) will develop and boundary layer thickness will grow as the boundary layer moves down to the plate.

At the leading edge, it starts at a laminar boundary layer, which is relative thin. Within it, pressure and shear stress are steady and easily predictable. At some point, it grows to a transition region and quickly becomes a thicker turbulent boundary layer (TBL) with all kinds of complicated vorticities and eddies, and the pressure and shear stress are no long steady, but begin fluctuating strongly in space and time. For a flat plate with zero pressure gradient, the TBL thickness δ , defined as the distance from the plate at which the mean velocity is 99% of the free stream velocity, can be estimated from the correlation [35]

$$\delta = 0.382 \frac{x_d}{\text{Re}_x^{0.2}} \quad (2.8)$$

where Reynolds number $Re_x = \rho U_\infty x_d / \mu$, x_d is the distance downstream from the leading edge, ρ is density of flow, μ is dynamic viscosity of the fluid. Looking at the cross-section of TBL, there is a thin viscous sublayer in contact with the plate surface where the viscous effect dominates and the turbulent fluctuations are damped out. In this region, the flow profile and properties are very similar with laminar flow. The thickness is about five wall units, where a wall unit U_T is defined as

$$U_T = \frac{\mu}{\sqrt{\rho \tau_w}} \quad (2.9)$$

For instance, a free stream velocity of approximately 250 m/s (Mach 0.8), typical of commercial airliner, in air with sound speed 300 m/s, at a density of 0.4 kg/m^3 and a dynamic viscosity of $1.5 \times 10^{-5} \text{ Pa s}$ (approximate properties at a cruise altitude of 10 km), shear stress $\tau_w = 40 \text{ Pa}$, thus, the Reynolds number is 7×10^6 and $\delta = 16 \text{ mm}$ at $x_d = 1 \text{ m}$, also, the wall unit is $4 \mu\text{m}$, so the viscous sublayer thickness is 20 m . The viscous sublayer thickness is a target for the maximum roughness of the MEMS sensor.

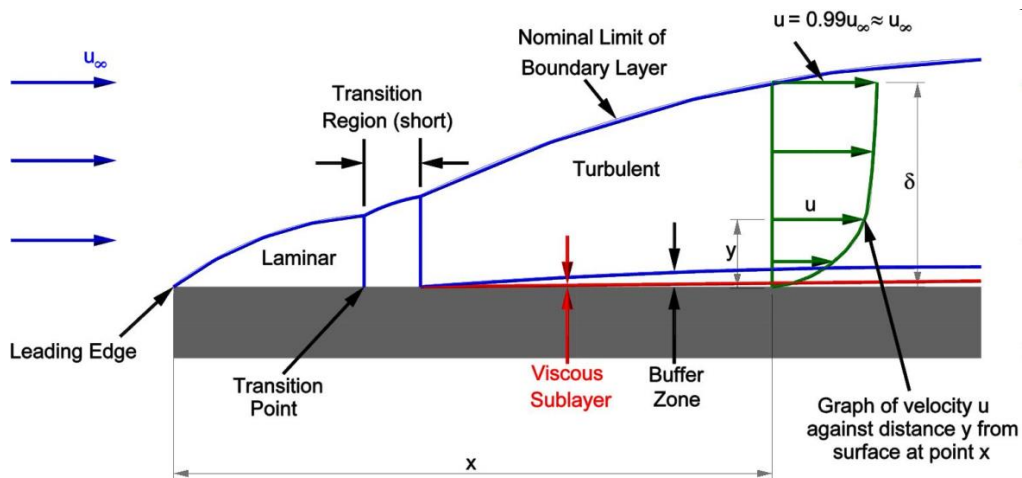


Figure 2.9. Schematic turbulent boundary layer over a flat plate [36]

2.2.2 Drag Coefficient and Skin Friction Coefficient

Two nondimensional parameters are used to express shear forces on an object.

The drag coefficient, C_d , is a dimensionless quantity used to quantify the mean drag force on an object in a flow environment. It is given by

$$C_d = \frac{F}{0.5\rho U_\infty^2 A_p} \quad (2.10)$$

where F is total drag force, A_p is projected frontal area. It is useful to predict how large the time averaged drag force is going to be on a given object. The drag coefficient will be a function of the shape of the object and the flow speed. The total drag includes not only contributions from shear stress (also called skin friction) but also includes effects from pressure differentials in front of and behind an object (termed form drag), and, at high speeds where portions of the flow become transonic, wave drag.

The skin friction component itself can be locally quantified using the skin friction coefficient. This is defined as the local shear stress divided by the dynamic pressure. For an incompressible, zero pressure gradient flat plate TBL, C_f can be estimated using 1/7th power law [37]:

$$C_f = \frac{0.027}{\text{Re}_x^{1/7}} = \frac{\tau_w}{0.5\rho U_\infty^2} \quad (2.11)$$

At the same condition as above, drag coefficient $C_f = 0.0032$. However, compressibility effects at high subsonic Mach numbers will reduce the friction factor by approximately 10% [37], assuming there is not a great deal of heat transfer from the wall to the flow. These results are consistent with recent oil

film measurements on a 2.7% scale model of a commercial airliner, the common research model, conducted in the NASA Ames 11 foot transonic tunnel under similar Mach and Reynolds number conditions to those experience in commercial flight. Measured values of C_f on the majority of the wing, tail, and body varied from approximately 0.002 to 0.004 [38].

2.2.3 Kolmogorov Microscales

The turbulent boundary layer is composed of many different sizes of eddies. The large eddies are unstable and eventually break down to the smaller eddies, and these smaller eddies undergo the same process, giving rise to even smaller eddies, and so on. In this way, the kinematic energy cascades down from the largest scale eddies to the smallest scale eddies where the energy is rapidly dissipated. This smallest scale of interest is introduced as Kolmogorov microscale. At the Kolmogorov scale, energy is rapidly dissipated by viscous effects. Hence, not eddies exist as scales smaller than these. Kolmogorov length and time scales are estimated, according to dimensional analysis, by

$$\eta = \left(\frac{\nu^3}{\varepsilon} \right)^{1/4} \quad (2.12)$$

$$\gamma = \left(\frac{\nu}{\varepsilon} \right)^{1/2} \quad (2.13)$$

where η is the Kolmogorov length scale, and γ the Kolmogorov time scale. The kinematic viscosity is $\nu = \mu / \rho$, and ε is the rate of turbulent energy dissipation per unit mass. Using dimensional analysis, ε scales as the ratio

of free stream velocity cubed to TBL thickness,

$$\varepsilon \propto \frac{U_\infty^3}{\delta} \quad (2.14)$$

In the same example as above, of $U_\infty = 250 \text{ m/s}$ and $\delta = 16 \text{ mm}$, η and γ are therefore approximate $2.7 \text{ }\mu\text{m}$ and $0.2 \text{ }\mu\text{sec}$ ($\sim 5 \text{ MHz}$). A shear stress sensor capable of detecting all aspects of unsteady shear at the wall would need to achieve this spatial and temporal resolution. This will prove to be extremely challenging. However, a sensor that can detect some portion of the spectrum of the spatial and temporal variation will still be useful.

Table 2.2. Typical situation of a commercial airliner in cruise

Symbol	Property	Value	Unit
	Altitude	10	<i>km</i>
ρ	Air density	0.4	<i>kg/m³</i>
c	Speed of sound	300	<i>m/s</i>
U_∞	Airspeed	240	<i>m/s</i>
Ma	Mach number	0.8	<i>dimensionless</i>
Re	Reynolds number	7×10^6	<i>dimensionless</i>
q	Dynamic pressure ($\rho U_\infty^2/2$)	12	<i>kPa</i>
μ	Dynamic viscosity	1.5×10^{-5}	<i>Pa s</i>
τ_w	Wall shear stress	40	<i>Pa</i>
δ	TBL thickness	16	<i>mm</i>
	Viscous sublayer thickness	20	<i>μm</i>
C_f	Skin friction coefficient	~ 0.003	<i>dimensionless</i>
η	Kolmogorov length scale	2.7	<i>μm</i>
γ	Kolmogorov time scale	0.2	<i>μsec</i>

Notation: All BL properties computed at $x_d = 1$ meter from the leading edge.

Chapter 3

Design

This chapter first covers the design and mathematical modeling of the MEMS-based floating element with bump shear stress sensor array. The second section discusses the fluid modeling, particularly in an attempt to distinguish pressure gradient and shear stress sensitivity.

3.1 Physical Description

The design of an individual floating element sensor in the array, shown in Figure 3.1, has many similarities to the sensor described in the previous chapter [24]. Each element has a movable center shuttle, two sets of comb fingers for differential capacitive sensing of the motion of the shuttle, and a series of folded beams.

- a) The center shuttle is the main body of the sensor, and physically experiences forces from interaction with the flow.
- b) The beams act as an elastic support, bending to allow the center shuttle to move in the plane of the device. The four inner beams are fixed to the substrate through the anchors. The reason to use a folded-beam rather than a tethered suspension is that the folded beam structure reduces the effects of residual stresses introduced during manufacturing [39]. Therefore, the stiffness of the structure is primarily determined by the beam's dimensions, and described later.
- c) The comb finger is comprised of a series of interdigitated parallel plates and utilized for sensing motion of the device. The inner combs attached to the center shuttle engage and disengage to the outer combs that are anchored down to a substrate (see Figure 3.2). Therefore, the sensor responds to a driving force and the change of capacitance between the comb fingers is related to the magnitude of force. More details are presented in the electrostatic model.

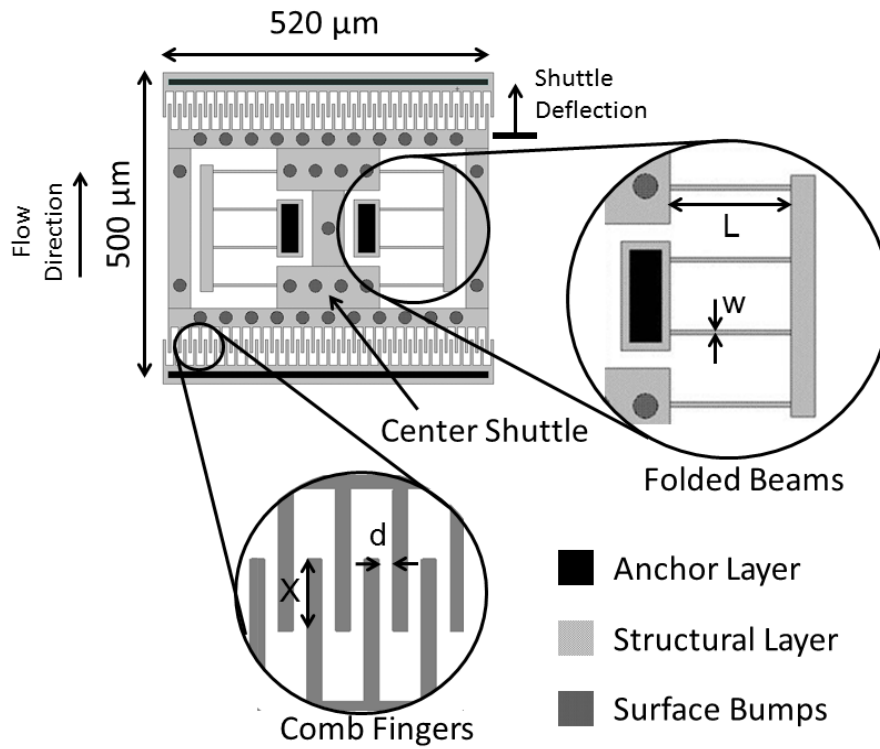


Figure 3.1. Diagram of the mechanical structure of the floating element sensor.

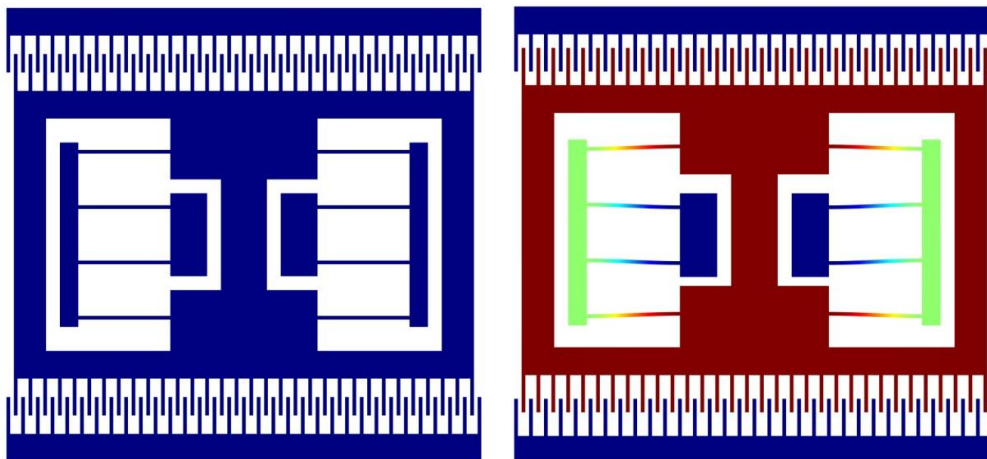


Figure 3.2. Schematic in-plane motion of floating element: (left) initial position and (right) deflected.

3.2 Sensor Model and Design

This section describes the mechanical and electrostatic modeling of the floating element, followed by the design of bump and array. From the model, the sensitivity to wall shear stress is defined and predicted.

3.2.1 Mechanical modeling

Referring to the physical description of the floating element above, a linear mechanical model has been developed based on several simplifying assumptions:

- a) The center shuttle is stiff, and can be considered as rigid body.
- b) Linear damping is assumed.
- c) The beams are lumped into single linear elastic springs.
- d) All beams are assumed to be identical.
- e) The connecting trusses between inner and outer folded beams are infinitely stiff. The assumption is valid for a small motion of center shuttle.

Taking these assumptions, the floating element is modeled as a mass damping mechanical system, shown in Figure 3.3. Inner beams acts in parallel and in series with outer beams. The stiffness of an individual beam and the floating element system and the air damping will be determined.

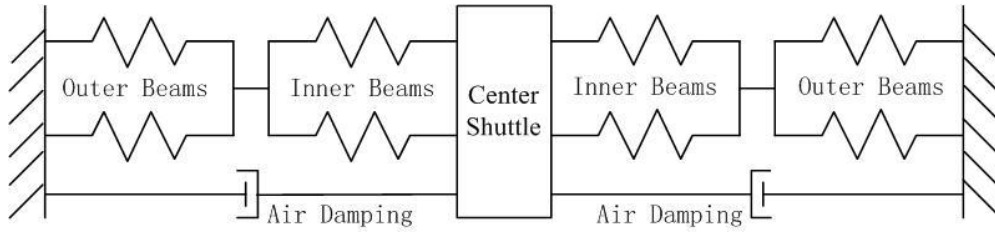


Figure 3.3. Diagram of mechanical model of floating element.

To apply a shear force F to the floating element will cause the beams to bend, resulting in a displacement U_c of the floating plate and deflection U_b of each beam in Figure 3.4. Since four beams are identical, the force acting on each beam

$$f = \frac{1}{4} F \quad (3.1)$$

and the deflections are the same that is

$$U_b = \frac{1}{2} U_c \quad (3.2)$$

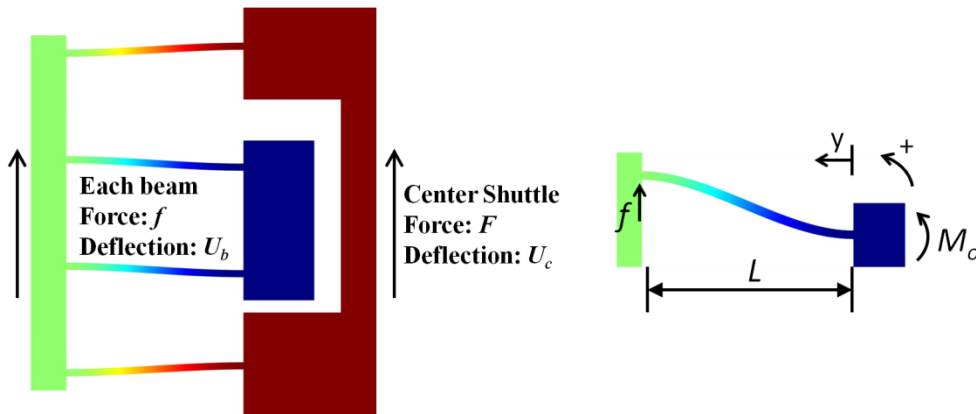


Figure 3.4. (Left) Deflection shape of the folded-beam suspension; (Right) Schematic bending moment diagram of the top beam.

Figure 3.4 presents the beam's bending moment diagram and the equilibrium of moment around the anchor yields

$$EI \frac{d^2u}{dy^2} = \sum M = -fy + M_o \quad (3.3)$$

where E is the Young's Modulus of beam, and I is the second moment of inertia of the beam, u is the displacement variable of the beam, y is the horizontal coordinate, M_o is the moment on the start of beam. Integrating Eq. (3.3) twice, we obtain,

$$EI \frac{du}{dy} = -\frac{1}{2}fy^2 + M_o y + C_1 \quad (3.4)$$

$$EIu = -\frac{1}{6}fy^3 + \frac{1}{2}M_o y^2 + C_1 y + C_2 \quad (3.5)$$

The boundary conditions at $y=0$ and $y=L$ are known by:

- a) Slope conditions: $\frac{du}{dx}|_{x=0} = 0$, and $\frac{du}{dx}|_{x=L} = 0$
- b) Deflection conditions: $y(0) = 0$, and $x(L) = U_b$

Applying the slope boundary conditions into Eq. (3.4), we have

$$C_1 = 0 \quad (3.6)$$

$$M_1 = \frac{1}{2}fL \quad (3.7)$$

Then, substituting Eq. (3.6) and (3.7) to Eq. (3.5) and applying deflection boundary conditions and, we have,

$$U_b = \frac{1}{12EI} fL^3 \quad (3.8)$$

Since the second moment of inertia of a rectangular area is defined by

$$I = \frac{1}{12}tw^3 \quad (3.9)$$

where t and w are the beam thickness and width, and the stiffness of each beam can be found as

$$k = \frac{f}{U_b} = Et\left(\frac{w}{L}\right)^3 \quad (3.10)$$

According to the relationships among eight identical beams, the global stiffness is predicted to be double of local:

$$K_x = 2k = 2Et\left(\frac{w}{L}\right)^3 \quad (3.11)$$

Then, the resonant frequency at the in-plane mode can be estimated using

$$f = \frac{1}{2\pi} \sqrt{\frac{K_x}{m}} \quad (3.12)$$

where m is the mass of center shuttle. FEA modeling is used to validate Eq. (3.12) and predict other modes at COMSOL Multiphysics. A 3D model of the floating element without comb finger is created and the Eigenvalues as well as the resonant frequencies are computed in vacuum condition (no air loading or electrostatics). The simulated results are shown in Figure 3.5.

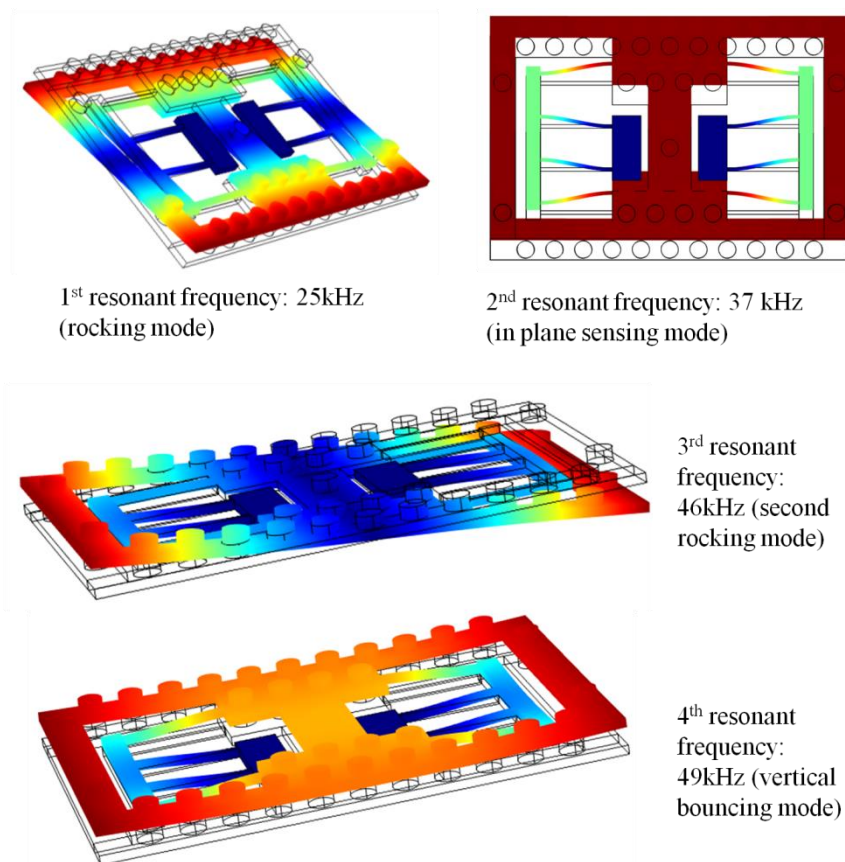


Figure 3.5. FEA simulation and of a floating element at COMSOL model

Theoretical 37.0 kHz from Eq. (3.12) is only 0.5% difference with simulated 37.2 kHz. The predictions are based on the manufactured dimensions shown in Table 3.2. In chapter 6, the experimental measurement will be introduced and compared with the simulation.

Damping is a second characteristic in a mathematical mechanical model and the damping in the floating element system is caused by the viscous drag. When the center shuttle is moving relative to the substrate, the flow between them is driven by viscous drag acting on the fluid and the applied pressure gradient parallel to the plates. If assuming that flow in the small gap is Couette flow, the cross-section profile flow is shown in Figure 3.6.

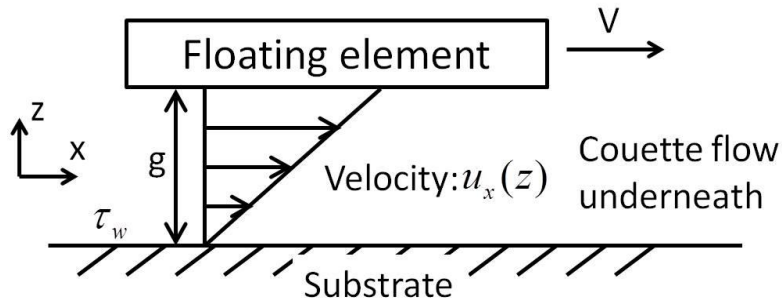


Figure 3.6. Schematic description of flow velocity profile and shear stress on Couette flow [40].

The shear stress in a Newtonian flow is given by

$$\tau = \mu \frac{\partial u_x}{\partial z} \quad (3.13)$$

where u_x is the flow velocity along the x-axis. Because of the small gap and the boundary conditions of $u_x(0) = 0$ and $u_x(g) = V$, the exact solution of shear stress becomes

$$\tau = \mu \frac{V}{g} \quad (3.14)$$

where, g is the gap between the floating element and the substrate.

In the mechanics model, the force F can be modeled as being proportional to the velocity V . The ratio between them is called the viscous damping coefficient, which is given by

$$b = \frac{F}{V} = \frac{\tau A}{V} \quad (3.15)$$

where A is the effective surface area corresponding to F . Substitute Eq. (3.14)

into Eq. (3.15) yields the damping of floating element

$$b = \mu \frac{A}{g} \quad (3.16)$$

However the damping is not critical in the static model, it plays a role in the velocity of center shuttle. The mechanical dynamic model in the direction along the comb finger would be written in the form of

$$m \frac{d^2 x}{dt^2} + b \frac{dx}{dt} + K_x x = F_x \quad (3.17)$$

where m is the mass of center shuttle, x and t are the movement and time variable, F_x is the total force applied on the center shuttle on the same direction.

3.2.2 Electrostatic modeling

Electrostatic model of floating element is essentially computed as the parallel plates. The parallel movement of the fingers changes the capacitance, as illustrated in Figure 3.7. The capacitance C of a single finger is defined as

$$C = 2 \frac{\epsilon t x}{d} = 2 \frac{\epsilon t}{d} (x_0 + \Delta x) \quad (3.18)$$

where ϵ is the permittivity of air, t is the finger thickness, d is the finger gap, x_0 is the inertial overlap length, Δx is the displacement of the movable finger. The total change of capacitance of one floating element is given by

$$\frac{\partial C}{\partial x} = 2N \frac{\epsilon t}{d} \quad (3.19)$$

where N the number of comb fingers on the shuttle.

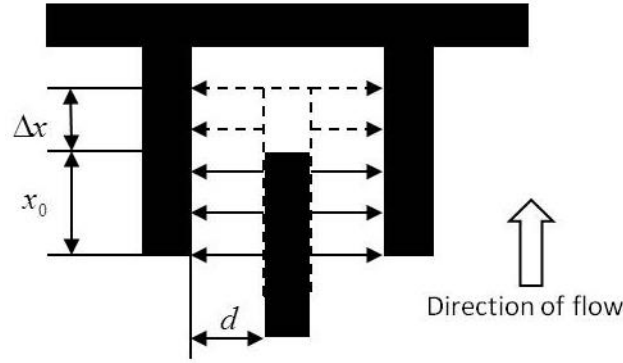


Figure 3.7. The change of electric field after the movable finger displaces by Δx into the slot.

The fringe effect has been considered and quantified using COMSOL Multiphysics. Since the fingers are all symmetric, the electrical region between two interdigitated fingers has been created, and the design geometry will be given in the next section. Left image in Figure 3.8 indicates the solution of electric potential distribution using 2D COMSOL Electrostatics model at the inertia position. Boundary conditions are set as follows: “Ground” at the boundaries of 1-3, “Terminal” at the boundaries of 5-7, and “Zero Charge” at the boundaries of 4 and 8. The free space is filled with air and meshed using extra fine triangular. Therefore, first, the total static

capacitance in the COMSOL model is about 3.8 pF and the theoretical capacitance with no fringe effect is 2.2 pF . It means static fringe capacitance is significant and approximate 68% of the parallel capacitance. However, if computing the change of capacitances (with fringe) while one finger is moving towards to the other one, it shows a great agreement between the COMSOL model and Eq. (3.19). There is only less than 5% disagreement on $\partial C / \partial x$ when a finger is moved within $1 \mu\text{m}$, as shown in right plot of Figure 3.8. The conclusion is that the fringe effect can be neglected here and the linear relationship of Eq. (3.19) is validated.

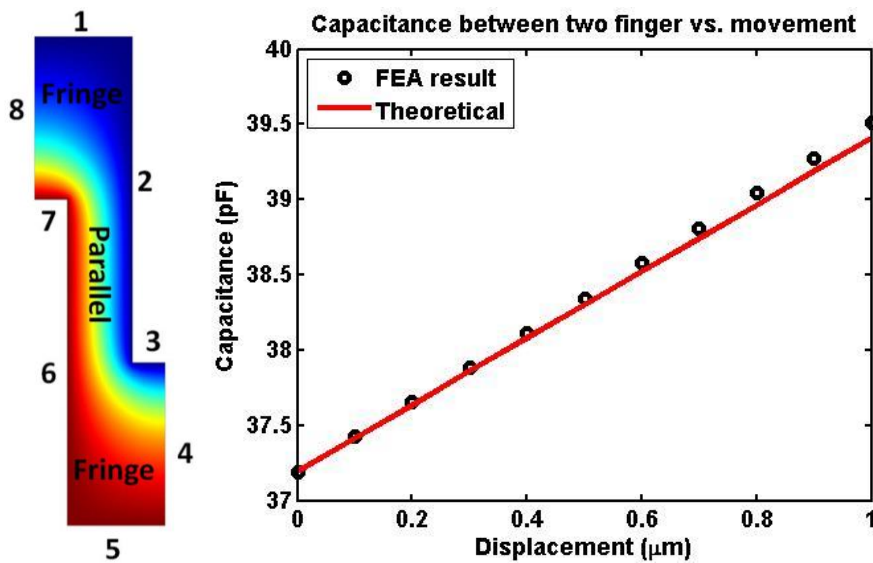


Figure 3.8. Capacitance between two fingers: (left) COMSOL model of electric field including fringe field, (right) fringe effect on the change of capacitance (right).

3.2.3 Electromechanical modeling

Eq. (3.11) expresses the mechanical property of the floating element in-plane direction and Eq. (3.19) describes the electrical energy of comb finger. Combination of these two is able to predict the electromechanical model from force to capacitance. The sensitivity S_I of the floating element to a constant applied force is thus:

$$S_1 = \frac{\partial C}{\partial F} = \frac{\partial C}{\partial x} \frac{\partial x}{\partial F} = \frac{\partial C}{\partial X} \frac{1}{K_x} = \frac{N\epsilon L^3}{Edw^3} \quad (3.20)$$

Eq. (3.20) is a fact if assuming the out-of-plane is infinitely stiff. In order to reduce out-of-plane motion, the aspect ratio (t to w) is desired as high as possible.

3.2.4 Bump Design and Modeling

In Figure 3.1, 35 cylindrical bumps, each $12 \mu\text{m}$ high with a diameter of $25 \mu\text{m}$, are designed in a distributed pattern on the top of floating element layer. One goal of adding the bumps is to increase the sensitivity, because more lateral force is expected due to the interaction of the flow with the rough surface. 3D COMSOL laminar flow model was used to predict the force generated on a half bump since it is symmetric. The steady, fluid dynamic simulation result is shown in Figure 3.9. In this simulation,

- a) a Poiseuille profile identical to that used in our laminar flow cell is introduced from the side,
- b) the pressure on the exit is zero,

- c) the symmetry boundary conditions are applied on two sidewalls along the flow stream line,
- d) the velocity on the top side is determined based on a Poiseuille profile,
- e) the steady flow is calculated using Navier-stokes with an incompressible, viscous Newtonian fluid model.

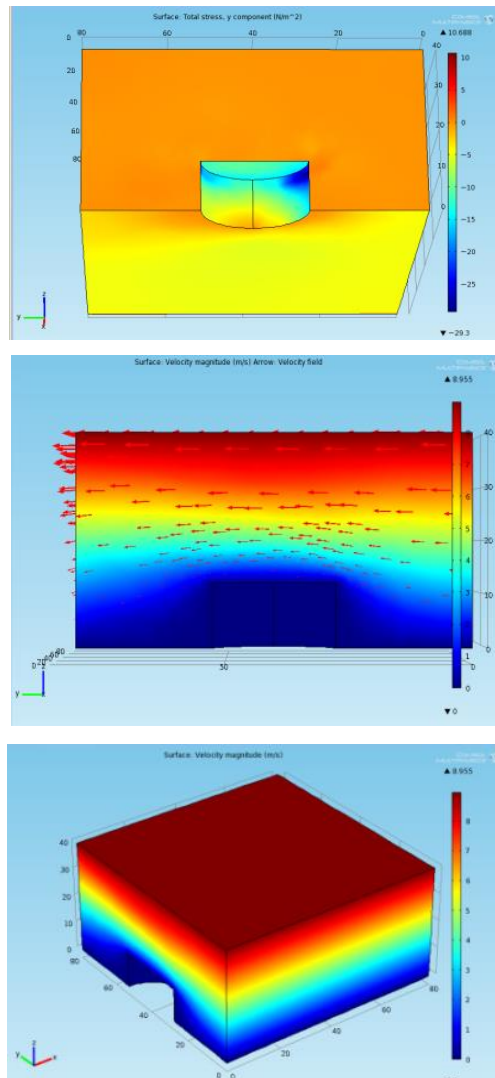


Figure 3.9. COMSOL model: (top) 3D velocity profile of laminar duct flow, (middle) 2D velocity profile along the bump, (bottom) pressure distribution around the bump.

The volume flow rates, Q , were swept from 5 *CFH* (cubic feet per hour) to 40 *CFH* at a step of 5 *CFH*. The surface integration of pressure gives the force over the half bump, f . The total force of 35 bumps, $F_2=2\ 35 f$. For the same conditions, the wall shear force on a non-bump-element, $F_1 =$ shear stress (τ) times surface area (A_m). Thus, the sensitivity increase of bump to non-bump can be estimated s as

$$s = \frac{F_1 + F_2}{F_1} \quad (3.21)$$

And, the simulation results are summarized in Table 3.1.

Table 3.1. Sensitivity effect of the bump of 20 μm diameter and 12 μm height in the laminar duct flow below 40 *CFH* flow rate.

Q (<i>CFH</i>)	f (<i>nN</i>)	F_2 (μN)	F_1 (μN)	s
5	21	0.15	0.14	2.1
10	44	0.31	0.27	2.1
15	68	0.48	0.41	2.2
20	94	0.66	0.55	2.2
25	122	0.85	0.69	2.2
30	150	1.05	0.83	2.3
35	180	1.26	0.97	2.3
40	212	2.49	1.11	2.3

Though, only 12 μm -high bumps were fabricated and tested, the ratio s will be increased to 3 or 11 as the height goes up to 20 or 50 μm . Also, this assumes that as flow increases, the ratio of force for flow around the bumps to force on the flat plate remains approximately the same. This is expected to be true for low flow rates where the Navier-Stokes equations are close to linear. However, at higher flow rates a separate flow calculation would need to be

done at each flow rate. And, once turbulent flow is established, a more sophisticated model would be required. The purpose of this calculation is primarily to provide a first estimate of the increase in sensitivity expected in the laminar flow test setup

So far, the design geometry for individual floating element with bumps shear stress sensor in the dissertation is given in Table 3.2.

Table 3.2. Design dimensions of the floating element with bump sensor array-on-a-chip.

Symbol	Property	Value	Units
d	Finger gap	4	μm
	Finger width	4	μm
N	Number of comb fingers on the shuttle	64	dimensionless
t	Thickness of structure	8	μm
w	Width of folded beam	4	μm
L	Length of folded beam	100	μm
H	Height of bump	12	μm
D	Diameter of bump	20	μm
g	Height of air gap below shuttle	5	μm
A_m	Shuttle top area (includes finger and shuttle top surface area)	0.085	mm^2

3.2.5 Array Design

Last portion of sensor design is “array”, which is another unique feature of this shear stress sensor. In anticipation of a future goal of measuring local spatial variation in unsteady shear, a number of the individual floating elements are electrically connected in parallel to become a single group. More groups have been designed to create even larger area of the surface sensors. A 1 cm

square MEMS sensor chip includes a 16×16 groups and each group consists of a 4×4 pattern of elements as shown in Figure 3.10.

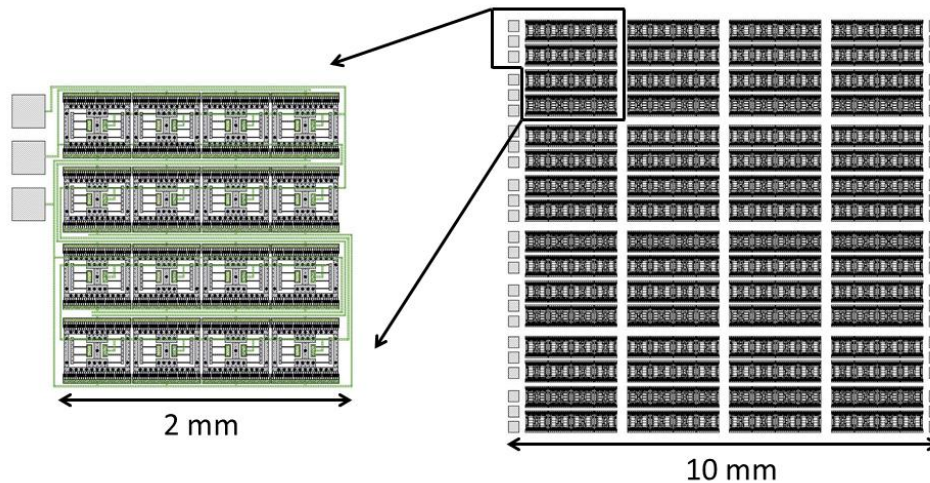


Figure 3.10. Layout of the 1 cm^2 array chip. 256 elements are arranged into 16 groups of 16 elements. Each group is independently addressable.

Each group has independent connections routed to three electrical pads for the top combs, bottom combs, and common (center shuttle) electrodes. The groups are approximately $2 \text{ mm} \times 2 \text{ mm}$ in size, thus the spatial resolution for shear measurements of the array-on-a-chip is on the order of 2 mm . The local shear stress of a group or average shear of the whole chip can be measured separately. This allows the end user to trade off between spatial resolution and sensitivity. In addition, a major benefit of the array architecture is that failure of a single element or single group, either during fabrication or during operation, does not destroy the functionality of the entire chip. This may be a highly desirable feature for sensors deployed in harsh operating environments where single elements may be lost to particulates or moisture, but the chip continues to function, albeit with reduced sensitivity.

3.3 Fluid Force Modeling

This section will introduce the fluid forces acting at the floating element in order to distinguish the shear stress and pressure gradient and drive their sensitivities. This modeling is the theory behind the calibration of shear stress in the later chapter.

The structure will respond to forces applied to the shuttle arising from interaction with the flow field. For a perfectly smooth shear sensor with no gaps or topology, the lateral force would simply be the surface area of the shuttle multiplied by the wall shear stress. Thus, some previous authors have assumed that the static force on the sensor would be

$$F \approx A_m \cdot \tau_{yx} \quad (3.22)$$

where τ_{yx} is the wall shear stress present at the wall in x-y coordinate. However, for a sensor that includes gaps, topology, roughness, and packaging topology, it is expected that the steady fluidic force may depend on both the time average local wall shear stress, the local streamwise pressure gradient in the flow, and the details of the geometry at the microscale. It is also possible that the compressibility of the flow may play a role, and, in the case of boundary layer flows, the boundary layer thickness may be important. A fully 3D numerical analysis coupled with a series of experiments is required to capture all the details of this interaction, as the local geometries are complex. Such an analysis is outside the scope of this dissertation, although it is being conducted in a parallel project. The only numerical flow work for a floating

element shear sensor of which we are aware is the conference paper by Chen and Reshotko [41], and recent work by our group [42]. As a first step towards a more comprehensive, but still experimentally tractable, flow interaction model, consider the sensor to have an effective rectangular shape, and to be acted on by the local surface shear stress and the pressure gradient present in the flow, as diagrammed in Figure 3.11.

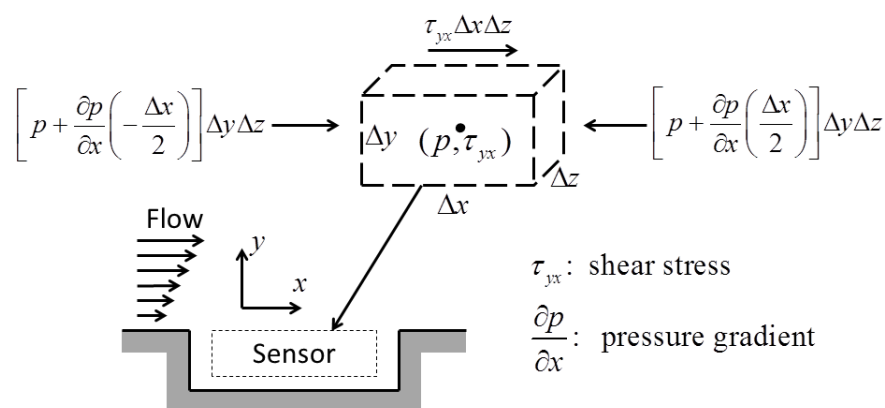


Figure 3.11. Simple model of the flow interaction with the shear sensor including pressure gradient and surface shear.

It is emphasized that the effective size of the element, Δx by Δy by Δz , is not identical to the physical size of the element. These effective dimensions will be determined experimentally, and, to first order, account for the unknown details of the microscale flow around the element. They can also account for small manufacturing nonuniformities or imperfect packaging, such as a slightly misaligned sensor. It is likely that these dimensions will be of the same order of magnitude as the physical size of the element. Given this model, the fluidic force acting on the element will be

$$F = \tau_{yx} \cdot \Delta x \Delta z - \left(\frac{\partial p}{\partial x} \right) \cdot \Delta x \cdot (\Delta y \Delta z) \quad (3.23)$$

By combining Eq. (3.20) and (3.23), the differential sensitivity of a single element to the two flow variables can then be written

$$S_2 = \frac{\partial C}{\partial \tau_{yx}} = \frac{\partial C}{\partial F} \frac{\partial F}{\partial \tau_{yx}} = \frac{N \varepsilon L^3}{Edw^3} \Delta x \Delta z \quad (3.24)$$

$$S_3 = \frac{\partial C}{\partial (\partial p / \partial x)} = \frac{\partial C}{\partial F} \frac{\partial F}{\partial (\partial p / \partial x)} = \frac{-N \varepsilon L^3}{Edw^3} \Delta x \Delta y \Delta z \quad (3.25)$$

where S_2 is the sensitivity to shear, and S_3 is the sensitivity to pressure gradient.

Chapter 4

Fabrication

This chapter introduces the procedure of the microfabrication of the floating element with bump shear stress sensor. The sensors were fabricated using a four-mask nickel surface micromachining process in the Tufts Micro/Nano Fab. Four masks process realizes a variety of structures, including Cr/Au interconnects, copper sacrificial layer, and two nickel structural layers (floating element and bump). The cartoons of cross-section and microscope images from top view corresponding to the steps are attached in the end of each section, to provide a better understanding of the process. SEM pictures are presented in last section to focus the detailed structure of floating element with bump sensor.

4.1 Metal Layers

The process starts with the insulating soda lime substrate of 100 ± 0.2 mm diameter, 550 ± 50 μm thick, rounded edges, and primary flat only. The lower parasitic capacitance is the primary reason we chose glass wafer instead of silicon wafer. A high power (200 watt) and low vacuum (300 mTorr) oxygen plasma at an oxygen flow rate of 100 sccm (standard cubic centimeters per minute) is used to clean the wafer for two minutes prior to the first layer. The plasma tool used over the procedure is “MARCH CS1701F Reactive Ion Etcher (RIE)”.

In the metal layer, 75/225 nm-thick Cr/Au metallization layer is deposited and patterned on the glass wafer.

Step (a) The wafer is center loaded on the chuck of “Laurell WS-400B-6NPP-Lite Manual Spinner”. A liftoff resist, “LOR-20B” [Microchem, Newton, MA], is spun on the wafer at 2000 rpm for 45 sec and soft baked at 200°C for 5 min. AZ9245 photoresist is then spun at 4500 rpm for 60 sec and soft baked at 115°C for 90 sec. Two photoresists are approximate 2 and 3.5 μm thick, respectively.

Step (b) The wafer with photoresist is hard-contacted and patterned with the metal mask using “OAI Model 204IR Aligner”, and exposed and for 20 sec under ultraviolet (UV) light.

Step (c) After exposure, the wafer is developed for 2 min and 10 sec in a diluted solution of 1 part “AZ 400 K developer” to 3 parts deionized (DI)

water, followed by 2 min rinse in water twice and air gun drying. Due to the dark field mask and positive photoresist, the area without the photoresist is defined as the metal region. Figure 4.1_(c) illustrates the LOR and AZ9245 developing creates a bi-layer reentrant sidewall profiles due the undercut of LOR resist and the undercut from the top view looks like a shadow or double line along the edge of the pattern (4 μm undercut at one side in the figure). The undercut distance depends on the different parameters. Lower temperature/short softbake and longer developing increases the undercut, and vice versa. Note:

- 1) do not go below 160°C for LOR softbake,
- 2) baking time is not as strong an effect as baking temperature.

Step (d) Short and normal power oxygen plasma (30 sec, 150 w preferred) is always a subsequent step of lithography to clean the photoresist residual if any. The dry etch rate at 150 w power is about 0.4 $\mu\text{m}/\text{min}$.

Step (e) A thin film of 75 nm chromium followed by 225 nm of gold is sputter deposited in an environment of Argon gas at a pressure of 5 mT using “NSC3000 DC Sputter Tool” and deposition rates of Cr and Au are 0.3 nm/sec and 0.8 nm/sec. The reason of Cr/Au is that

- 1) gold has better electrical conductivity and consistent mechanical property than other metals,
- 2) chromium has great adhesion to the substrate than gold.

Figure 4.1_(e) indicates the discontinuity of Cr/Au at the steps which is the

major advantage of reentrant sidewall profile of LOR resist. Another advantage is the prevention of the formation of raised ridges at the edges of the patterns.

Step (f) The liftoff of Cr/Au is accomplished by immersing the wafer in Remover 1165 at 60°C and using a gentle abrasion with a cleanroom swab as needed. In the benefit of discontinuity, the liftoff can be performed without sonication when the minimum feature size is $15\ \mu\text{m}$. Then, the wafer is rinsed in isopropyl alcohol (IPA) for $5\ \text{min}$, DI water for $2\ \text{min}$ twice, and air gun dried. Without sonication, the metal came off in a large piece without tiny metal particles, which is capable of getting rid of the possibilities of metal particles dried on the wafer while it is transferred between two solutions.

It is noticed that the gold wires are slight larger ($1\text{-}2\ \mu\text{m}$) than design (dark field mask) because of photoresist undercut, which is not a matter for this process. This might have to be corrected in mask design for other applications.

So far the electrode pads and interconnection lines are formed, as shown in Figure 4.1_(f).

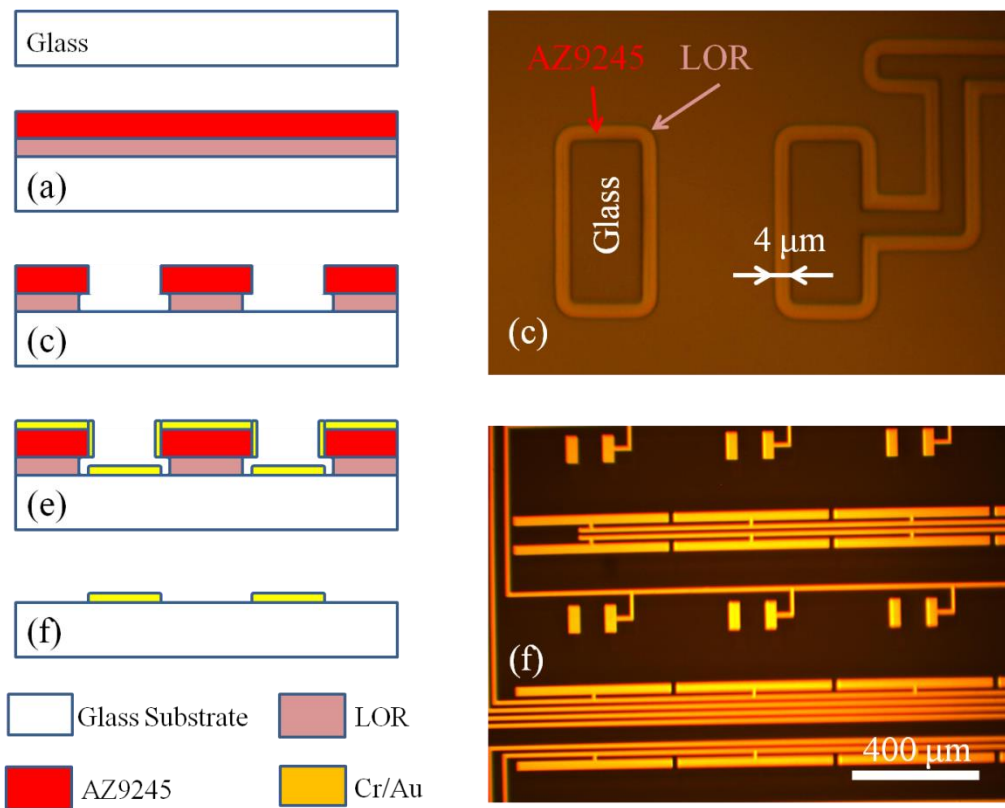


Figure 4.1. (Left) Fabrication process of metal layer: schematic in side view and (right) microscope images from top view.

4.2 Sacrificial Layer

Sacrificial layer is composed of two sub-layers. First sub-layer is a thin sputtered metal film as a seed layer and second one is the thick copper layer electroplated on the top of seed layer.

Step (a) The deposition and pattern of the Ti/Cu seed layer uses the identical liftoff process in the metal layer. First, LOR liftoff resist and AZ9245 were spun and soft baked separately, followed by exposure and developing. Figure 4.5_(a.1) shows the photoresist is remaining on the anchor areas only. Again, oxygen descum cleans the potential photoresist residual. And then, a film of 30 *nm* titanium and 300 *nm* copper is coated to cover the whole wafer (Figure 4.5_(a.2)) in the sputter tool and lifted off in Remover 1165 (Figure 4.5_(a.3)). The deposition rates of Ti and Cu are about 0.08 and 0.45 *nm/sec*. Titanium is served as an adhesion layer and the selection of titanium rather than other metal is relevant with the release which is the end step introduced later.

Since the LOR liftoff has been implemented in this process after the sacrificial layer mask design, 10 μm minimum feature size in light field mask of second layer is not ideal for the 2-3 μm single-side undercut. Care is taken in the developing time to avoid over undercut LOR. Figure 4.2 shows the over developing causes the small feature is undercut thoroughly and peeled off. The modification of this layer mask will be a work in the future. Alternatively, lithography of standard photresist can be used without the liftoff

resist. One option is to spin SPR220-3 at 3000 *rpm* for 30 *sec*, softbake at 115 °C for 90 *sec*, 8 *sec* exposure, followed by post-exposure-bake at 115 °C for 90 *sec* and 2 *min* 15 *sec* develop in “MF CD-26 developer”. Replacing Remover 1165 by acetone is suitable for a standard liftoff (no LOR).

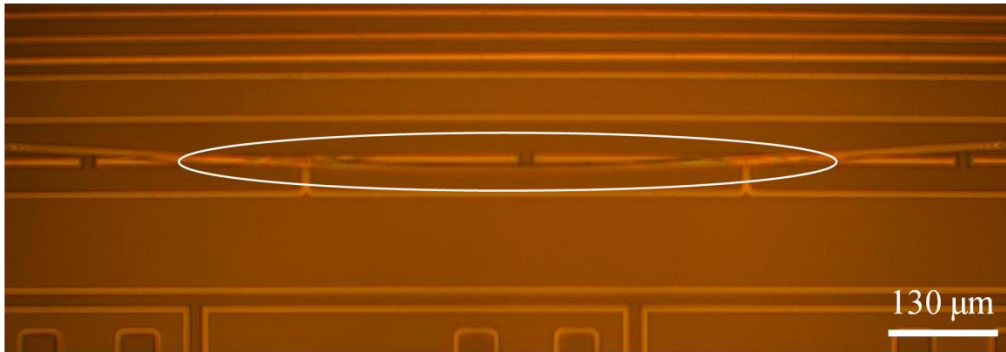


Figure 4.2. Over developing of liftoff resist caused AZ9245 peeled off.

Step (b) Another lithography with the same mask is used to define the anchor regions for copper electroplating. HMDS (Hexamethyldisilazane) is spun on in order to improve the adhesion of photoresist. Then, the spin of AZ9245 photoresist at 1000 *rpm* for 60 *sec* usually produces $8 \pm 0.5 \mu\text{m}$ thickness for a target of 5 μm copper plating. Thicker photoresist requires longer softbake and exposure, thus the wafer is soft baked at 115 °C for 2 *min* 30 *sec* and exposed 35 *sec* with hard contact. Agitation is suggested in a diluted AZ400K developer for thicker photoresis to achieve a more uniform developing speed across the wafer. However, it is still observed that the area of wafer close to the developer surface usually has been developed faster than the wafer in the bottom. With agitation, 5 to 6 *min* is sufficient to fully

develop everywhere. The misalignment between the sacrificial layer lithography and the seed layer shown in Figure 4.3 is attempted to be minimized.

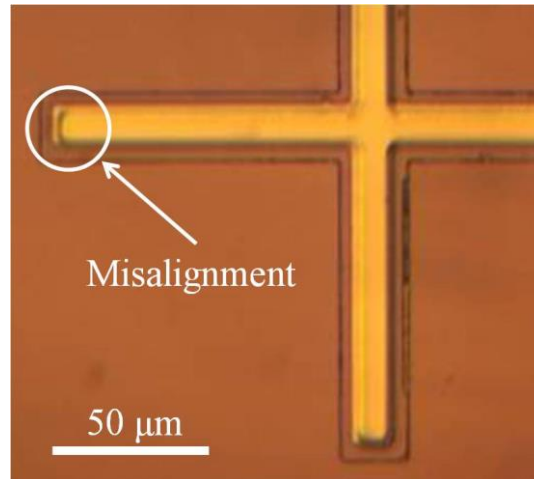


Figure 4.3. Misalignment due to twice sacrificial layer lithography.

Step (c) A $5 \pm 0.5 \mu\text{m}$ sacrificial layer of copper is electroplated on top of the Ti/Cu seed layer to cover the entire substrate except the anchor regions. Therefore, the plating area is about 78 cm^2 . Plating is done using a commercial copper sulfate plating solution “Technic Inc, Cranston, RI” in a 4 liter glass tank at room temperature. This solution contains 5-10 % copper sulfate, 15-20 % sulfuric acid as well as a small amount of chloride ions and brightener. A power supply is used to control the current through the wafer (connected to the negative terminal) and a piece of pure copper sheet (connected to the positive terminal). The size of copper sheet should be 1 to 1.5 times larger than the plated area on the wafer.

Compared with sputtering, the biggest advantage is that electroplating is

able to build much thicker metal layer easily and quickly, nevertheless, there are a few drawbacks of electroplating.

- 1) Less uniform deposition rate at different locations of plating solution or different plating shapes.
- 2) Rougher surface due to the particles.
- 3) Accuracy of plated thickness. There is no measure to the copper thickness simultaneously while plating (measurement is only available after plating).

Numerous care and improvement are taken to address the issues and presented as follows.

- 1) This “ready to use” solution has already balanced by the manufacturer (instead of mixing the copper sulfate anhydrous, sulfuric acid, and DI water).
- 2) A 3D printed plastic wafer holder (shown in Figure 4.4) is used to hold the wafer and a copper sheet in parallel to keep the same traveling distance of copper ions (Cu^{2+}). This holder is designed by a previous M.S. student in the group, Eric Schmitt.
- 3) A FloKing filter with a pump body is circulating the solution during the plating to absorb the copper particles and achieve a smooth film.
- 4) It is strongly suggested that the first run is to plate only half time of the expectation to finish (based on the previous experiment at the log book), measure the current thickness, compute the plating rate, then

plate the rest height using the current rate.

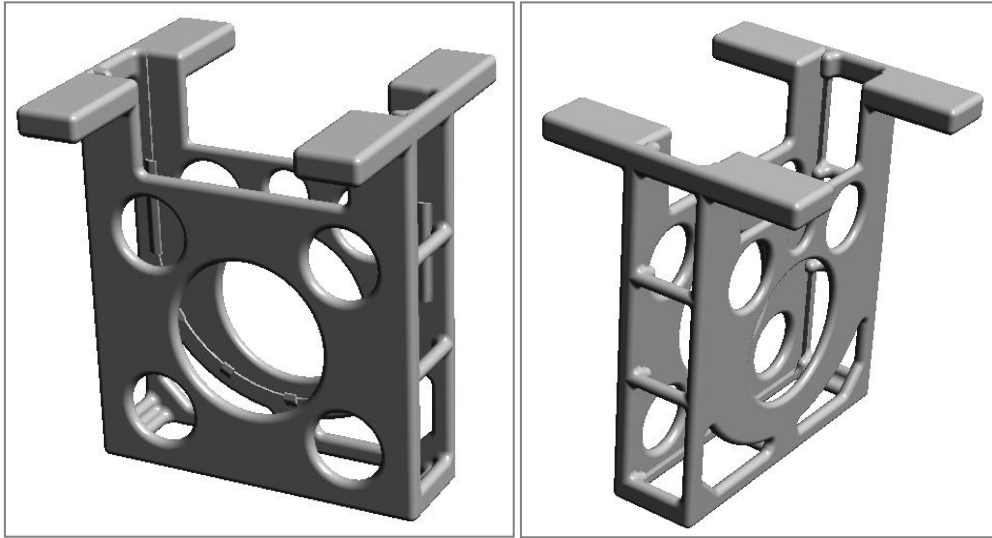


Figure 4.4. The holder for wafer and anode sheet in the plating solution.

These actions improve the plating quality indeed, but do not get rid of the troubles completely. These phenomena are observed, along with some discussions.

- 1) The plating rate is determined by the current density. A density of 5 mA/cm^2 results a rate of between 100 and 150 nm/min on this particular plating condition. $5 \pm 0.5 \text{ } \mu\text{m}$ takes about 40 min at a current of 0.4 A in this process.
- 2) The variation of plating rate can be caused by the age and the composition ratio of the plating solution, the different locations in the solution bath, the local plated area, the current drifting and the resolution of power supply, and the room temperature/humidity. For some reasons, the larger local area and location near the solution

surface have been plated slower than small area and the bottom of solution. Larger variation is observed as the current density goes higher, which is one reason we want to keep the density at 5 mA/cm^2 .

- 3) Another reason is that the current density is related to the copper roughness. Higher density, rougher surface. For 5 mA/cm^2 and a total $5 \mu\text{m}$ thickness of copper, the RMS surface roughness is between 50 nm and 150 nm . Surface comparison to 5 nm roughness of sputtered copper can be seen in the top view microscopes images of Figure 4.5_(a.3) and (d).
- 4) The deposition rate may not vary proportionally to the change of current density. For example, the rate went up to 340 nm/min at 10 mA/cm^2 occasionally.

Step (d) The AZ9245 photoresist is stripped in acetone 5 min and rinsed with isopropanol and DI water. Afterwards, a thin film of photoresist sticks on the wafer partially sometimes, which seems to be the photoresist residual. More investigation is needed to understand the reason causing this such residual. However, it is certain that they are able to be cleaned completely using oxygen plasma wet etch. A power of 200 w for 2 min is sufficient.

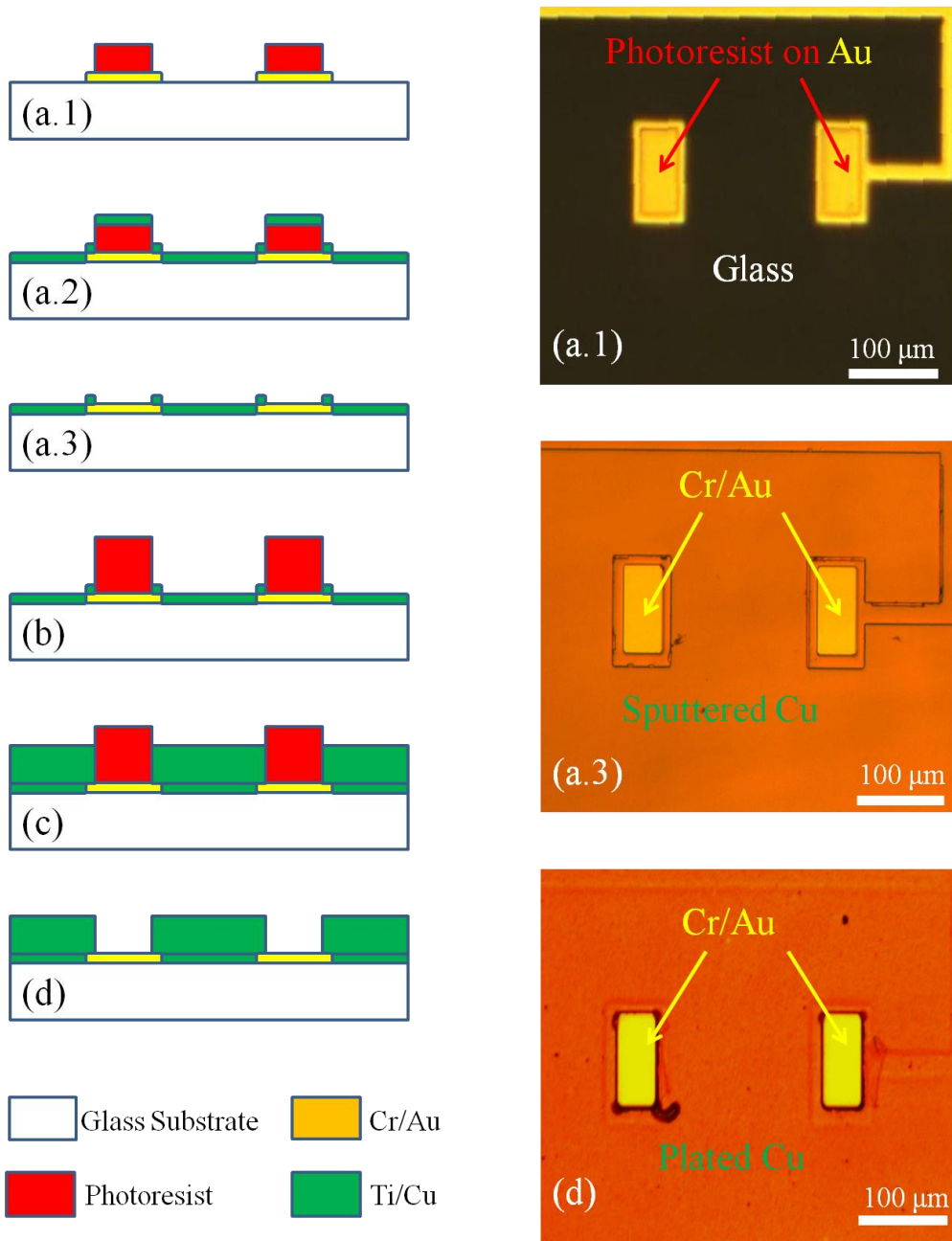


Figure 4.5. Fabrication process of sacrificial layer: schematic in sideview (left) and microscope images from top view (right).

4.3 Structure_1 Layer: Floating Element

First of two structure layers is the floating element and fabricated using AZ9260 photoresist as pattern and nickel electroplating. This lithography is more critical and difficult than others since the figure size is only 4 μm . Two major challenges here are the edge bead removal and optimization of exposure time.

Step (a) In order to create 10 μm photoresist mold for 8 μm floating element layer, this lithography process uses a high viscous photoresist, AZ9260. First of all, HDMS followed by AZ9260 were spun at 1500 *rpm* for 60 *sec*, soft baked at 115 $^{\circ}\text{C}$ for 2 *min* 30 *sec*.

In case of coating thick resist film, such as AZ series, there is a so-called edge bead that is the photoresist is accumulating pronouncedly near the substrate edge. Edge bead may cause sticking to the mask as well as undesired proximity-gap during exposure with a reduced lateral resolution as a consequence. And, low spin speed and high viscosity increase the edge bead. Although AZ9245 does have the same issue, the reason of why it has not been considered is that the minimum feature size is 10 μm and the aspect ratio is less than 1. When the feature size is down to 4 μm in this layer, edge bead removal (EBR) is vital for high aspect ratio of 2.5 (10 μm to 4 μm). The surface profile detected in the stylus profilometer, "VEECO DEKTAK 6M", displays the edge bead of AZ9260 at 1500 *rpm* spin speed is 13 μm higher of highest point than the wafer center and 3-4 *mm* wide, in Figure 4.6.

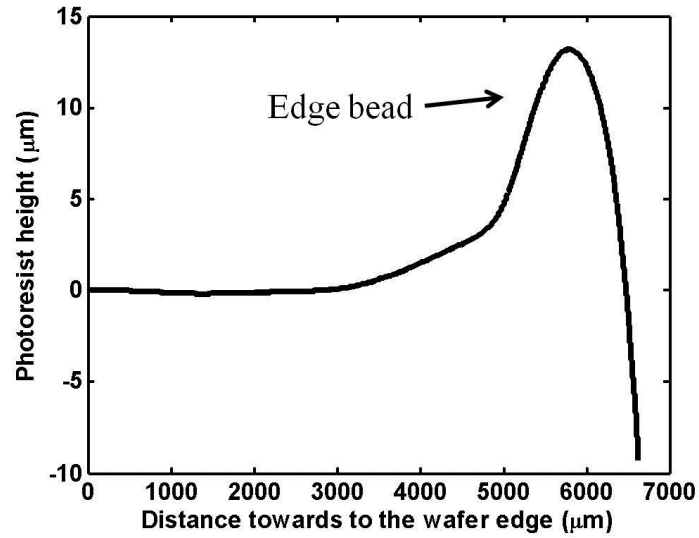


Figure 4.6. Edge bead of AZ9260 at a spin speed of 1500 rpm.

One method of edge bead removal is to manually swab (or dispense) acetone (or particular AZ EBR solvent) onto the edge of substrate which is spinning at a low speed (~ 200 rpm). It efficiently reduces the bead as low as $3 \mu\text{m}$. For best result, the other method is an additional step of exposure and developing with EBR shadow mask (shown in Figure 4.7) before normal mask is implemented to get a 5 mm -wide removal of resist on the outside of wafer.

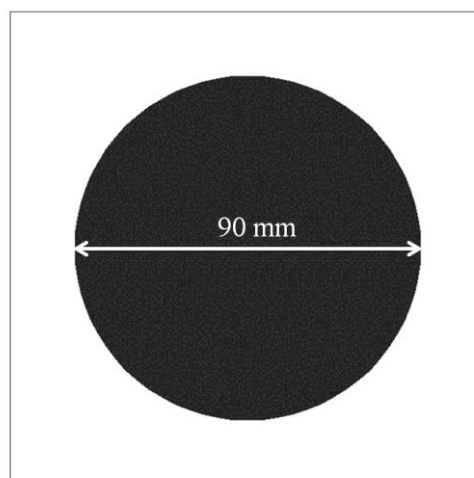


Figure 4.7. Layout design of edge bead removal (EBR) mask.

In the process, 80 *sec* over-exposure and 7 *min* developing are applied.

Result of both methods is shown below, in Figure 4.8.

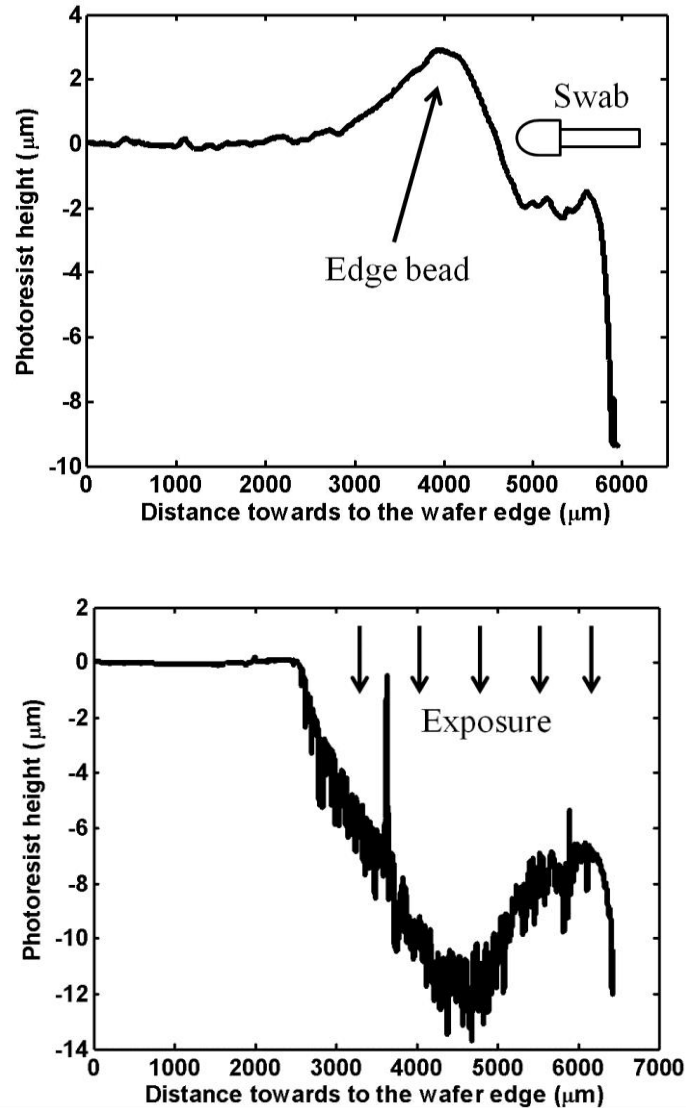


Figure 4.8. Surface profiles of wafer edge after the two different edge bead removals: (top) acetone swab and (bottom) EBR mask exposure/developing.

Then, next challenge is going to be the exposure time. Besides the small finger width and gap, AZ9260 is also sensitive to the roughness reflection, such as plated copper vs. sputtered copper. The rougher copper layer requires, first, a shorter exposure time to avoid over-exposure, but also a better

optimized exposure time because of the diffuse reflection of UV light. Figure 4.9 exhibits the photoresist patterns of the comb finger using different exposure time from 15 *sec* to 27 *sec*. The narrowest photoresist in (a.4) will not be able to survive in the electroplating solution of the next step, although it has higher potential sensitivity due to small gap. Therefore, the exposure time is optimized at 20 *sec* to achieve to 1 μm over-exposure of 4 μm finger gap so as to increase the sensitivity, reduce the developing time to 8 *min*, and adapt to plating. More than 2 *min* over-developing time should be averted because it can result the same appearance in Figure 4.9_(a.4).

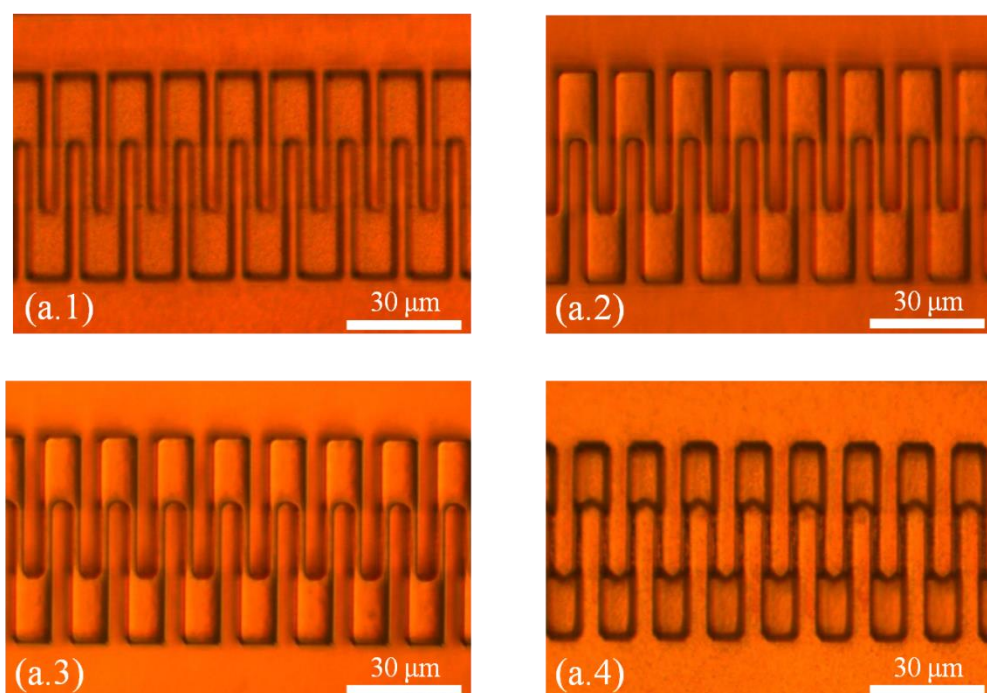


Figure 4.9. Photoresist of comb finger at the different exposure time and same developing time: exposure time goes from short to long from (a.1) to (a.4).

Step (b) As usual, oxygen plasma descum is performed here.

Step (c) Subsequently, a 8-9 μm height floating element layer is

electroplated using a commercial Nickel Sulfamate “Technic Inc, Cranston, RI” plating solution. This solution is comprised of 25-30 % nickel sulfamate, 0.5-1.5 % nickel bromide acid, and 1-3 % boric acid. The setup and process of nickel electroplating are very similar with copper, the differences are as follows.

- 1) A brief acid etch was conducted to remove any copper oxide because nickel is not going to plate on which the copper oxidizes. The reason of no action before copper plating is that copper oxides (no matter CuO or Cu₂O) are reacted with sulfuric acid and becomes into copper sulfate and water (or copper).
- 2) For nickel plating, 50 °C solution temperature is recommended by manufacturer. The first setup is to place the plating tank on the 25 cm × 25 cm hotplate, and put the small battery powered probe thermometer poking into the solution. Next step is to set the hotplate to 200 °C and heat it up rapidly. Once it reaches to 50 °C (it usually takes 1.5 hr), next is to reduce hotplate to 160 °C. The solution temperature should stabilize at 50 °C. It might have to adjust to the hotplate by small amount if necessary to achieve 50 °C solution temperature.

Hence, nickel is plated at 50 °C at a current density 5 mA/cm² which results a current of 0.2 A (the plating area including EBR is 40 cm²) and a deposition rate of approximately 100 nm/min. The surface roughness of the

nickel after plating is 150 *nm* to 200 *nm*. The roughness appears to be a reflection primarily of the roughness of the copper sacrificial layer. Actually, nickel plating performs a smoother surface and fewer particles than copper. The nickel roughness should be less than 50 *nm* on the sputtered copper.

Step (d) It is identical as step (d) in the sacrificial layer: photoresist stripping in acetone and residual cleaning using RIE.

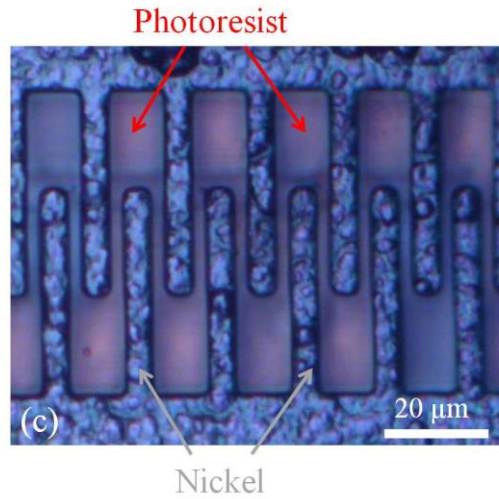
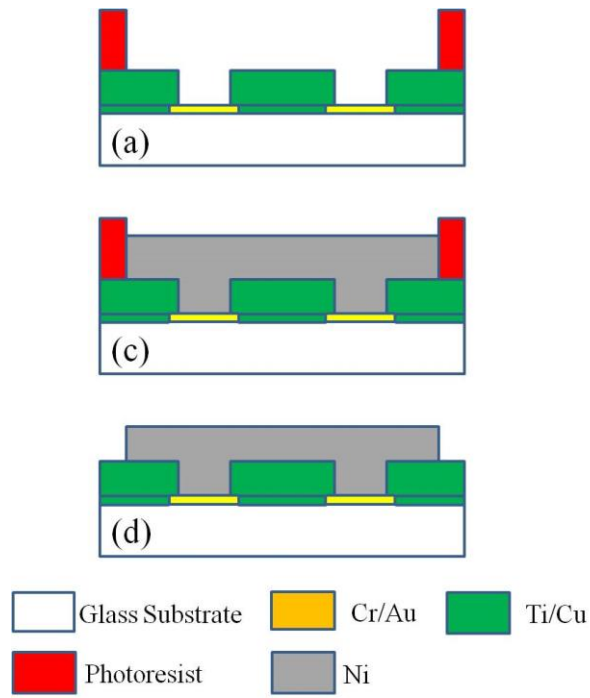


Figure 4.10. (Top) Fabrication process of floating element layer: schematic in side view and (bottom) microscope images from top view.

4.4 Structure_2 Layer: Bump

This bump layer is produced identically as the floating element layer with slightly different parameters at each step.

Step (a) While an even thicker ($16\ \mu\text{m}$) photoresist is performed using $800\ \text{rpm}$ spin speed, this lithography is less strict on exposure and developing time since the aspect ratio is only 0.8 ($20\ \mu\text{m}$ diameter bump). Experimental result has shown a relative low temperature of softbake is better for thicker photoresist to have uniform thermal conduction, so 100°C and $3\ \text{min}$ are applied. Then, $90\ \text{sec}$ edge bead removal exposure and $6\ \text{min}$ develop followed by $45\ \text{sec}$ bump layer exposure and $8\text{-}10\ \text{min}$ develop in AZ400K are operated. At the bump mark exposure, a UV filter is used to provide a cut-on wavelength of $360\ \text{nm}$, blocking the shorter wavelengths and transmitting the longer wavelengths, and improve straight feature walls of photoresist. Note: as the lithography on the fourth layer, it is getting harder for the photoresist to overcome the surface topology, especially $8\ \mu\text{m}$ thick floating element structure. Figure 4.11 shows the uneven photoresist spinning on the edge of wafer only. However, there is no defect on the bump location at all and they do not hunch up. Thus, it does not influence the following steps.

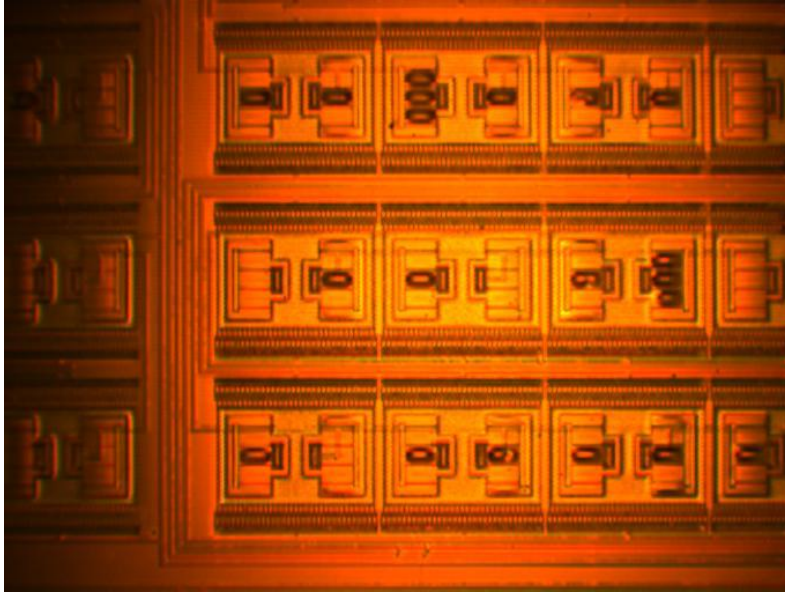


Figure 4.11. The photoresist did not spread out uniformly on $8\mu\text{m}$ floating element structure of the wafer edge.

Step (b) When the area of bump layer is only 0.72 cm^2 , it barely plates at a tiny current 4 mA if keeping a current density of 5 mA/cm^2 . As it mentioned, the deposition rate does not exactly follow the current density linearly, 0.06 A is used and reaches 200 nm/min . Photoresist removal is not needed after plating in this layer.

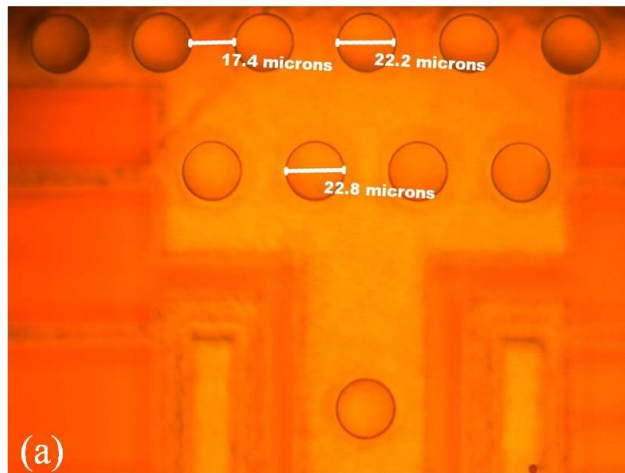
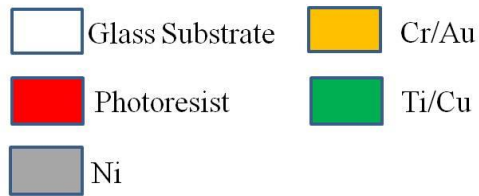
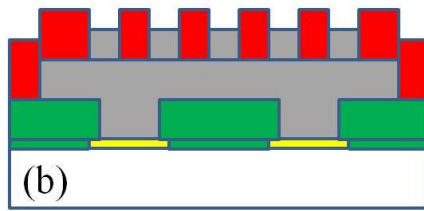
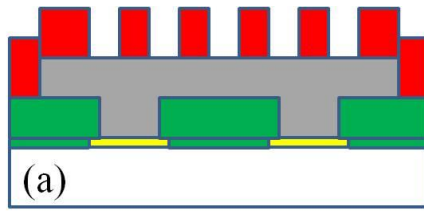


Figure 4.12. (Top) Fabrication process of bump layer: schematic from side view and (bottom) microscope images from top view.

4.5 Dice and Release

This section will introduce, first, dicing the wafer into a large amount of individual square chips, second, chip release of removing the sacrificial layer to create the air gap under the floating element.

Step (a) A layer of photoresist (AZ9245) is spun on the wafer to protect the structures from dicing. That is why the previous photoresist does not have to be removed.

Step (b) The MA1006 die saw is used for dicing the wafer into 10.1 mm^2 . Programming of the wafer diameter, index distance, cut depth and blade speed is able to automatically start dicing along the cutting lines.

Step (c) The individual chips are then immersed in acetone to strip the photoresist, and rinse with isopropanol, water.

Step (d) The copper sacrificial layer is etched away in a mixture of 1 part acetic acid to 1 part 30% hydrogen peroxide to 18 parts DI water for 24 *hr*. It etches all 5 μm copper within 0.5 *hr*, but attacks the titanium much slowly. High selective to Ti/Cu only allows the long time release. The chip is, then, rinsed in water twice, isopropanol, and methanol (low surface tension and less chance to stick down), and allowed to air dry in a dry box that has been flooded with clean dry air with a low relative humidity. Figure 4.13 provides an overview of a group of released floating element with surface bumps and gold route underneath.

An interesting phenomenon has been noticed in the original process.

After etching the sacrificial layer, there are appeared two obviously different colors of metal layer depending on the sacrificial mask design. The locations of Cr/Au layer without Ti/Cu sputtering are the pure gold color, however, the gold surface which used to coat with Ti/Cu presents to be a red color after Ti/Cu is stripped. Figure 4.14 explains it explicitly and has two cases at the same time. It is also known that once the gold surface turns into red color, it is not able to be cleaned in either wet or dry etch. Energy-dispersive X-ray spectrum on the red surface indicates a minor peak on titanium besides a major gold peak, which means something changed in the interface of gold and titanium in the nickel plating (not in the copper plating). This sort of titanium contamination does not have an obvious effect on the electrical conductivity but bring trouble in wirebonding from the electrical pads to the package (the packaging process will be discussed in chapter 5). The pure gold surface is most ideal and easiest to wirebond via gold wire. In order to solve it, all electrodes have been designed as anchor regions and added on the sacrificial mask (see Appendix A.2), so, they are covered by photoresist to prevent the copper plating.

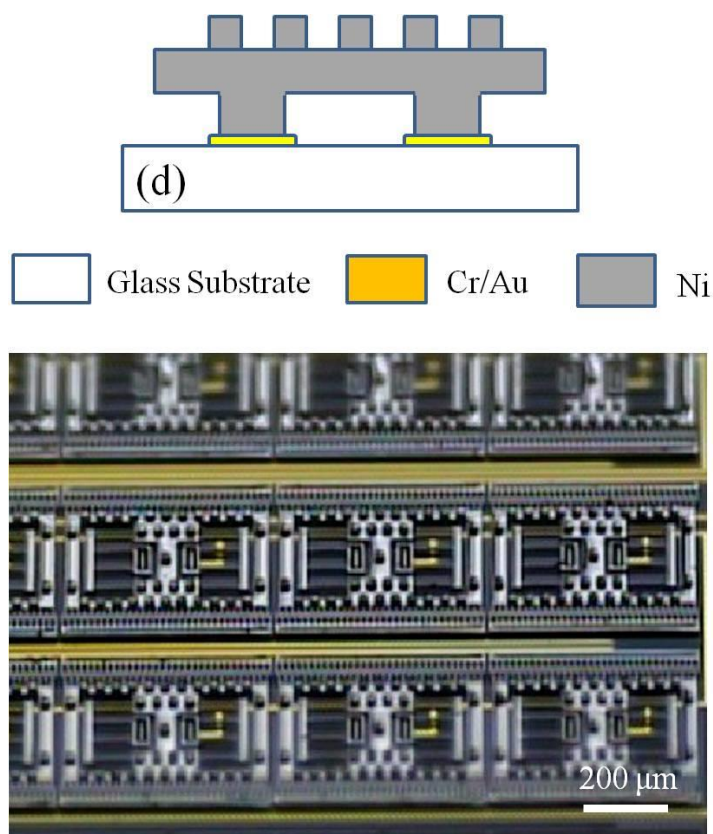


Figure 4.13. After releasing, (top) schematic in sideview and (bottom) overview of a group of floating element with bump.

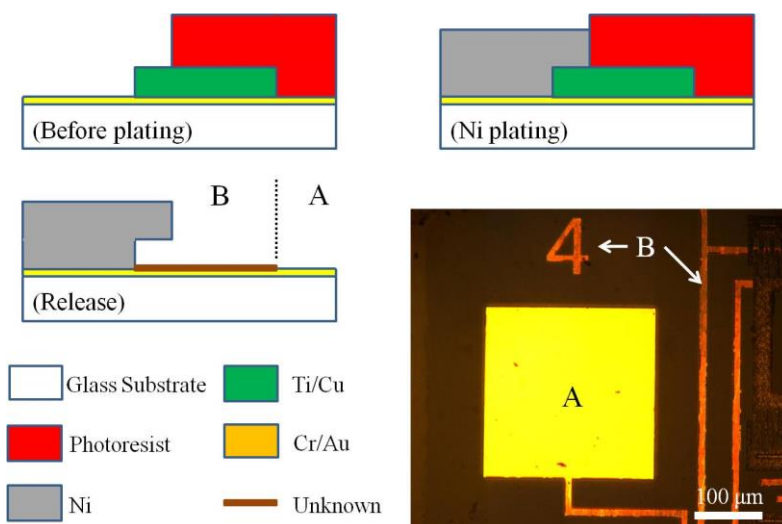


Figure 4.14. Explanation of interface reaction between Ti and Au caused by the nickel plating process.

4.6 Dimple Layer (optional)

Besides the essential four-mask microfabrication procedure discussed above, a “Dimple” mask is alternative that can be added followed by the sacrificial layer. This layer is on purpose of reducing the bottom area of floating element that is in contact with the substrate as well as the stiction issue during the release step. However, no dimple layer is on the floating element sensor in this dissertation. Figure 4.15 demonstrates the process.

Step (a) After 5 μm copper is plated, a layer of photoresist is coated and patterned on top of the copper sacrificial layer. The identical non-LOR lithography steps and parameters used in seed layer are used here.

Step (b) A short copper wet etch in “Transene Copper Etchant Type APS-100 (contains 15-20% Ammonium Persulfate and Water)” is applied for 10 *sec* to create the dimple array pattern, which will be reflected under the floating element after release.

Step (c) Then, photoresist is removed in acetone and the process is going to continue with the floating element structure and so on.

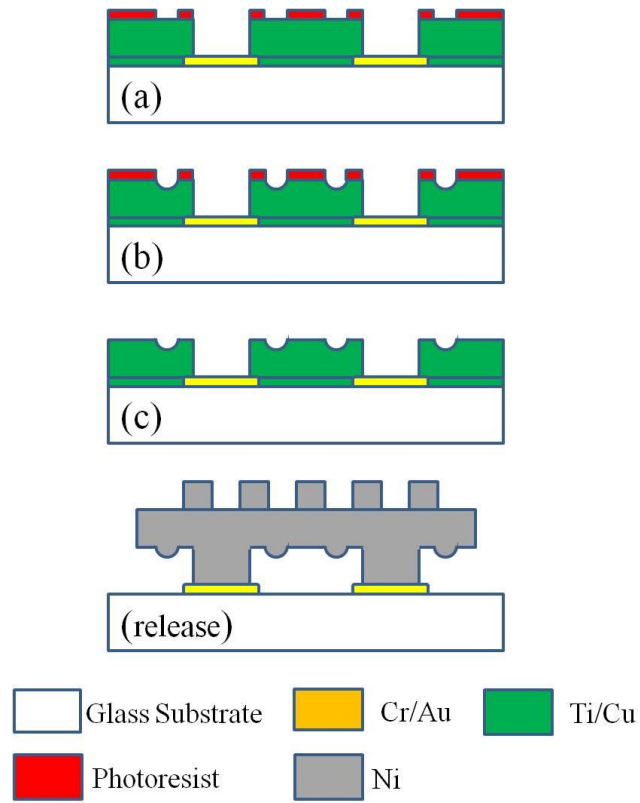


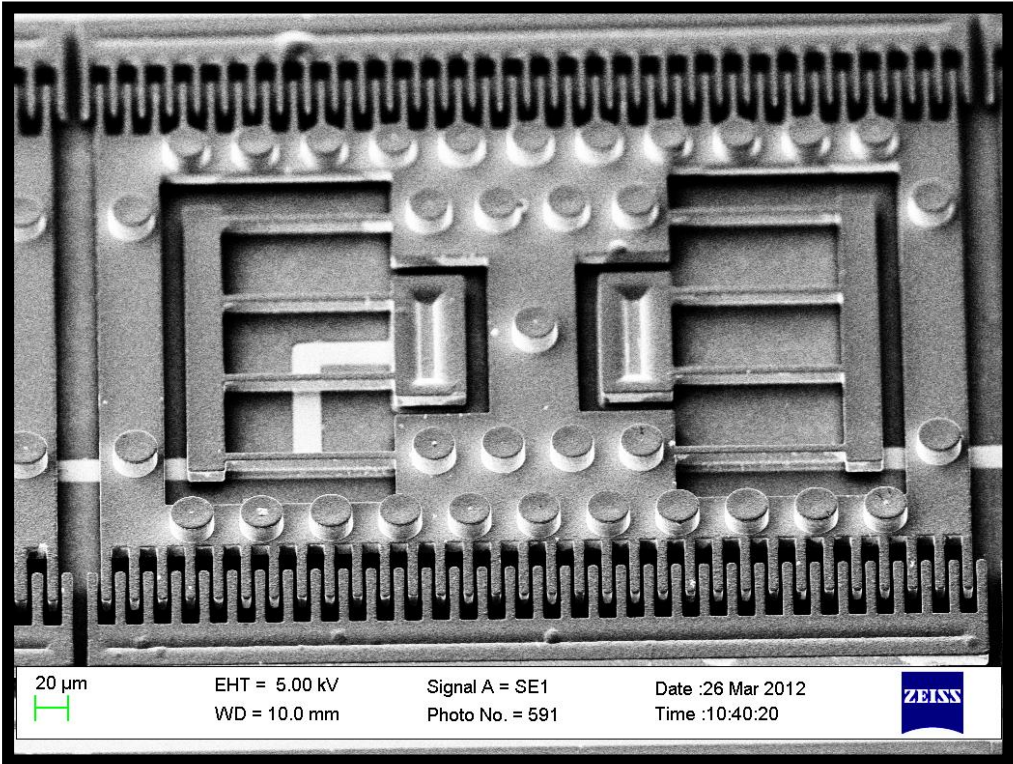
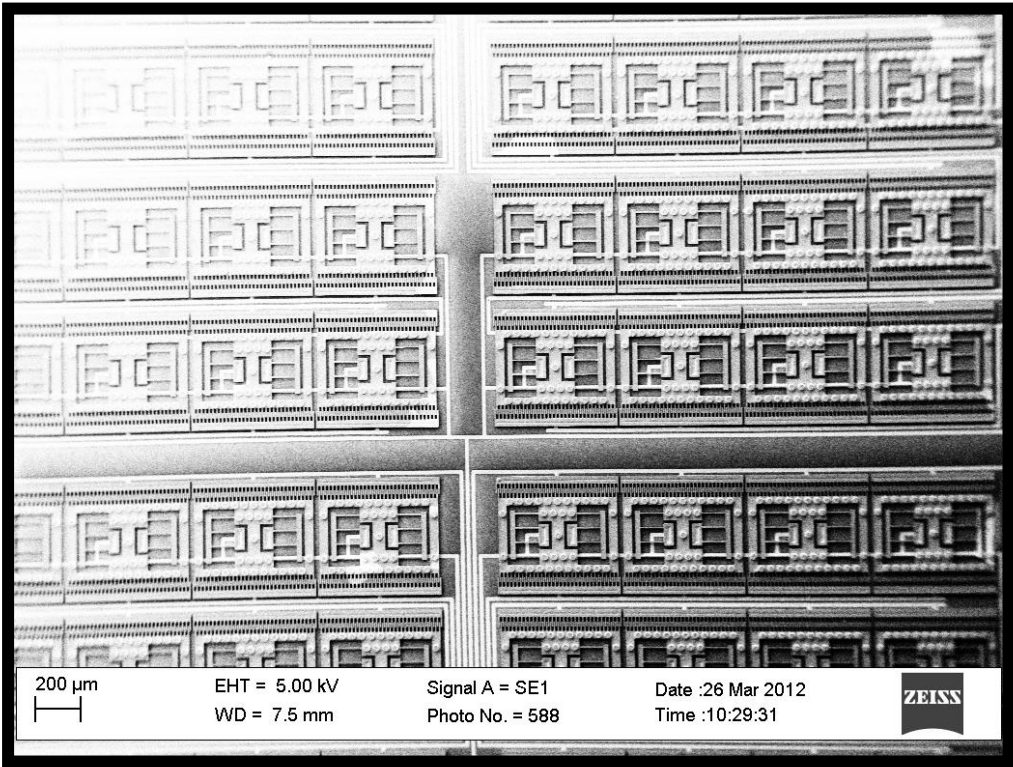
Figure 4.15. Schematic of fabrication process of dimple layer.

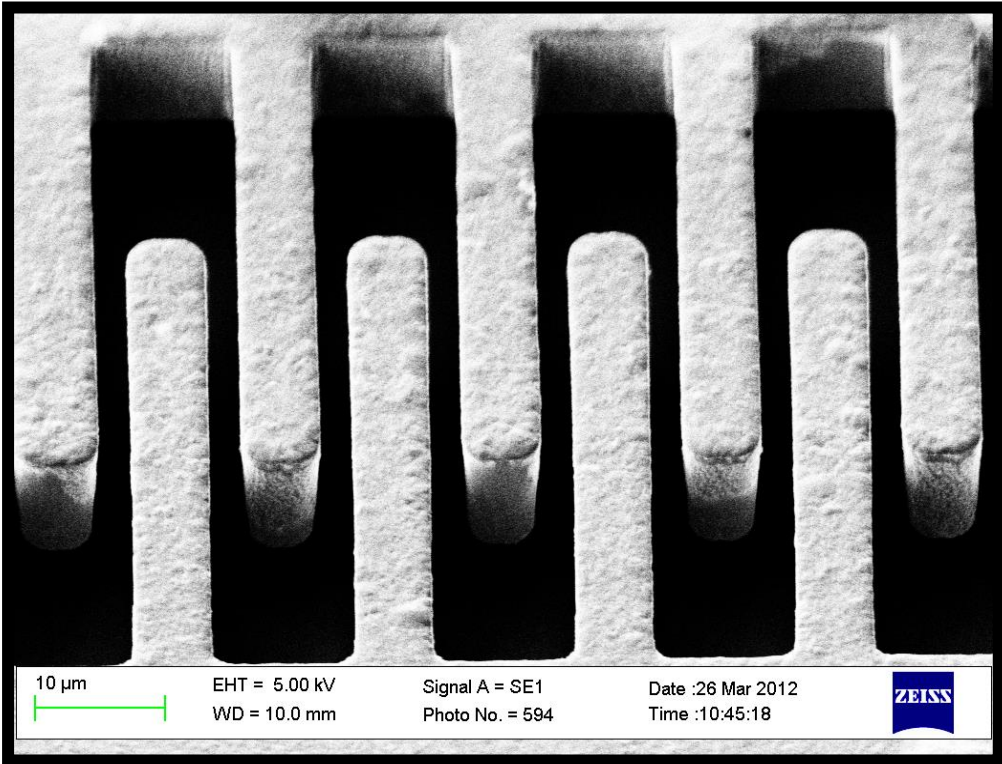
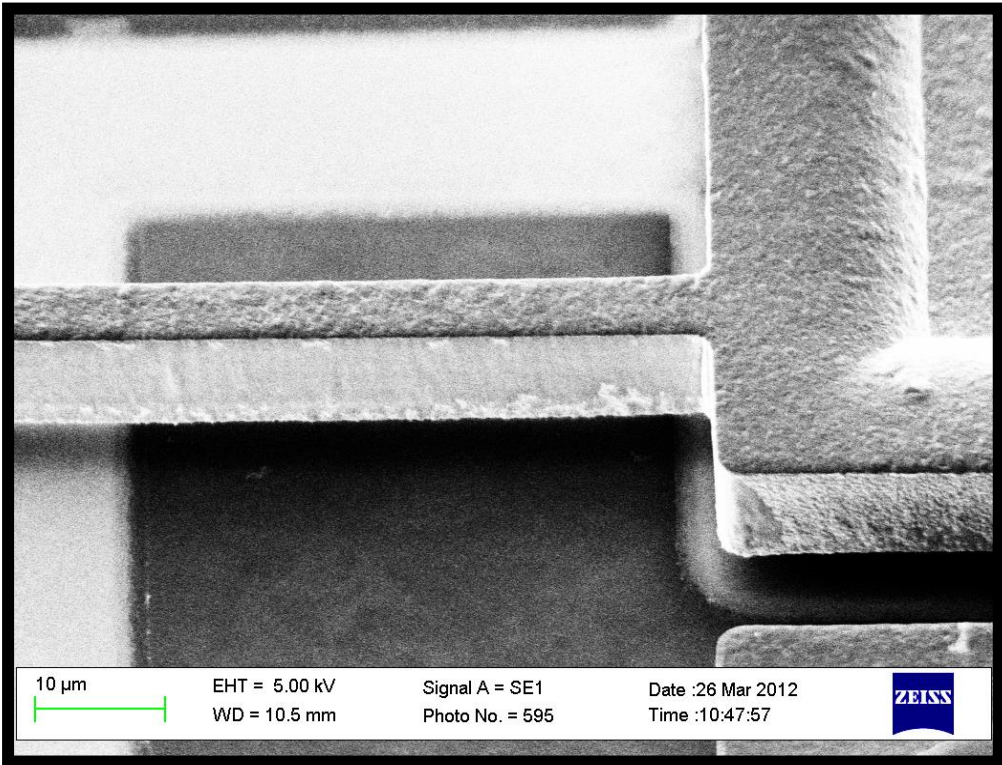
4.7 SEM Images

Images in Figure 4.16 are taken in “Zeiss EVO MA series Scanning Electron Microscope (SEM)” and showing the released structure. The manufactured dimensions shown in Table 3.2 were taken from the SEM images for in-plane dimensions and from white light interferometry measurements for layer thicknesses.

Table 4.1. Design and as-manufactured dimensions of the floating element with bump sensor.

Symbol	Property	Design	Manufactured	Units
d	Finger gap	4	2.9	μm
	Finger width	4	5.1	μm
t	Thickness of structure	8	8.8	μm
w	Width of folded beam	4	5.1	μm
L	Length of folded beam	100	99.2	μm
H	Height of bump	12	11.7	μm
D	Diameter of bump	20	24.7	μm
g	Height of air gap below shuttle	5	5.2	μm





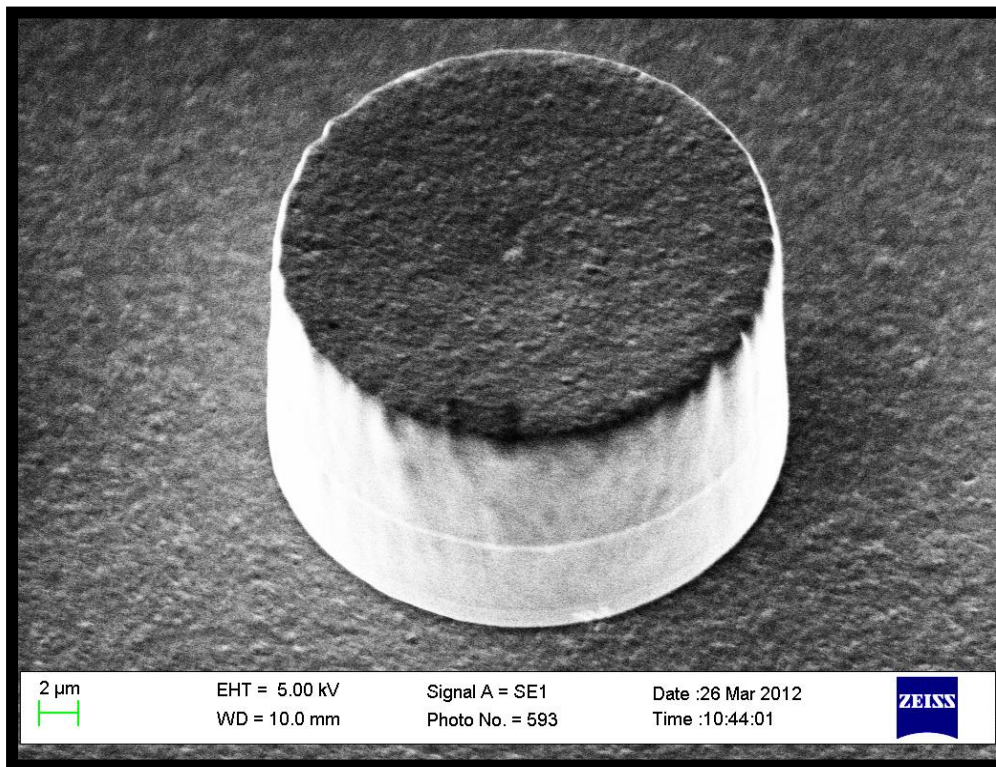


Figure 4.16. SEM images of a released sensor chip: multiple elements in one group, a single element, a beam attached to anchor with an air gap underneath, comb fingers, and a bump (from first to end).

Chapter 5

Packaging

Packaging is required to serve as the interface between micro-scale MEMS devices, electronics, and the environment. This is a vital component in MEMS design. Two packaging approaches for the microfabricated $10.1\text{ mm} \times 10.1\text{ mm}$ MEMS floating element chip are presented in this chapter. The first method uses a standard ceramic pin grid array hybrid package (CPGA), wirebonding as the electrical connections, and epoxy encapsulant. This was the first generation package that we used. A second method uses printed circuit board (PCB) packaging, focused on a lower surface topology and probe configuration, and uses conductive ink for the connections and an aluminum tube for cylindrical housing. Three corresponding electronics design are also presented in the second section.

5.1 Packaging

Since the MEMS floating element sensor is designed for application in both a laminar duct flow and a turbulent boundary layer in a wind tunnel, the height of the sensor in the package is critical to the sensor performance. If the sensor surface is flush with the package surface, the package will not disturb the flow and influence the flow characteristics. This section will include two packaging processes of the released MEMS chip and how the chip is flush packaged.

5.1.1 CPGA Packaging Process

The process starts with a 4 *cm* × 4 *cm* ceramic pin grid array (CPGA) hybrid package [Spectrum Semiconductor Materials, San Jose, CA], with 144 pins, of which 48 are used. The CPGA is arranged in a 15 × 15 array and a schematic drawing of the design is shown in Figure 5.1. The process contains the following main steps: CNC machining of CPGA cavity, wirebonding, and epoxy encapsulant. The critical step is that epoxy is used to, first, modify the height of package cavity according to the thickness of the MEMS chip, and second, cover any topology between the package and chip in the end. The details are introduced as follows.

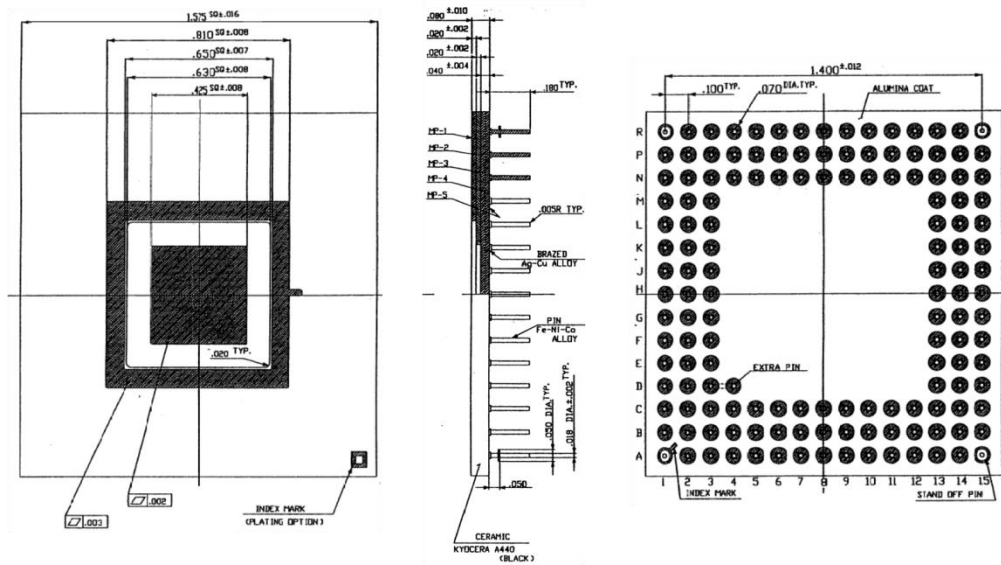


Figure 5.1. Schematics of CPGA used in MEMS floating element shear stress sensor (measurements are in inches). [Spectrum Semiconductor Materials, San Jose, CA]

Step (a) The CPGA cavity is partially filled with potting epoxy “Namics Chipcoat G8345-6” [NAMICS Corporation, Niigata City, Niigata Prefecture, Japan]. The reasons of choosing this epoxy are

- 1) a low viscosity of 50 Pa s is better for step coverage and achieving a flat surface;
- 2) a low coefficient of thermal expansion of $15 \text{ ppm}/^\circ\text{C}$ is appropriate to the various temperature conditions;
- 3) a high resistivity of $3 \times 10^{13} \text{ } \Omega \text{ cm}$ is suitable to encapsulation and electronics;
- 4) high temperature ($>100^\circ\text{C}$) curing temperature allows efficient working time.

Because of high fluidity, care is taken to not overfill so that the epoxy does not flow over the gold finger bonds on the CPGA. The epoxy is then

cured on a hotplate at 90°C for 1 *hr* and then increased to 160°C for another 1 *hr* to ensure low stress during curing and minimize the warpage of the epoxy.

Step (b) After curing, the epoxy is CNC (computer numerically controlled) milled to the appropriate height, including a small square pocket to center and align the chip. Therefore, it allows the MEMS chip to be flush mounted to the top of the package and centered in the package by calculating the chip's height and milling from the top of the package down to that height plus an additional $25\ \mu\text{m}$ to account for the epoxy that will secure the MEMS chip in the step (c).

Step (c) The chip is mounted into that pocket with depositing a small amount of the same epoxy. A fast curing step is done here, heating to 130°C for 5 *min* and then increasing to 160°C for another 10 *min*.

Step (d) The wirebonding machine (Marpet Mech-EI MEI 1204B Gold-Wire Ball Bonder) is used to ball bonded on the electrode pads and wedge bonded to the finger bonds on the CPGA via $25\ \mu\text{m}$ diameter gold wires. Careful attention is taken to minimize the height of gold wire so as to reduce the surface topology. The layout of the pads, fingers on the top side and pins on the back side of package are configured as illustrated in Appendix D.

Step (e) Finally, the wire bonds are potted in epoxy, which is allowed to settle and cure, with multiple layers being applied until a flat surface is achieved around the chip and package. The epoxy is cured identically as in

the step (a).

Using this method, it is possible to create a flat surface with a total maximum topology from the ceramic surface, onto the epoxy, over the wire bonds and onto the chip of approximately 0.1 mm. Figure 5.2 shows a photograph of the packaged chip, and a stylus profilometer scan of the surface topology from the package, onto the epoxy, across the wirebonds, onto the chip and back onto the package. As can be seen, the packaging exhibits approximately 0.1 mm of total topology, and the chip is parallel to the package surface within 0.1°.

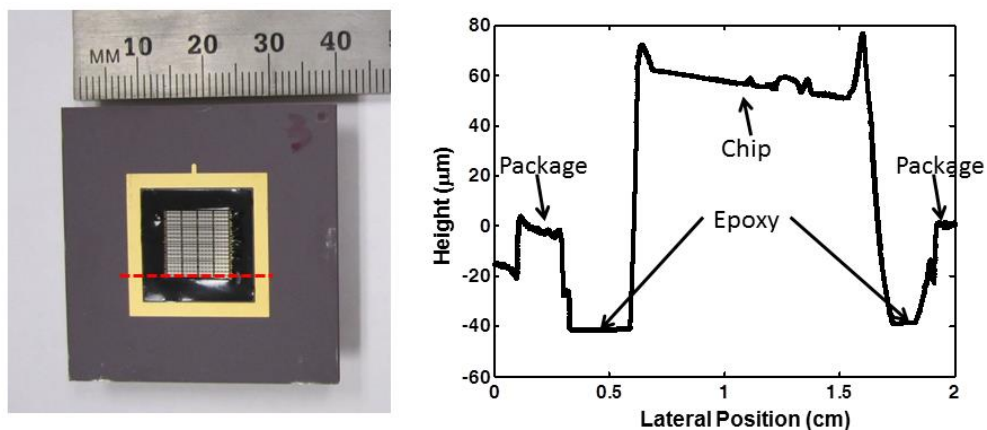


Figure 5.2. (Left) A finished sensor chip packaged and potted in a ceramic pin grid array package. A dashed line indicates the line along which a stylus profilometer scan was taken. (Right) The measured height of the surface topology along the indicated scan line.

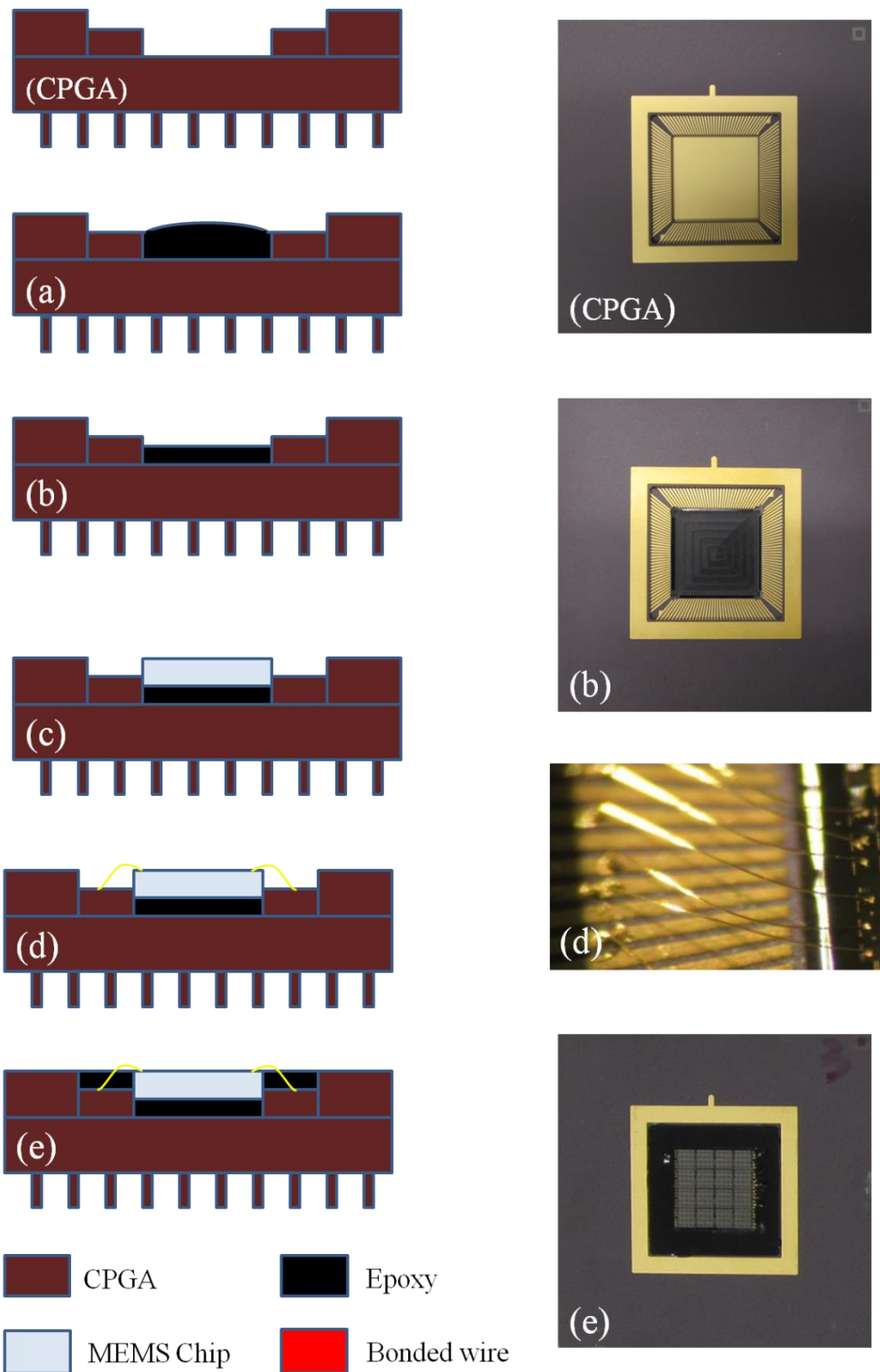


Figure 5.3. Schematics and photos of the CPGA packaging process

5.1.2 PCB Packaging Process

A second packaging method was investigated. The reason and goal to develop another packaging technology are to 1) replace the square configuration by the circle configuration for an access to package rotation in a flow channel, 2) high repeatability to achieve a low surface topology and better flush mounting, 3) reduce the package size as well as electronics (in the next section) to extend the application conditions. This process is originally designed and developed by a previous M.S. student in the group, John Burns, then modified and improved by the author.

The process starts from a 24 *mm* diameter circular printed circuit board (PCB) with 11 *mm* × 11 *mm* center cutout in which the MEMS chip is filled.

Step (a) An acrylic stencil is designed with a cutout slight smaller than MEMS die size. The stencil is cut from a cast acrylic using a benchtop laser cutter. After manufacturing, the cutout is about 200-300 μm smaller than the die. Care is taken to align the stencil to PCB to create the proper margin on all sides. A piece of adhesive film is placed between the stencil and the PCB, and the center tape is cut away along the stencil using a scalpel, as shown in Figure 5.8_(a.2). This step allows subsequent positioning of the MEMS chip face down, flush with the PCB surface, without damaging the nickel floating element structure. It is not a concern if the tape touches the gold pads on the left and right edges of the die. The tape can be chosen to be either “ProFilm DX266C Dicing Tape” [Avantek, Calamba, Laguna,

Philippines] or “Rev-alpha thermal release tape” [Nitto Denko America, Fremont, CA], both of which have been used successfully. Dicing tape is adhesive on one side only with high adhesion, and rev-alpha tape is double side, but less adhesive. Neither of them is perfect for this application. The ideal tape should be double sided, with good adhesion, and sufficient hard base material. Such a tape has not yet been identified.

Step (b) It is now safe to place the MEMS chip face down into PCB cutout and stick it on the tape. It is better to flip it over, check the position of MEMS chip on a microscope to make sure the tap is not on the nickel. Redo or gently move the chip if needed. Then, the uniform pressure is applied on the back side of chip to avoid any missed contact area, or if the chip is tilted to the PCB.

Step (c) Next step is to fill the back cavity with epoxy to permanently secure the die on the PCB. The epoxy used here is selected to be relative high viscosity, such as “Loctite Fixmaster Poxypak Epoxy” or “Loctite E-00NS Hysol Epoxy” [Henkel Corporation, Westlake, OH], to minimize the area in which the epoxy seeps in to covers the pads or create the topology. The photo (a) of Figure 5.4 is showing the overflowing of relative low viscous epoxy, “Loctite E-60NC Hysol Epoxy”. The photo (b) is the best result, the Poxypak epoxy stops flowing until barely reaching the top of MEMS die. However, over viscous epoxy, E-00NS, is not fully filling the gap around the die, as shown at Figure 5.4_(c). Note: these results are tested on the

application of an Advantek dicing tape. The proper viscosity is dependent on how adhesive the tape is; for instance, Poxy Pak epoxy is too fluid for the rev-alpha tape.

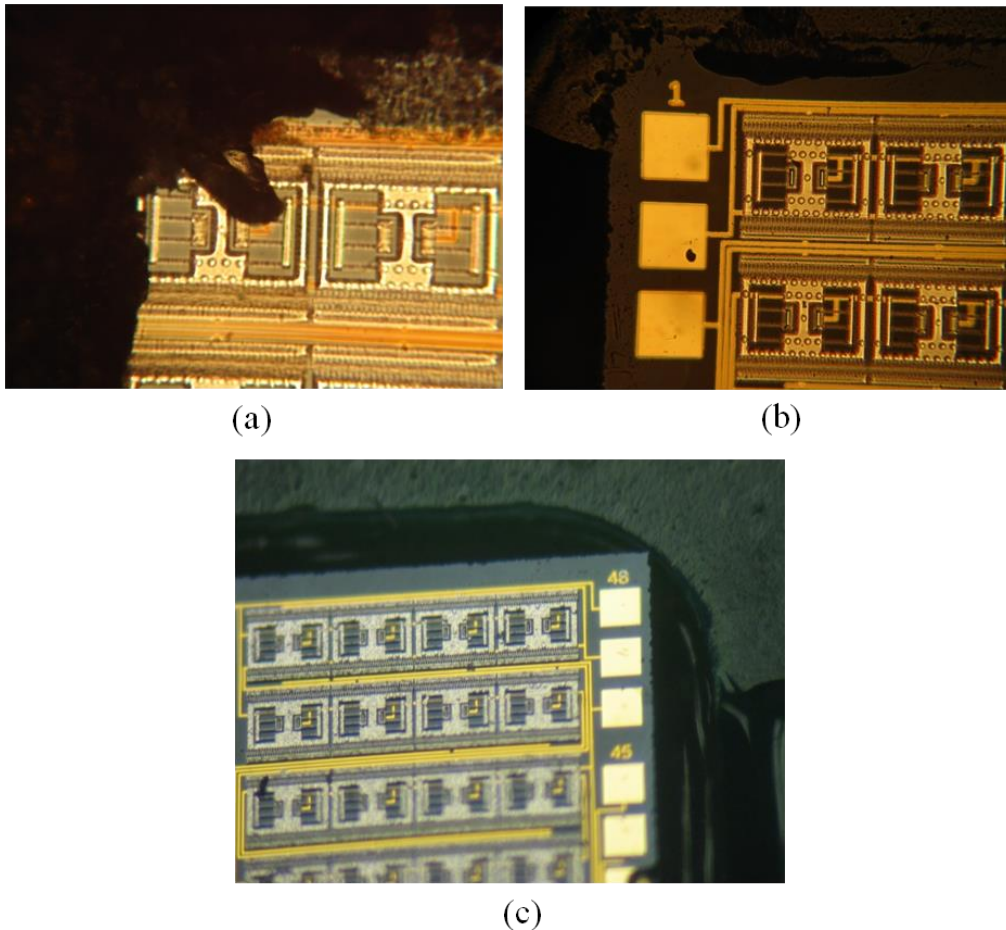


Figure 5.4. The situations of using different viscous epoxy as adhesion to the MEMS chip: (a) over fill, (b) full fill, (c) under fill.

Depending on the different epoxy, the curing time is varied from 30 *min* (E-00NS epoxy) to 10 *hr* (E-60NC epoxy). A low viscosity has a long working time and requires a long curing time. Once it is cured, the stencil and tape are peeled off gently and slowly, and are not allowed to touch the sensor structure.

Step (d) This optional step is intended to solve the issue shown in Figure 5.4_(c), where there is insufficient fill. It can be skipped if not necessary.

In a situation of under filling the epoxy, a low viscosity epoxy, E-60NC, can be used to directly inject into the open groove between the PCB and the chip. A syringe with a small tip (~ 2.5 mm outer diameter) should be used, followed by a 10 hr curing at the room temperature. Heating might be a possibility to reduce the curing time, but has not been tested.

It is important to have a smooth surface from the PCB to the chip, because the conductive ink does not have good step coverage.

Step (e) Now, the chip is flush mounted with the PCB, and 125-13 electrically conductive silver ink [Creativematerials, Ayer, MA] is ready to serve to electrically connect from the pads on the MEMS chip to the corresponding pins on the PCB. The drawing system setup is shown in Figure 5.5.

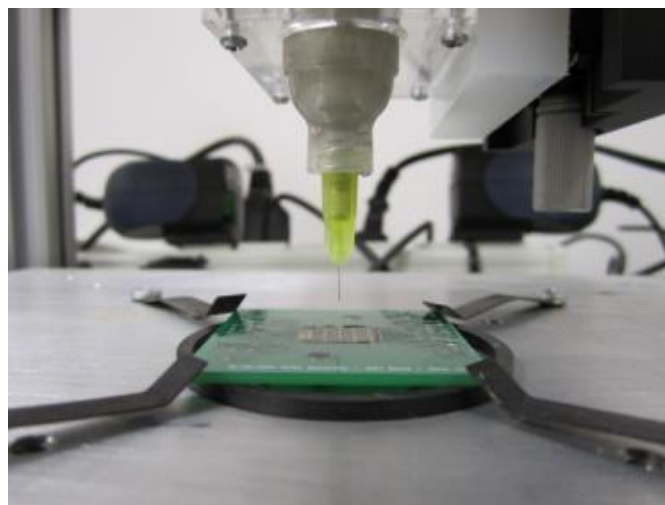


Figure 5.5. A photo of conductive ink drawing setup [43].

It consists of an aluminum flat plate on the bottom, controlled by a pair of digital micro stages underneath in the in-plane directions, the ink syringe holder attached to a manual micro stage is perpendicular to the plate, a microscope is used to help locate the pads, and a dispensing system with a pressure switch is used between a mechanical pump and the ink syringe [43].

The automation of on/off of the dispensing system, micro stage motion, and alignment, was attempted using a LabVIEW program, however, they are not fully functional without further hardware improvements. Therefore, the following manual steps were used to draw the conductive ink traces.

- 1) Load the PCB with a MEMS chip on the Al plate and secure the PCB with four springs, turn on the mechanical pump and set the pressure at 2-4 psi.
- 2) Manually lower the ink syringe with a thinwall precision machine tip [Integrated Dispensing Solution, Agoura Hills, CA] to close to the PCB, so that microscope can focus on both the tip and PCB surface. The pads on the MEMS chip are supposed to be horizontal to the pins on the PCB. Due to the alignment error, it is likely the chip is shifted slightly in the cutout. In this case, the whole package has to be rotated and adjusted according to move the syringe tip back and forth over the air, until a pin and a corresponding pad are on a straight line, which means all of them are corrected. Note: the ink has to be thawed out at room temperature more than 2 *hr* for best result prior to

using.

- 3) Lower the syringe to barely touch a pad. Then, turn on the dispensing system (you should be able to see the ink is flowing right now), immediately move the base stage (do not let the ink spread out too much and touch the neighbor pads). Once the ink is connecting to the pin and first drawing is finished, stop the moving and dispensing, raise up the syringe.
- 4) The syringe is moved to the next pad, and the step 3 is repeated, and so forth. When all connections are finished, the package is transferred on a hotplate and the ink is cured at 150°C for 5 min . Although the recommendation temperature is 180°C on the datasheet, it is observed that the higher temperature has resulted in cracks on the E-60NC epoxy.

The detailed ink lines and the overview of one chip are shown in Figure 5.6 and Figure 5.7. The height of single ink trace is approximate $30\ \mu\text{m}$, and the width is in the range between $150\ \mu\text{m}$ and $300\ \mu\text{m}$, depending on the usage of tip, the position of tip above the package surface, and the surface topology.

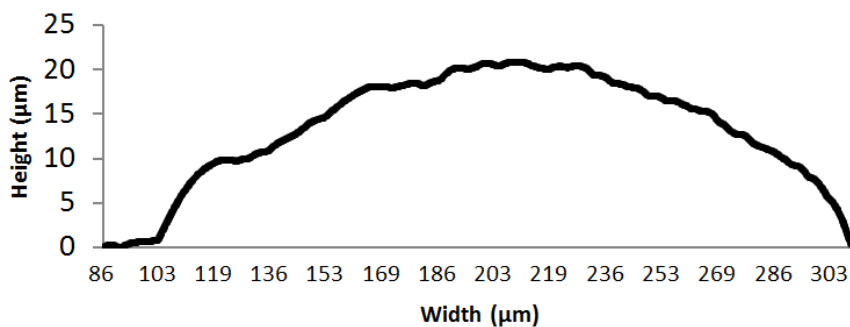


Figure 5.6. Surface profile at the cross-section of a conductive ink line [43].

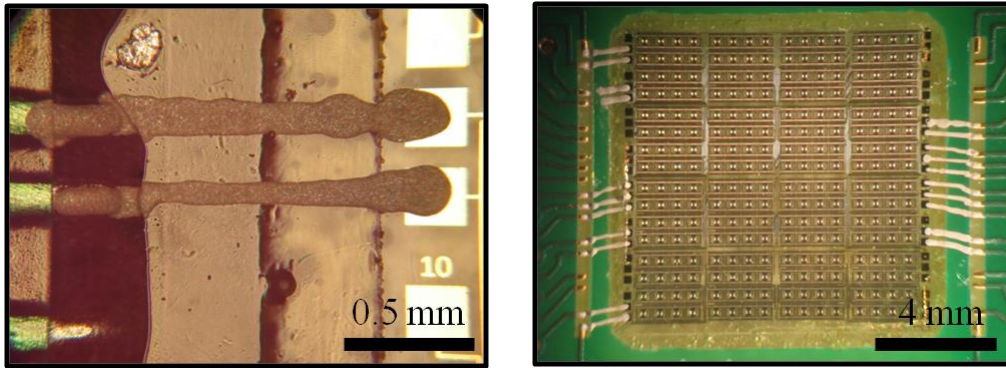


Figure 5.7. (Left) Conductive ink connections of two pads and (right) an overview of a completed PCB package.

The whole process of PCB packaging is shown in Figure 5.8. In the end, the electrical conductivity has to be tested to make sure there is no defect. The ink demonstrates excellent conductivity; the resistance is as low as 2Ω within 2 mm length of single line. The total capacitance of a group should be the summation of all connected groups in parallel. An extremely low resistance means something shorted which could be the ink or floating element itself. Unbalanced capacitance of top and bottom electrodes or lower capacitance then the expectation indicates the broken ink connections. Since all groups are wired up on-board, debug is more difficult and complex than the CPGA package on which all groups are independent. So it is the drawback of the PCB packaging.

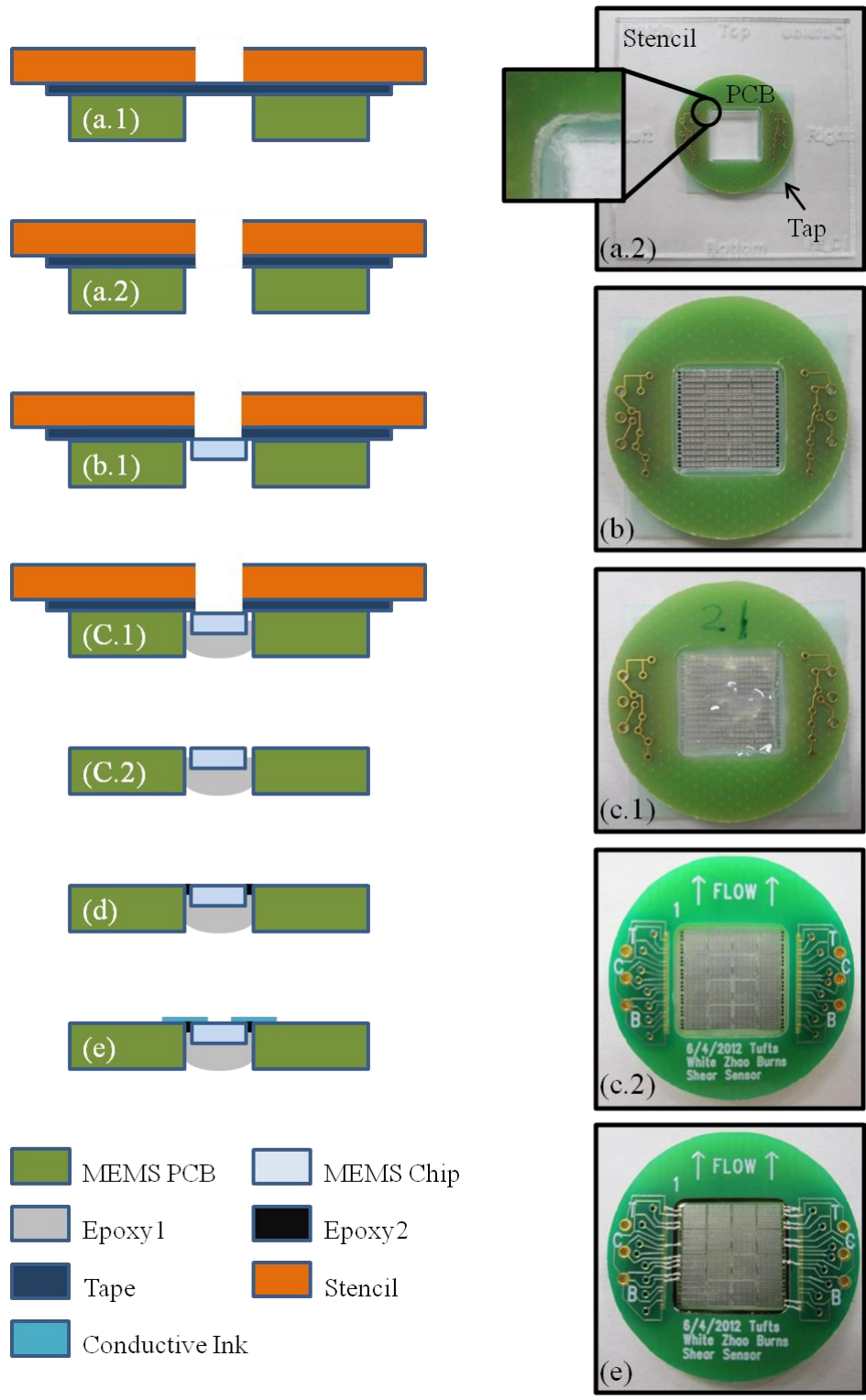


Figure 5.8. PCB packaging process using conductive ink: (left) cross-section schematics and (right) photos from top view.

5.2 Electronics

Three versions of electronics are designed and fabricated for use with the MEMS floating element shear stress sensor: (1) a MS3110 commercial chip, (2) an AD7747 commercial chip on a rectangular PC board, (3) an AD7745 commercial chip on a circular PC board. In all cases, the goal is to convert the scale (atto-Farad level) differential capacitance change on chip into either an analog or digital signal that can be read remotely.

5.2.1 MS3110

This first version of the electronics is composed of a printed circuit board (PCB), a MS3110 Universal Capacitive Readout™ IC [MicroSensors, Costa Mesa, CA], a capacitor, a few various connectors (power, output, programming), and a reset button. The board was designed by Shuangqin (Susan) Liu, a previous Ph.D student in the group. The PCB design shown in Figure 5.9 and MS3110 characteristic will be introduced below.

- 1) The PCB board surface dimensions are $9.4\text{ cm} \times 10.2\text{ cm}$, with a 15×15 zero insertion force (ZIF) socket mounted on the PC board, allowing the CPGA to fit into the flow cell mentioned in the next chapter. All pins are sorted and routed into three independent channels according to the electrode types.
- 2) 16 pin small-outline integrated circuit (SOIC) MS3110 chip is surface mounted on the back of the PCB. It includes an on-chip variable

capacitive DAC (CS_1 and CS_2) for initial differential adjustment of dual channels, a low pass filter of programmable cutoff frequency from 500 Hz to 8 kHz.

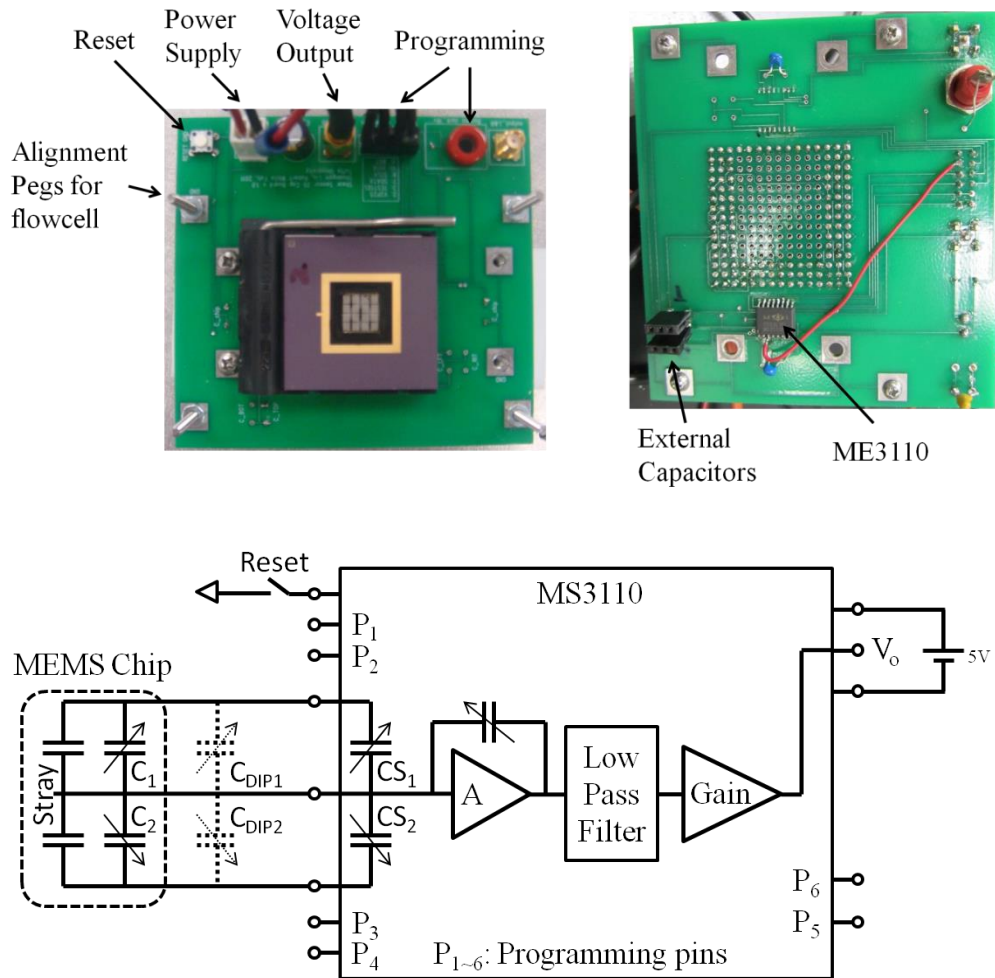


Figure 5.9. (Top) Front and back photos of the MS3110 electronics board and (bottom) schematic of MEMS chip and MS3110 chip system.

- 3) Dual channels of the MS3110 are connected to the top and bottom electrodes of the floating element (C_1 and C_2), respectively, thus, this differential measurement has an advantage to partially cancel out the mutual temperature, humidity or other environment noise that may

cause common mode capacitance change. The transfer function of the MS3110 chip is provided by the manufacturer

$$V_{out} = 2.565 \cdot GAIN \cdot \frac{(C_2 + CS_2) - (C_1 + CS_1)}{CF} + VREF \quad (5.1)$$

where $Gain = 2$ or 4 V/V nominal, CF is a feedback capacitor, and $VREF$ can be set to 0.5 V or 2.25 V DC. Therefore, the output voltage V_{out} will be proportional to the difference between top and bottom capacitance output.

- 4) The MS3110 chip is driven by 5 V DC from a power supply via a two-wire Molex header, and able to optimize the voltage output by programming the parameters in Eq. (5.1). The setting data either can be stored into an on-chip EEPROM permanently or sent out to the control registers directly. EEPROM requires another extra a 16 V DC power. Both writing modes are realized via the digital output channels of a data acquisition board.
- 5) The output of voltage uses subminiature version A (SMA) connector and sends to a voltage meter.
- 6) Since the internal variable capacitors (CS_{1or2}) are limited to 10 pF , two female headers on the back side are available to plug in two external DIP capacitors if the difference between two electrodes exceeds 10 pF .
- 7) Four 4-32 screws on the corners are used to align and assemble the flow cell (see the flow test setup in the next chapter).

5.2.2 AD7747

In a second version of the electronics, an AD7747 [Analog Devices, Wilmington, MA] capacitance to digital converter chip is used to measure the differential capacitance between the top and bottom electrodes on the MEMS chip and output a digital signal. The features of AD7747 chip are demonstrated as below.

- 1) The chip uses an AC excitation and a sigma delta modulator to measure differential capacitance changes of $\pm 8 \text{ pF}$.
- 2) It is capable of removing offset static differential capacitances as high as 17 pF .
- 3) On chip registers control the conversion rate, AC excitation level, and allow for nulling of any static capacitance offset.
- 4) The best results in terms of noise performance are achieved using the slowest conversion rate of 219.3 ms , and an excitation voltage level of $\pm 3/8$ of V_{dd} , which produces a voltage swing from 0.625 V to 4.375 V applied to the MEMS capacitors. With these settings the AD7747 is expected to provide a resolution of 20 aF and a noise floor of $11 \text{ aF}/\text{rtHz}$ according to the datasheet.
- 5) The temperature sensor is integrated in AD7747 by using an on-chip transistor to measure the temperature of the inside silicon chip.
- 6) The resolutions of capacitance and temperature are 20 aF and $0.1 \text{ }^\circ\text{C}$, and accuracies are 10 fF and $2 \text{ }^\circ\text{C}$, respectively.

The $76\text{ mm} \times 18\text{ mm}$ PC board (shown in Figure 5.10) is surface mounted with all electrical components simultaneously using solder paste: an AD7747 chip, two capacitors, a LED light (an indicator of power), a few capacitors ($0.1\ \mu\text{F}$ and $10\ \mu\text{F}$) and pull-up resistors. Two female headers are separately soldered on the ends for the MEMS chip connection and a microcontroller.

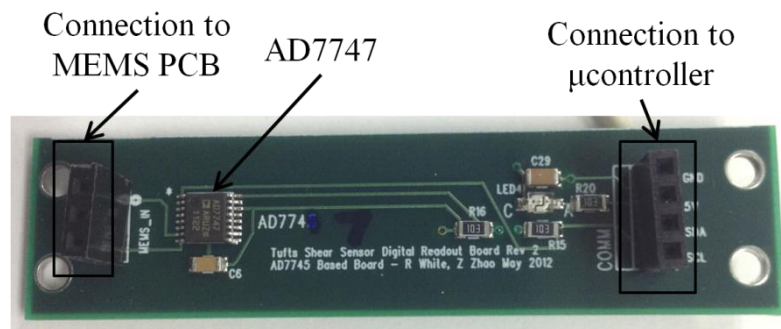


Figure 5.10. Photos of AD7747 electronics printed circuit board.

5.2.3 Microcontroller and DAC

Next, the AD7747 communicates with an Atmega328 microcontroller on an Arduino Uno board using the two-wire I²C protocol. The microcontroller then communicates with a computer over USB via an Atmega16U2 configured as a serial to USB converter, which is integrated on the Uno board as well. The speed of the system is limited by the conversion time of the AD7747. Shorter conversion times down to 22 ms can be used, but results in a lower capacitance resolution. A schematic of the system electronics is shown below in Figure 5.11.

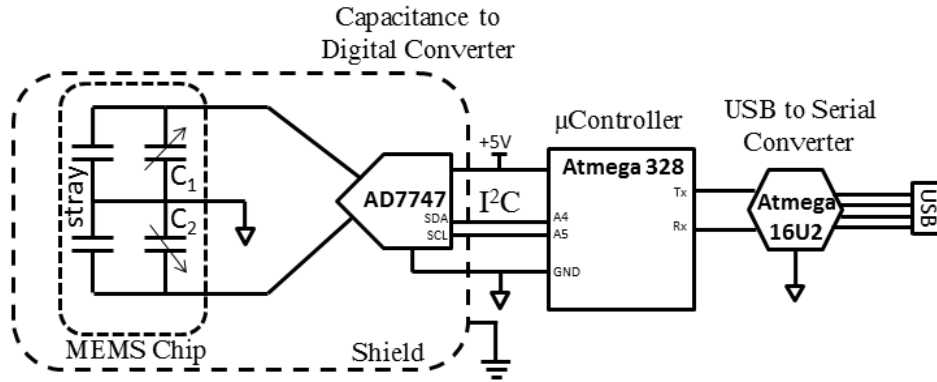


Figure 5.11. Readout electronics used an AD7747 capacitance to digital converter to perform differential capacitance measurements on the MEMS chip. Communication was via I²C to a microcontroller which then communicates over USB.

The digital signal has its own advantage of immunity to electromagnetic interference (EMI) when it is travelling to the next stage (computer), however, analog voltage is more convenient to read and display on a voltage meter. A small MCP4725 breakout board [Sparkfun, Boulder, CO] is used to convert digital into analog voltage as an alternative output.

Then, the microcontroller, digital-to-analog convertor as well as other components are combined together and stored in a metal enclosure as a shield. Besides a digital output via type B USB and an analog output via a BNC connector, Figure 5.12 is presenting additional functionalities, included reset of the EEPROM storage, two LED lights to indicate power and recording, and the extra power availability when no USB power. Ground sides of each part are attached to the wall of box.

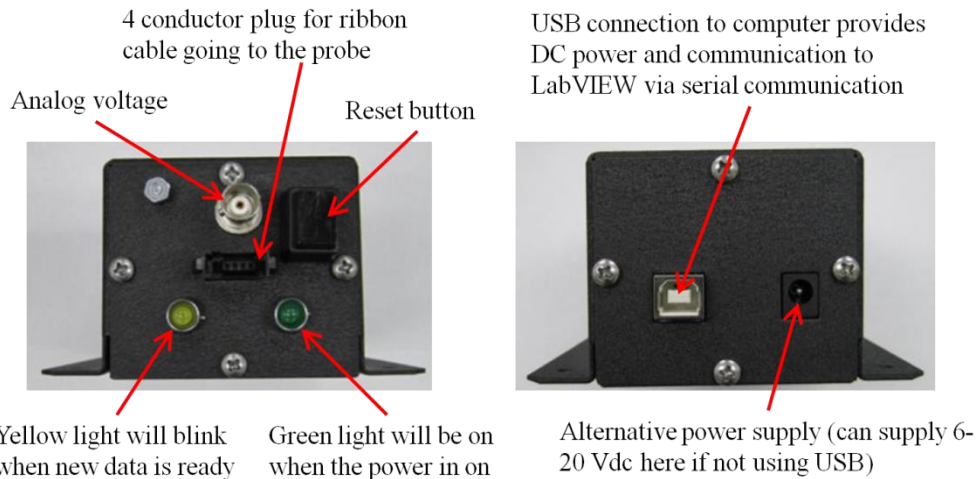


Figure 5.12. Interface of the box with the microcontroller and DAC board inside.

5.2.4 AD7745

MS3110 and AD7747 electronics are used to detect the capacitance of the CPGA package. Both of these chips work with the larger stray capacitance that is present in the CPGA packaged chips. The third electronics design, using an AD7745 chip, is designed for the PCB packaged MEMS chip and fits into the tube housing to create one probe with both MEMS chip and electronics. The AD7745 has higher capacitance resolution, but only works with the lower stray capacitance achieved with the PCB packaged. Since this design is intended to fit behind the sensor in a cylindrical can, instead of a rectangular board, an AD7745 is mounted on the circular PC board as same size as MEMS PCB package. The electronics design is introduced here, and the probe assembly will be covered in the next section.

An AD7745 is also digital capacitance readout chip with slightly difference with AD7747.

- 1) The center of AD7745 connected to the common electrode of the MEMS sensor is excited and has not to be grounded, which is good for floating capacitive sensors.
- 2) AD7745 gives a better resolution of 4 aF and a better noise floor of 2 $aF/rtHz$, compared with 20 aF and 11 $aF/rtHz$ for the AD7747.
- 3) The AD7745 is not appropriate to CPGA package is because it cannot drive and read the static capacitor larger than 60 pF , while the AD7747 can go up to 110 pF . The capability of MS3110 is not clear, but larger than 570 pF . The parasitic capacitances of empty CPGA and PCB package are 70 pF and 5-10 pF , respectively. 1 cm^2 square glass and silicon chips of such floating element sensor have parasitic capacitance of approximate 45 pF and 500 pF , considering all elements. So, the floating element shear sensor on a glass packaged on a PC board does not require any extra amplifier or buffer and can be measured with a single AD7745 chip directly. It is significant benefit on reduction to the size of the sensor package.

The PCB board of AD7745 is shown in Figure 5.13. On-board components are minimized into two capacitors only in order to fit them into 24 mm diameter PCB. They are surface mounted on the same side as AD7745 with the solder paste again. A four-pin Molex connector as an interface to the microcontroller is soldered on (the flat side must be towards to the center), which is not in the figures. Four pairs of silver boxes in the center of front

photo is able be coupled variously to achieve an appropriate circuit for either AD7745 or AD7746. AD7746 is identical to AD7745 but two capacitive channels that can separate the left and right floating elements on the MEMS chip. Use of AD7746 will be introduced at chapter 7. For AD7745 application, the pairs of a/b/d are connected to themselves to combine the T/C/B on the left and right.

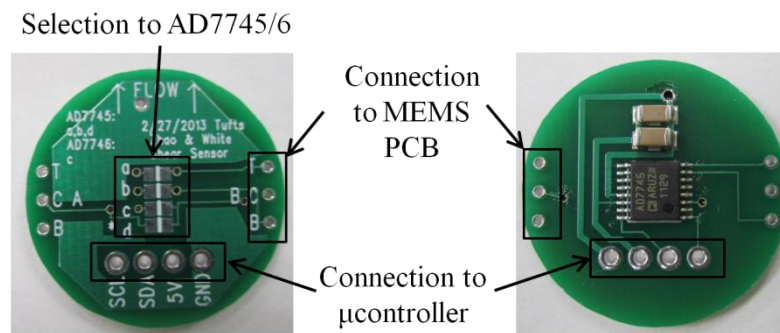


Figure 5.13. Front and back side of the circular AD7745 electronics

5.3 Probe Assembly

This section introduced how to assemble the two circular PC boards of MEMS chip and AD7745 electronics as well as the advantages compared with CPGA package.

First, an acrylic stand-off with $17\text{ mm} \times 17\text{ mm}$ cutout (see Figure 5.14) is used as a base to allow the MEMS package facing down and the rest parts will be built from its back side.

Second, two sets of three-pin male header are soldered into “T”, “C”, and

“B” holes on the left and right sides. Due to the acrylic stand-off, their heights are well controlled in order not to protrude from the sensor surface. A 12 *mm* long and 25 *mm* outer diameter Aluminum tube is slid along the PC board and they are tightly fit to each other. Next, the E-60NC epoxy is applied to seal the MEMS PCB and tube and fill the possible gap between them. Any tiny gap will result the flow leak and influent the flow pressure as well as shear stress. Curing of the epoxy requires more than 10 *hr*.

Finally, the completed AD7745 electronics PC board is piled up and aligned with the six pin heads and the flow direction arrow. This is a loose fit to compromise the assembly and manufactured errors. Following the solder of pins on the electronics, the high viscous epoxy is sealed the edges to secure the other end of the tube. The completed probe sensor with an acrylic cap is demonstrated at the bottom of Figure 5.14.

Three major advantages of the probe configuration are introduced here.

- 1) The AD7745 is located close to the MEMS chip, which helps to reduce EMI. The probe output is already digitalized.
- 2) The AD7745 is enclosed into an Al tube as a grounded shield. That is the purpose of ink trace between “GND” on the electronics and the tube wall as so to ground the tube.
- 3) Generally, the small sensor broadens the application and simplifies the implementation, such as mounting on the airfoil surface.

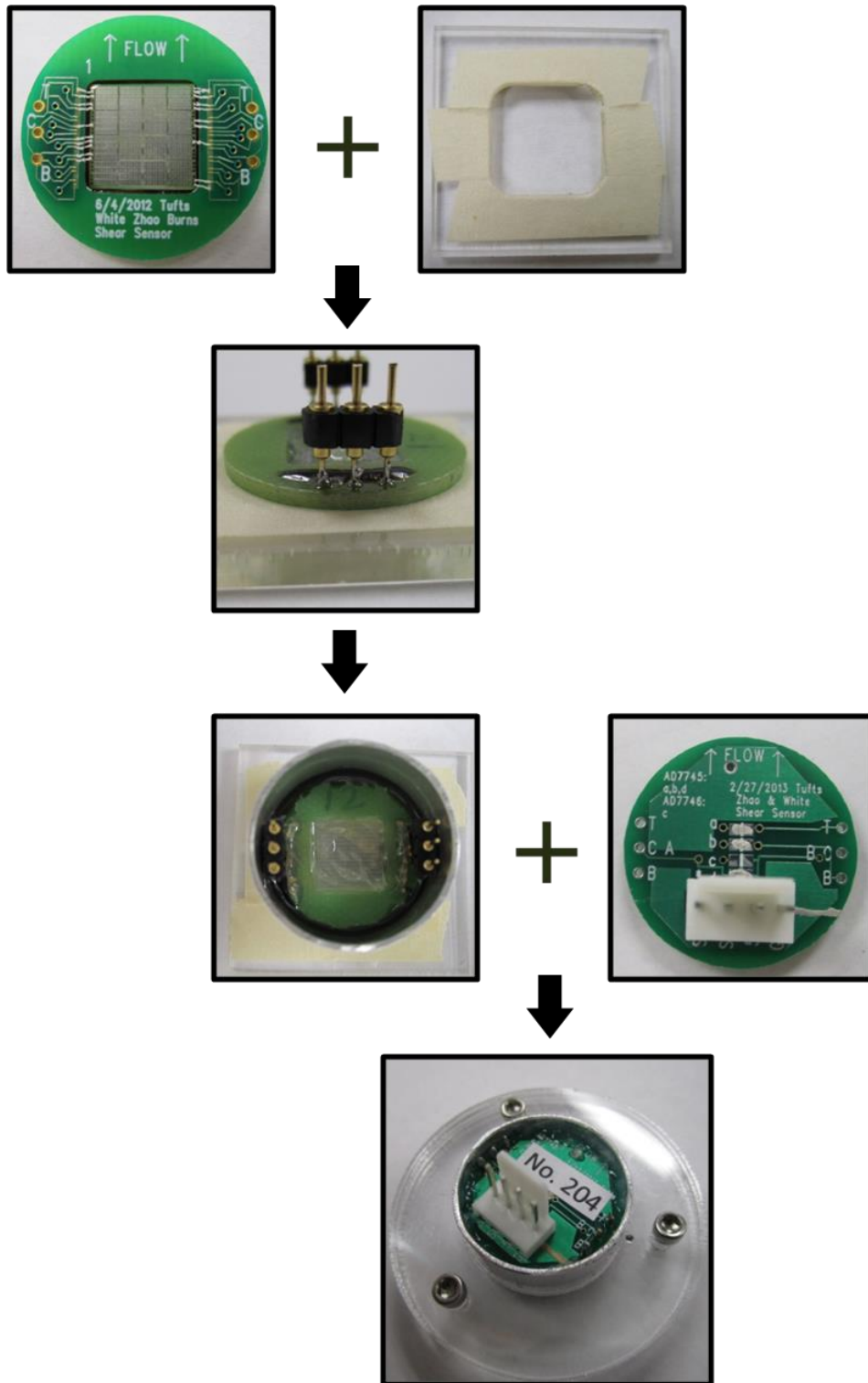


Figure 5.14. Assembly of MEMS chip and AD7745 electronics into an Al tube as small as possible.

Chapter 6

Characterization

The chapter is broken up into three parts: (1) Mechanical/electrostatic characterization using Laser Doppler Velocimetry (LDV) and Inductance-Capacitance-Resistance (LCR) meter, (2) the shear stress sensor characterization in the laminar flow of flowcell at Tufts laboratory as well as the pressure gradient calibration, and (3) the shear stress sensor characterization under the turbulent boundary layer (TBL) in a wind tunnel at NASA Ames research center. Primary laminar flow measurements are conducted on the different packaging and electronics approaches and evaluate their own performances. The best scheme is selected to determine the shear stress and pressure gradient sensitivities of the floating element sensor. The TBL test demonstrates successful operation in a wind tunnel application.

6.1 Electromechanical Calibration

Laser measurements and electrostatic actuation introduced in the first section are used to detect the resonant frequencies, snap down voltage, and dynamic motion of the element.

6.1.1 LDV Measurement

Laser Doppler Velocimetry (LDV) is a technique of using the Doppler shift in a reflected laser beam to measure the velocity (or displacement) in a vibratory motion of a surface.

A Polytec OFV 511 fiber interferometer along with a Polytec OFV 3001 vibrometer controller are used to measure the out of plane motion of the center shuttle while the floating element is driven by the Agilent 33220A function generator at a constant voltage through a series of frequencies. In this mode of operation, the sensor is driven electrostatically by varying the charge on the comb fingers. In the vibrometer controller, the resulting signal is decoded using the displacement decoder with a low pass filter at 2 *MHz*, and then the displacement output, at a sensitivity of 50 *nm/V*, is recorded using a NI PCI-4451 high speed data acquisition (DAQ) board. The laser source is set up on an optical table to absorb the vibration coming from the floor and pointing vertically at the center of the floating element. The laser direction is adjusted as perpendicular as possible to the chip surface so as to maximize the reflection strength, which is indicated on the signal level of the fiber

interferometer. A probe station is used to send a DC+AC driven voltage to the electrodes on the sensor. This measurement is completed on the 1 *cm* MEMS glass chip prior to the packaging step to determine whether the sensor is functional or not. The system also can be tested in this manner once the sensor is packaged.

The displacement response of an individual floating element over the frequencies range of 1-500 *kHz* is shown in Figure 6.1. First three modal frequencies between 10 *kHz* and 50 *kHz* are detected and in the same order as the prediction, compared to the simulation in chapter 3. This implies the sensor is successfully released and that the dynamics are similar to expected. The decreasing shift (10-20%) of all modes of frequency indicates the floating element is slightly more compliant than the simulation. This might be caused by the rigid body assumption on the shuttle region, geometric measurement errors, or additional compliance in the boundary conditions not included in the simulation.

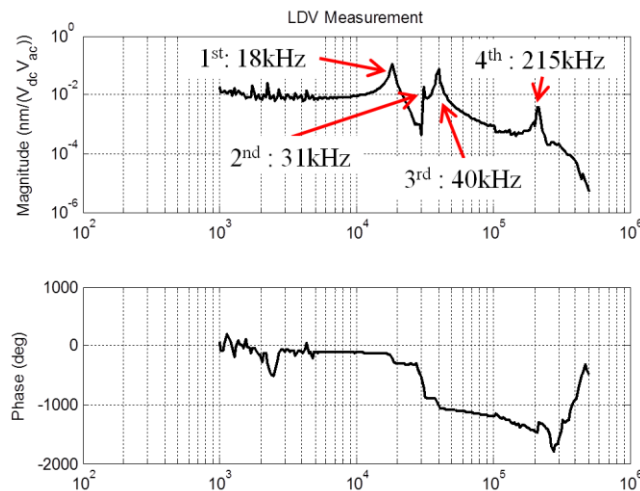


Figure 6.1 Displacement response of a single floating element using Laser Doppler Vibrometry and first four modal frequencies are found.

6.1.2 C-V Measurement

Capacitance-voltage (C-V) measurement is a technique to apply a series of DC voltages and measure the capacitance as a function of voltage. An Agilent E4980A Precision LCR Meter is computer controlled to generate 101 voltages between -40 V and +40 V. At each DC bias, capacitance is measured using a 1 kHz frequency test signal that is applied on the top electrode of one sensor group, with the common electrode grounded. The capacitance values are measured and plotted in Figure 6.2.

If in plane motion along the finger direction, and neglecting other possible motions, the electrostatic force at one element, F , is defined as

$$F = \frac{N\epsilon t}{2d} V^2 \quad (6.1)$$

where V is a series of voltage between -40 to 40. And, the displacement of center shuttle, Δx , is given by

$$\Delta x = \frac{F}{K_x} \quad (6.2)$$

Then, the C-V function between the top and common electrodes of one group can be expressed by substituting Eq. (3.11), (6.1), (6.2) into Eq. (3.19),

$$\Delta C = \frac{nN\epsilon t}{d} \Delta x = \frac{ntN^2\epsilon^2 L^3}{4Ed^2 w^3} V^2 \quad (6.3)$$

where $n=16$, is the number of elements in a group. The parabolic curve does agree with the second order relationship of C-V. However, Eq. (6.3) indicates as small as 0.08 fF change at 40 V, which is 50 times less than measured in Figure 6.2. It might be caused by some extra motions besides

in-plane direction. The gold wires under the nickel floating element are a likely reason producing a vertical electrostatic force pulling down the center shuttle in the out-of-plane direction, and also introducing a twisting moment. More modeling is needed to fully understand and match up the C-V measurement. Additionally, it is obviously that the sensor is able to survive to 40 V without snap down, which is of help to some future actuation applications, for instance, feedback control.

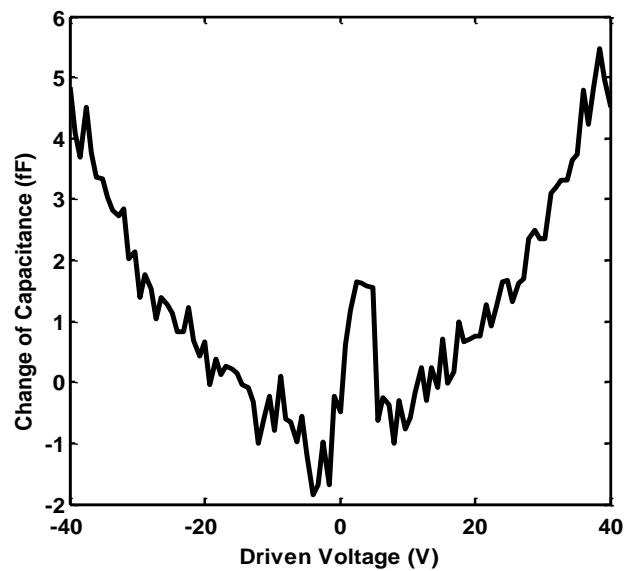


Figure 6.2. The change of capacitance as a function of driven voltage on one side of one floating element group.

6.2 Laminar Flow Test

The section is focused on: (1) the laminar flowcell design, giving dimensions, flow cell properties, pressure tap measurement information and the expectation of shear stress at the different flow rates, (2) the characterization setup for the different sensor configurations and the sensor characterization in laminar flow. This will include the distinction between the shear stress sensitivity and pressure gradient sensitivity.

6.2.1 Flowcell Design

The floating element sensor is tested in a laminar flowcell, similar to that described by other authors [25]. A duct flow channel illustrate in Figure 6.3 is created by CNC milling a thin rectangular slot into an aluminum plate, and assembling this with a flat bottom plate with a rectangular cutout for flush mounting the package. The slot is 28 *mm* wide, and three different height slots,

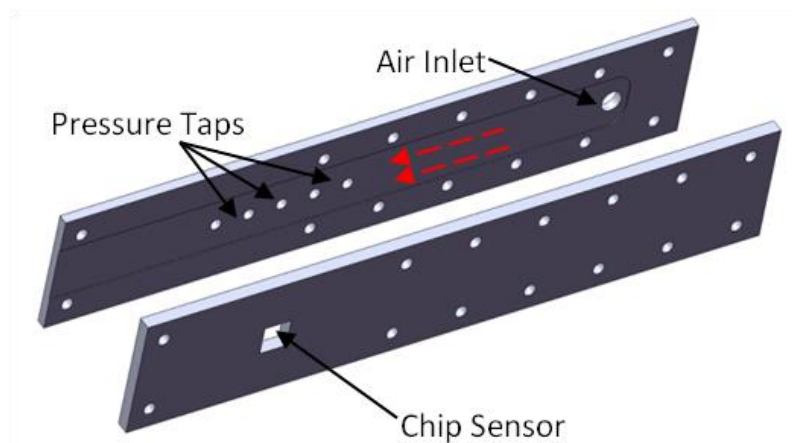


Figure 6.3. A schematic of a disassembled Flowcell.

0.30, 0.40 and 0.53 mm, are used in order to distinguish between the shear stress and pressure gradient sensitivity. The shallow and wide slots produces a high aspect ratio (~ 70) flow channel in order to reduce the entrance length, and obtain high shear stress and fast flow speed at achievable pressures. The inlet air supply is house clean dry air, and is regulated via computer control using a digital flow controller, Omega FMA3812 [Omega Engineering, Stamford, CT]. This unit controls the total volume flow rate from 0 to 40 cubic feet per hour (CFH). The outlet flow exits to atmosphere. Figure 6.4 is a diagram of the test setup.

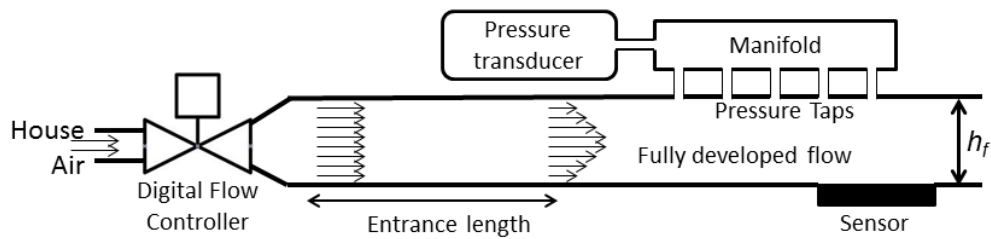


Figure 6.4. Diagram of the laminar flow cell test apparatus.

For flow rates of 40 CFH or less, the flow in the duct is laminar, and so the flow can be described by a Poiseuille flow profile for a narrow slot [37],

$$u(y) = \frac{6Q}{b_f h_f} \left[\frac{1}{4} - \left(\frac{y}{h_f} \right)^2 \right] \quad (6.4)$$

where Q is the volume flow rate, b_f is the duct width, h_f is the duct height, and $y = -h_f/2 \dots h_f/2$ is the coordinate. At $Q = 3.15 \cdot 10^{-4} \text{ m}^3/\text{s}$ (40 CFH), for the smallest duct, the centerline velocity (when $y = 0$) is 56 m/s and average velocity is 2/3 of the centerline, resulting in a centerline Mach number of 0.16

and an area averaged Mach number of 0.11. Hence, even at the highest flow rates, the flow can be considered incompressible.

The Reynolds number based on the average flow velocity and hydraulic diameter is

$$\text{Re}_{D_h} = \frac{2\bar{u}\rho h_f}{\mu} = \frac{2Q\rho}{b_f\mu} \quad (6.5)$$

where $\rho = 1.2 \text{ kg/m}^3$ is then air density, $\mu = 1.8 \cdot 10^{-5} \text{ Pa}\cdot\text{s}$ is the dynamic viscosity of air. As can be seen, Reynolds number does not vary with duct height. At the maximum flow rate of $Q = 3.15 \cdot 10^{-4} \text{ m}^3/\text{s}$ (40 CFH), $\text{Re}_{D_h} = 1500$. Transition to turbulence in parallel plate flow occurs above a Reynolds number of 2000 [37], thus the flow is expected to remain laminar, for all duct heights, up to the highest flow rate tested.

Given this, the pressure gradient and wall shear stress are expected to be

$$\frac{\partial p}{\partial x} = \frac{-12\mu Q}{h_f^3 b_f} \quad (6.6)$$

and

$$\tau = \frac{-1}{2} h_f \left(\frac{\partial p}{\partial x} \right) = \frac{6\mu Q}{h_f^2 b_f} \quad (6.7)$$

Five static pressure taps are included on the top of the channel along the streamline, with a pitch of 12.7 mm, to measure the pressure gradient in the fully developed region. The entrance length is depended on Reynolds number and hydraulic diameter, and for laminar flow, it is expressed as

$$L_{en} = 0.06 \cdot \text{Re}_{D_h} \cdot D_h = \frac{0.24Q\rho}{\mu} \left(\frac{h_f}{b_f} \right) \quad (6.8)$$

At the maximum flow rate and tallest duct, the entrance length is approximate 95 *mm*. The 1st pressure tap is located more than 95 *mm* from the entrance. The 5th pressure tap is located directly above the sensor. The static pressure is measured using an Omega PX209 pressure transducer [Omega Engineering, Stamford, CT].

The initial test of the measured pressure gradient is shown in Figure 6.5, and exhibits excellent agreement with the expectations of Eq. (6.6), giving considerable confidence that the flow is fully developed and laminar, and that the shear stress of Eq. (6.7) is accurate. Since pressure gradient and shear stress scale as hf^{-3} and hf^{-2} respectively, it is possible to produce laminar flow regimes with linearly independent values of the two fluid forcing terms by varying the duct height. Advantage will be taken of this fact to independently determine the two sensitivities of shear stress S_2 and pressure gradient S_3 .

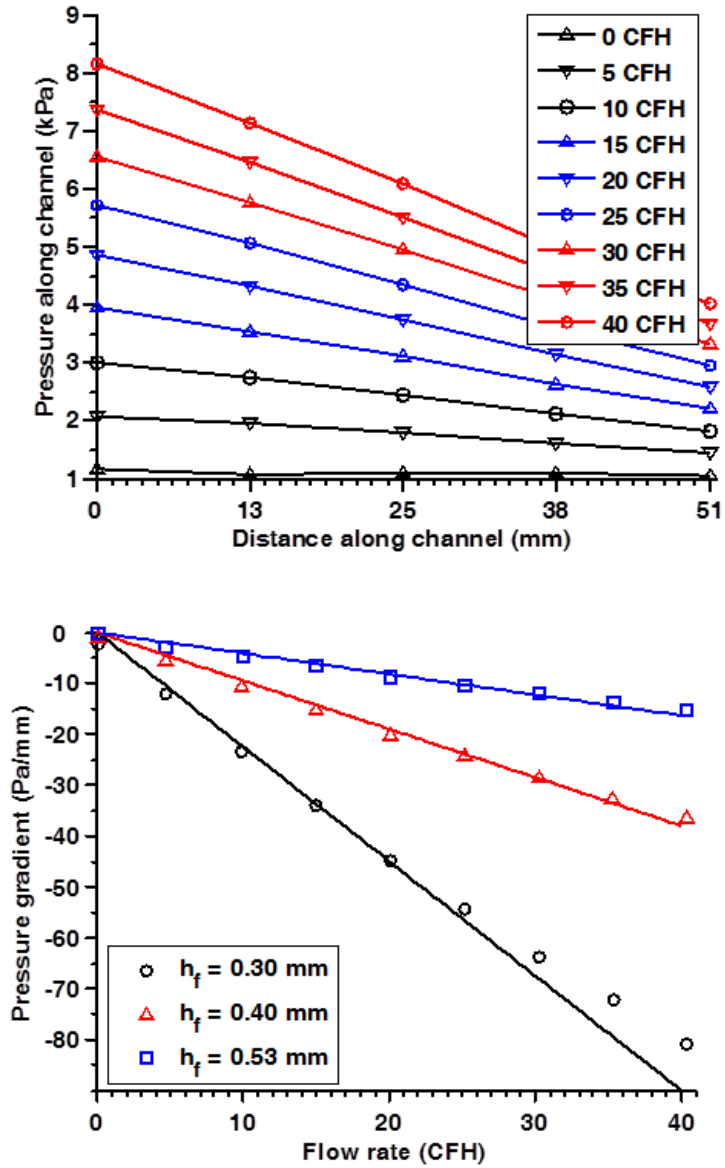


Figure 6.5. (Top) Measured pressure as a function of distance down the duct for different flow rates in the $h_f = 0.30$ mm high duct. (Bottom) Measured pressure gradient as a function of flow rate (symbols) compared to the Poiseuille flow model (lines), Eq. (6.6), plotted for the three duct heights.

6.2.2 Experimental Setup

The flowcell with the pressure taps/transducer, plus the flow controller, provides the laminar flow environment and the calibrated shear stress and pressure gradient for the sensor characterization. In addition, the testing setup consists of a base to support the electronics and flowcell, a DAQ board, a voltage meter, and power supplies. The setups are modified as needed due to three different sorts of sensor electronics.

CPGA Package + MS3110 Electronics

Figure 6.6 shows the experimental setup with the CPGA package and MS3110 electronics board. The PCB board is mounted on the four standoffs and assembled with the flowcell using four screws, as shown on the top image. The electronics and pressure transducer are included in a faraday cage to isolate them from external EMI, and the BNC and DB9 connections are accessible through the connectors on the cage's wall. The other features are placed outside the faraday cage, shown in the bottom image. The analog channels of NI PCI-6251 DAQ board are driving and reading the digital controller; the flow rate is proportional to the voltage at a rate of 5 *CFH* to 40 *CFH*. The digital channels 0-4 are used to set the parameters of MS3110 chip. A small power supply generates 12 V for the pressure transducer, and a multi-channel power supply is serving as the source for the MS3110 and the flow controller. The pressure gradient and sensor voltage are recorded and displayed separately by a HP E34401A voltage meter instead of the DAQ,

because of the better resolution of the voltage meter and avoidance of the cross-talk effect on the DAQ analog channels connected to the flow controller (the sensor voltages change on the order of 1 *mV*).

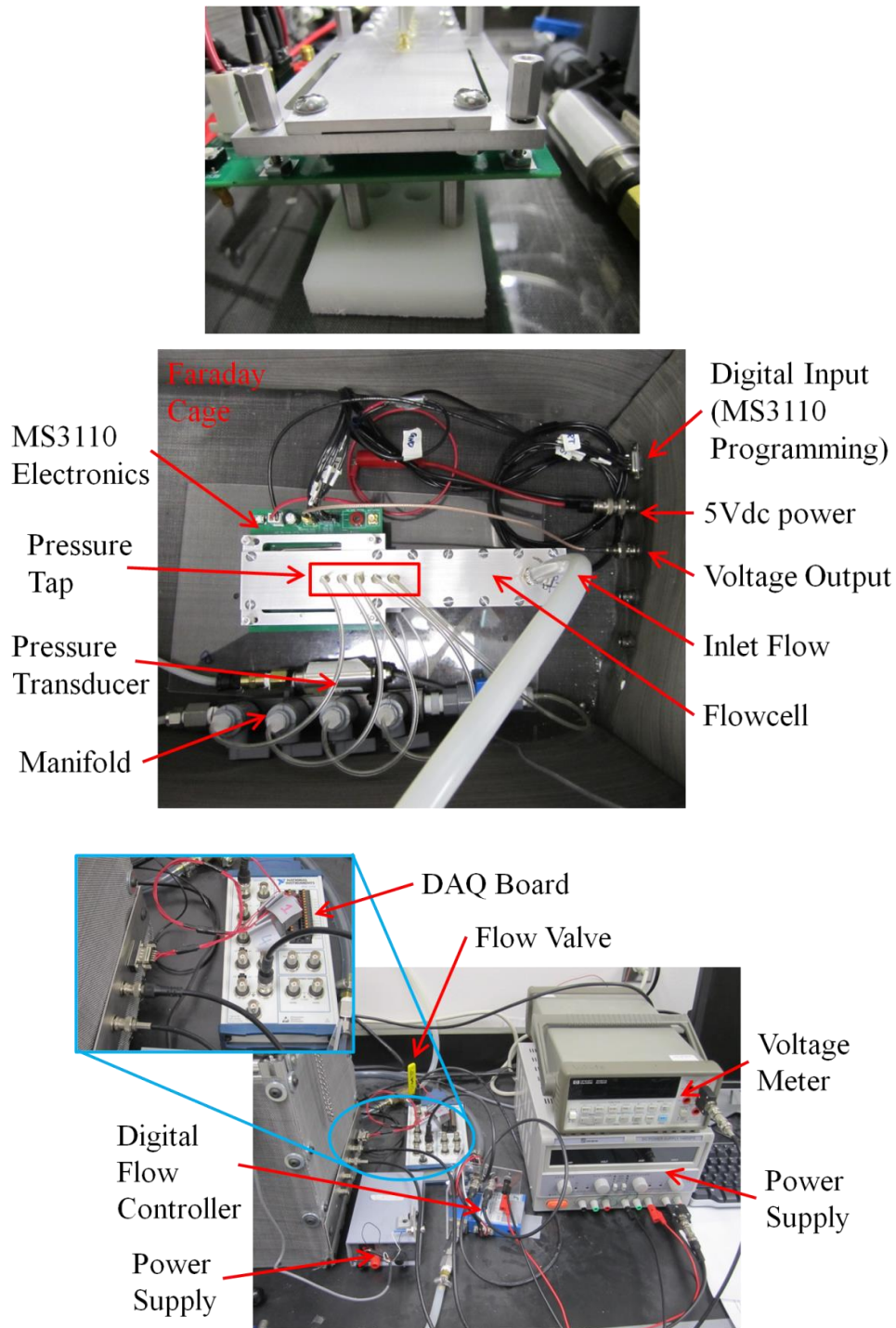


Figure 6.6. The laminar flow experimental setup of the MS3110 electronics: (top) inside faraday cage, (bottom) outside faraday cage.

CPGA Package + AD7747 Electronics

This setup is very similar with the MS3110. The sensor package, electronics, and the flowcell are protected from EMI noise in the faraday cage, and the laboratory instruments are outside. Figure 6.7 shows that one difference is the electronics only. The MS3110 PC board is replaced by another PCB attached with ZIF socket and two female headers only (no electrical parts) to support the CPGA package and assemble with the flowcell. The AD7747 electronics directly measures the differential capacitance of CPGA and then communicates to the microcontroller via a four wire ribbon cable. Figure 6.7 also shows another small faraday cage covers the AD7747 chip in order to reduce the EMI noise inside the larger faraday cage, which is possibly generated by the pressure transducer. AD7747 electronics is able to bring in the following advantages to the experimental setup.

- 1) The signal digitalization is completed in the cage and immunity to the noise no matter how far it has to travel to the next stage.
- 2) The analog voltage cable between the DAC box and a voltage meter is reduced as short as possible, if used.
- 3) DC power, AD7747 chip registration, and data communication are all integrated into a signal 4-wire ribbon cable, compared with the connections for MS3110 chip.

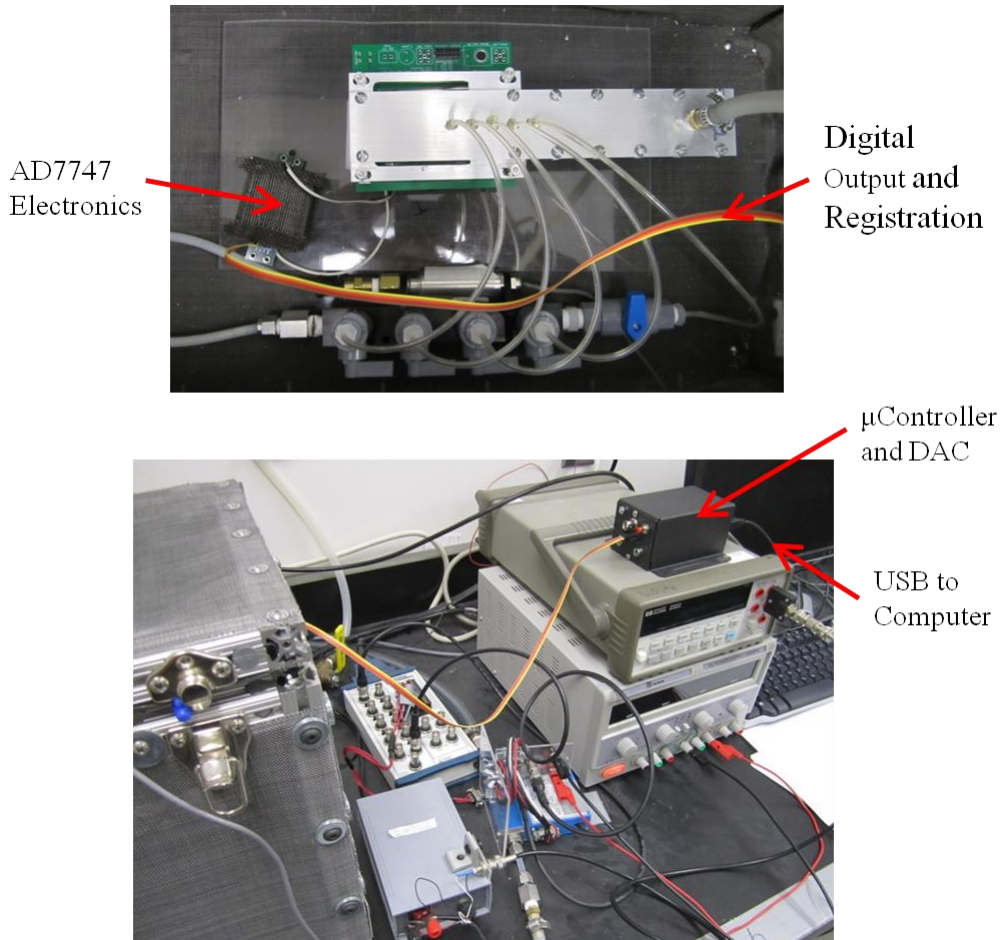


Figure 6.7. The laminar flow experimental setup of AD7747 electronics: (top) inside faraday cage, (bottom) outside faraday cage.

PCB Package + AD7745 Electronics

The off-sensor structure is identical to the AD7747 setup, and only the sensor support is re-designed to fit to the cylindrical sensor. First, the probe is slid into an aluminum plate with the circular cutout which is slightly larger than the probe diameter, and secured with two set screws on the left and right sides. Modeling clay is used to seal the gap around the sensor probe and cleared by a razor blade, as shown in the top photo of Figure 6.8. The Al plate is then mounted on an 80/20 base frame. Finally, assembly with flowcell on the top is able to maintain the sensor inside the laminar flow

channel. The entire setup is illustrated at the bottom Figure 6.8.

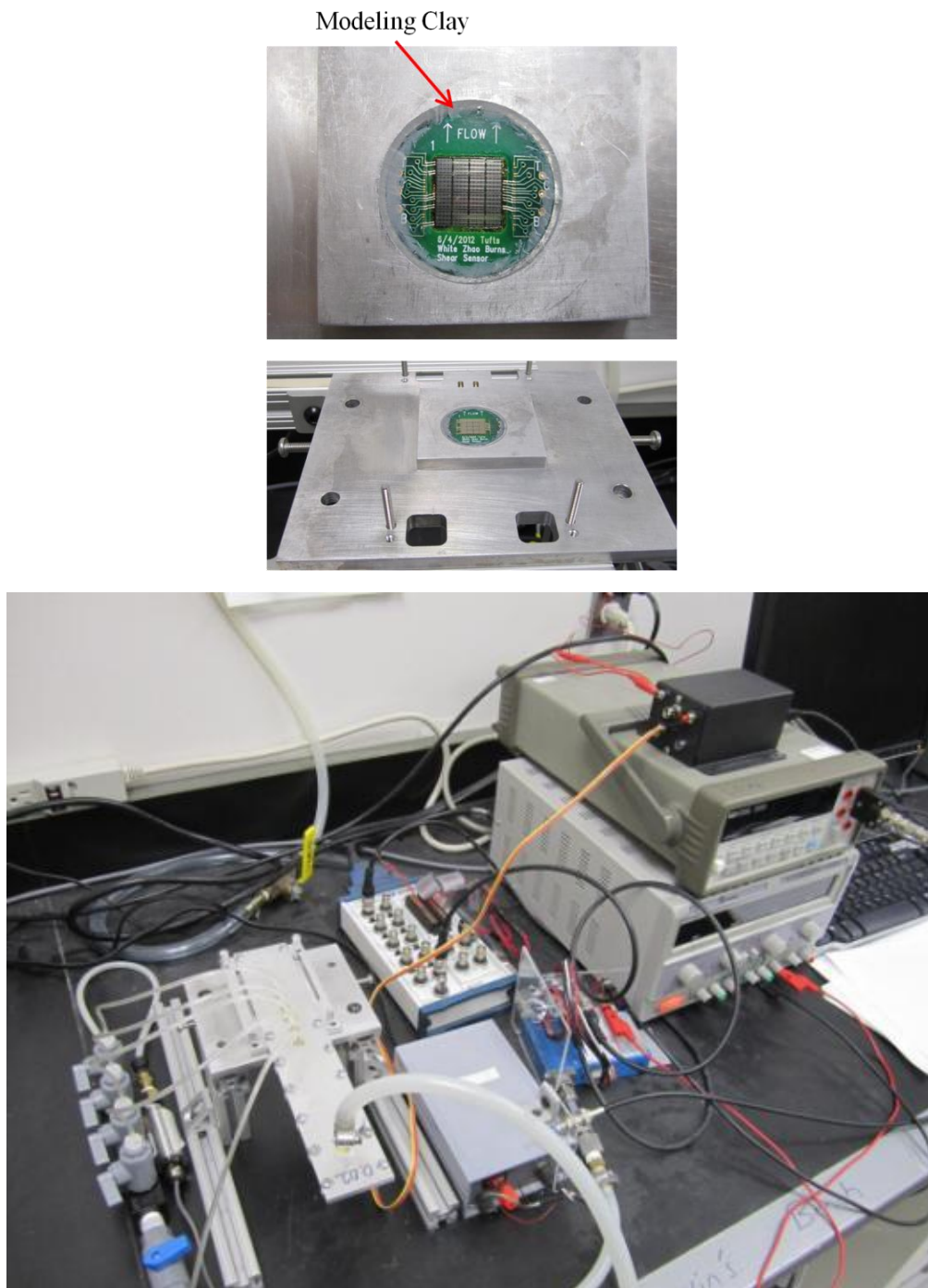


Figure 6.8. (Top) the sensor is flush mounted on a plate and modeling clay seals the edges, and (bottom) entire setup for the probe sensor.

6.2.3 Flow Measurement

These three setups are characterized at the smallest flowcell ($h_f = 0.3 \text{ mm}$), which will directly provide the signal output (either voltage or capacitance) as a function of flow rate. They will be compared in terms of the sensitivity, resolution, and noise floor in the end of this section.

Before running the flow and sensor measurement, the electronics are turned on for two hours with no flow, and then the flow is turned on at 10 *CFH* for an additional two hours. This conditioning is found to remove startup transients that are otherwise observed, no matter what kind of electronics is used. The startup transients appear to be related to ambient temperature and humidity, as well as surface charging of the glass, but the mechanisms are not well known. More work is needed to determine the source of startup transients and eliminate them. Hysteresis is not observed experimentally.

After the 4 hour turn on and soak, the flow rate is controlled by the computer via the digital flow controller starting at a low flow rate, and increasing to 40 *CFH* in steps of 5 *CFH*. The flow rates used for characterization are read and computed from the voltage output in the flow controller. The measurements from the three schemes are demonstrated as follows.

CPGA Package + MS3110 Electronics

For the CPGA package, 10 of the 16 groups on the chip are wire-bonded

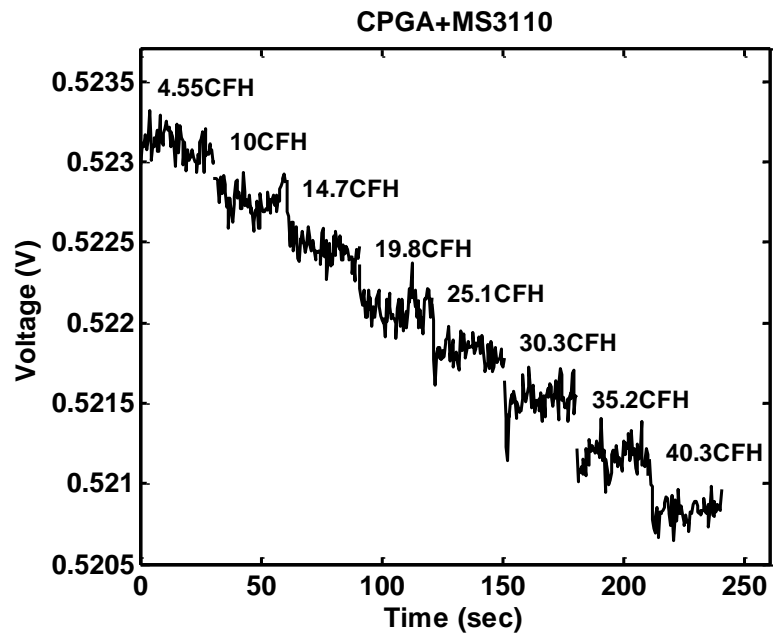
in parallel, so the output is the total capacitance change from 160 elements. The flow is starting at 5 *CFH*, running up to maximum flow rate of 40 *CFH* at steps of 5 *CFH*, going down to 5 *CFH* directly, stepping up to 40 *CFH*, and so on for 5 cycles. Each flow rate is held for 30 *sec*. Since the data rate is 2.3 samples/*sec*, there are 70 measured values at each flow rate.

Figure 6.9 indicates the calibration results of voltage output when the MS3110 readout chip is programmed as $Gain=2$, $CF=11.3$ *pF* (see Eq. (5.1)).

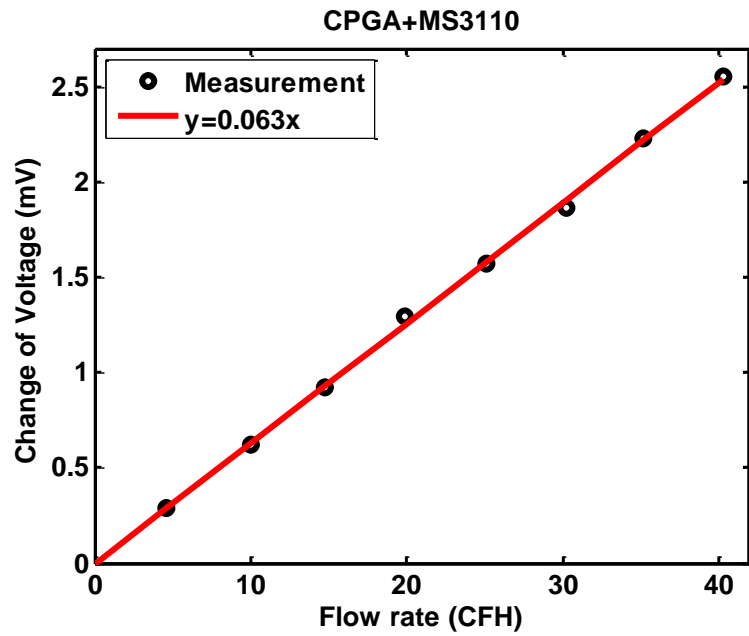
- 1) Since the top electrodes of MEMS chip is connected to C_1 and bottom goes to C_2 in the MS3110 transfer function (C_2-C_1), the plot (a) shows a decreased voltage as the flow increasing. The other three plots are flipped on sign.
- 2) Below 5 *CFH* steady state error of feedback control in the flow controller is observed.
- 3) The standard deviation of the capacitance about the mean for the time domain data gives the noise density of the measurement. For the data in plot (a), the standard deviation σ is 89 μV at a sample rate F_s of 2.3 samples/*sec*. A plot of the power spectral density of the voltage noise show that it is white noise. The noise density of the measurement is related to the stander deviation by

$$P_x = \sqrt{\frac{2\sigma^2}{F_s}} \quad (6.9)$$

Hence, the noise density in such measurement is 83 $\mu V/rtHz$ at low frequencies, which is approximate 0.2 *fF/rtHz* based on Eq. (5.1).



(a)



(b)

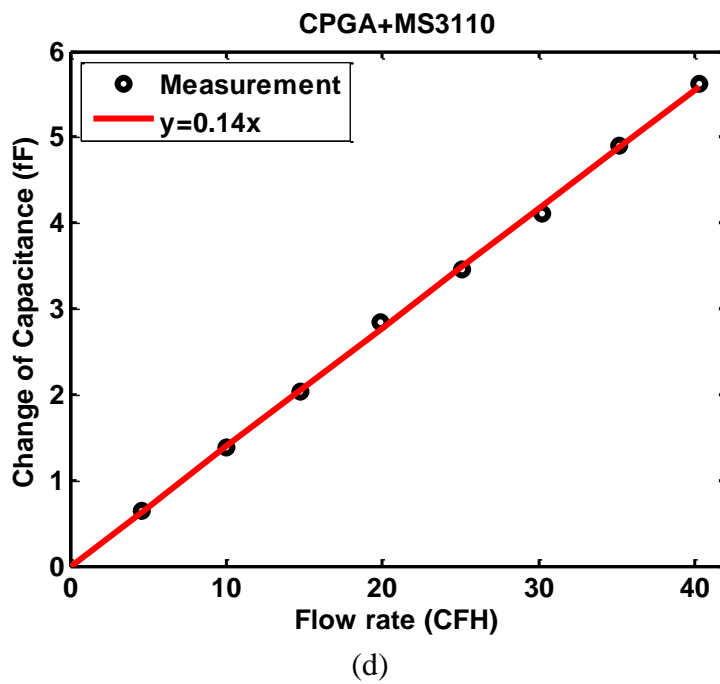
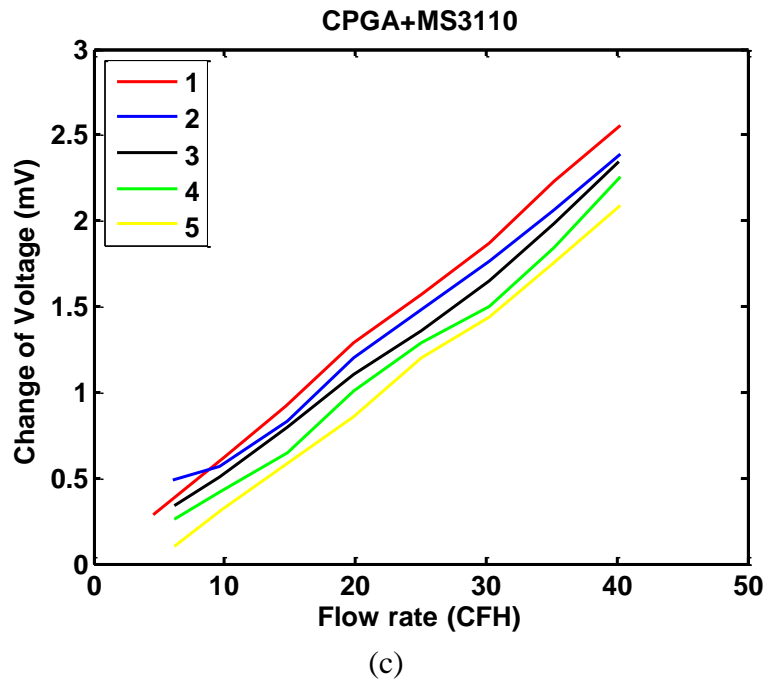


Figure 6.9. Measurement of 10 groups of floating element sensor arrays on a CPGA with MS3110 electronics in the 0.30 mm high laminar flowcell: (a) time domain voltage data at each flow rate, (b) change of voltage averaged at each flow rate in one cycle with linear fitting, (c) repeatability in five cycles, (d) and converted capacitance plot according to the MS3110 transfer function.

- 4) The sensitivity of change of voltage to flow rate of 10 groups sensor is shown in plot (b), $63 \mu V/CFH$, and plot (d) is the transferred sensitivity about capacitance. Thereby, the sensitivities of one group are obtained as measured $6.3 \mu V/CFH$ and converted $14 aF/CFH$.
- 5) The linearity is demonstrated up to the maximum flow rate, less than 2% nonlinearity at $40.3 CFH$.
- 6) The dynamic range (dr) is defined as the ratio between largest flow rate (Q_{max}) and smallest detectable flow rate (noise flow):

$$dr = 20 \log_{10} \left(\frac{Q_{max}}{P_x/s} \right) \quad (6.10)$$

where s is the sensitivity. In such measurement, the dynamic range is therefore $30 dB$ at 1 Hz band.

- 7) The plot (c) shows the experimental repeatability and consistent sensitivity. After settling to steady state, the average of drift is approximate $16 \mu V/min$, which equates to $36 aF/min$.

Time vs. Flow rate

Figure 6.10 shows the continuous flow rate response from 0 to $40 CFH$ and transition between each two rates. The overshoot in flow transition happens always, and that is also the reason to the overshoot at every beginning as the flow rate changes in the plot (a) of Figure 6.9. The longest settling time is $28 sec$ occurring at the ramp to $5 CFH$, and the flow stabilizes rapidly as the flow moves faster. The flow fluctuation is avoided in the rest of the

laminar flow testing with the other two electronics. The new flow conditions are that each flow rate is held for 60 seconds, and the first 30 seconds at each flow rate are not integrated, to allow the flow and sensor to settle, the sensor is measured during second 30 seconds.

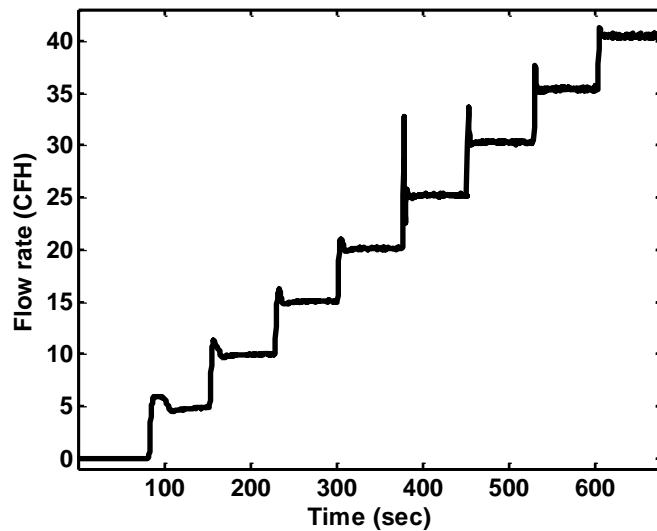


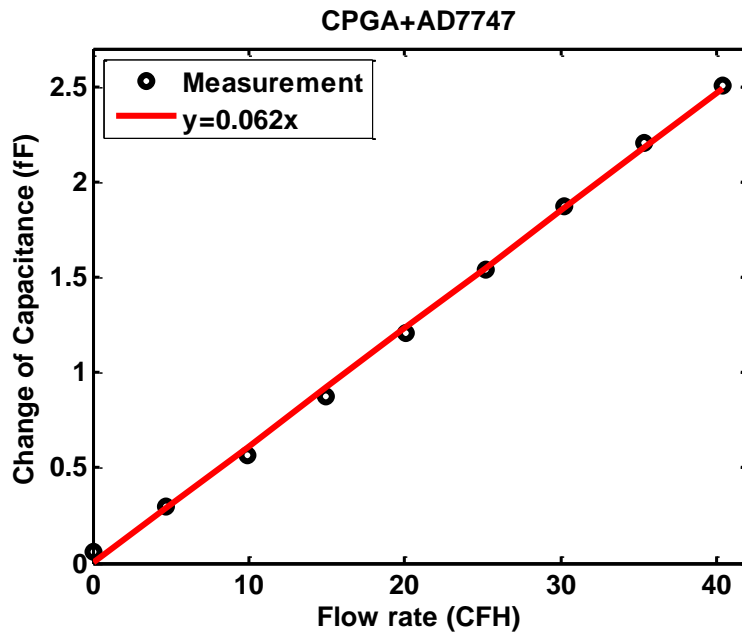
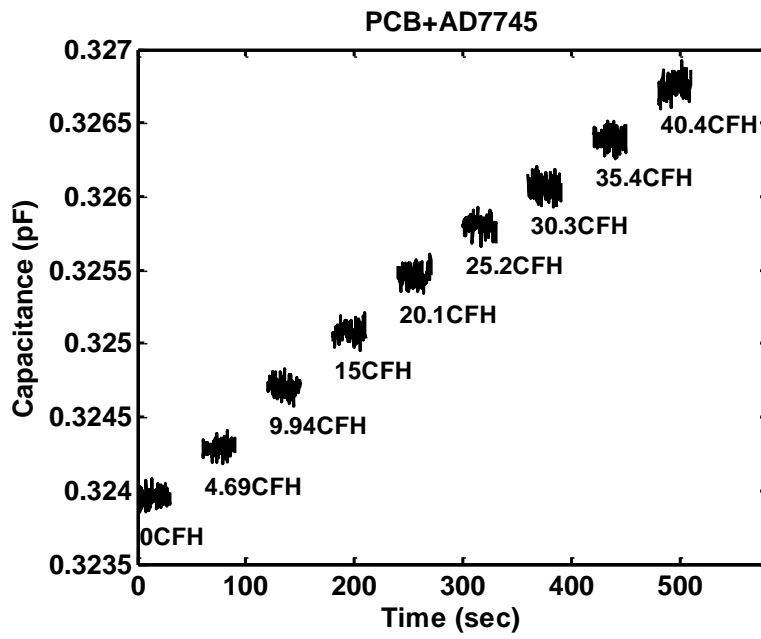
Figure 6.10. Flow rate measured in the digital flow controller response from 0 CFH to 40 CFH in steps of 5 CFH.

CPGA Package + AD7747 Electronics

In this setup, the MS3110 electronics is replaced by the AD7747 electronics, and the CPGA package is the same one as before. However, two groups were dead within these 10 months gap between two measurements. During this period of time, the package was protected in the plastic Petri dish and laying in the drawer of the laboratory, without any obvious damage. So, the reason is not clear (maybe particles) and more investigation is needed. However, this can indicate an advantage of array design: the sensor is still functional, if excluding the two dead groups.

Eight groups are tested with AD7747 electronics. From the time domain capacitance data, the relationship between the change of capacitance and the flow rate as well as the repeatability in Figure 6.11, we are able to demonstrate the sensitivity, noise level, resolution, and drift constant. The comparison with MS3110 will be summarized in the end of this section.

- 1) Overshoot settles out in the first 30 *sec* at each rate.
- 2) Care is taken on the electrode connection to have a same response direction of capacitance and flow rate.
- 3) The standard deviation using AD7747 measurement is 22 *aF* at a sample rate of 2.9 samples/sec. According to Eq. (6.9), the noise density is 18 *aF/rHz* at low frequencies.
- 4) This average of differential capacitances is computed for the 30 seconds of data at each stabilized flow rate.
- 5) The sensitivity of 8 groups using AD7747 electronics is given by 62 *aF/CFH*. Thus, one group is approximate 8 *aF/CFH*. 43% difference with the capacitance sensitivity of 14 *aF/CFH* in the MS3110 suggests that the MS3110 transfer function is not very accurate.
- 6) The sensor is still responding linearly up to the maximum flow rate. Due to the improved noise density with the AD7747, the dynamic range of the capacitance measurement is better, 43 *dB* at 1 Hz band.
- 7) The average drift is observed as low as 7 *aF/min*.



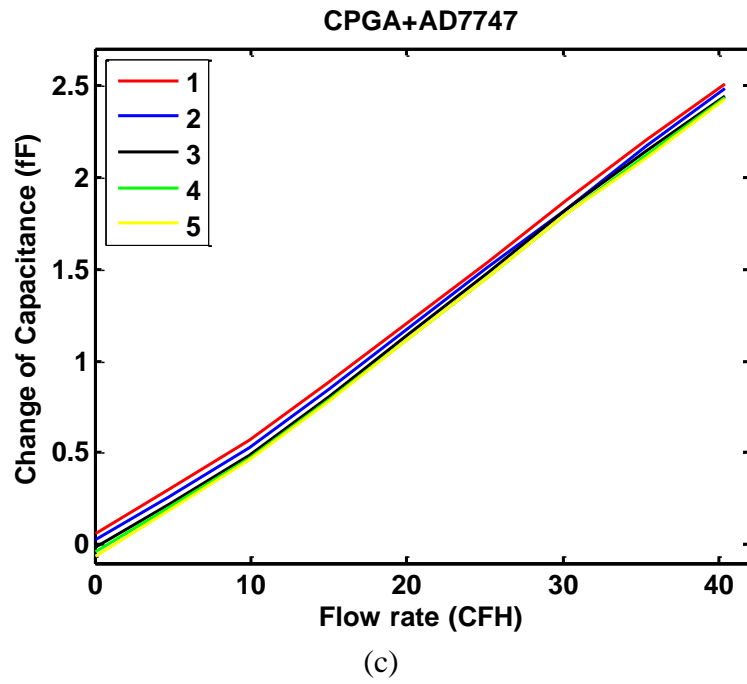
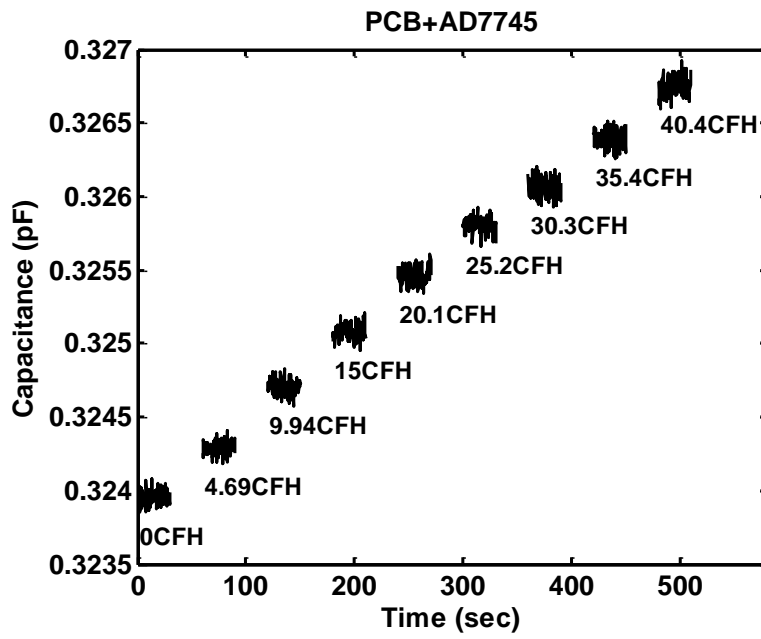


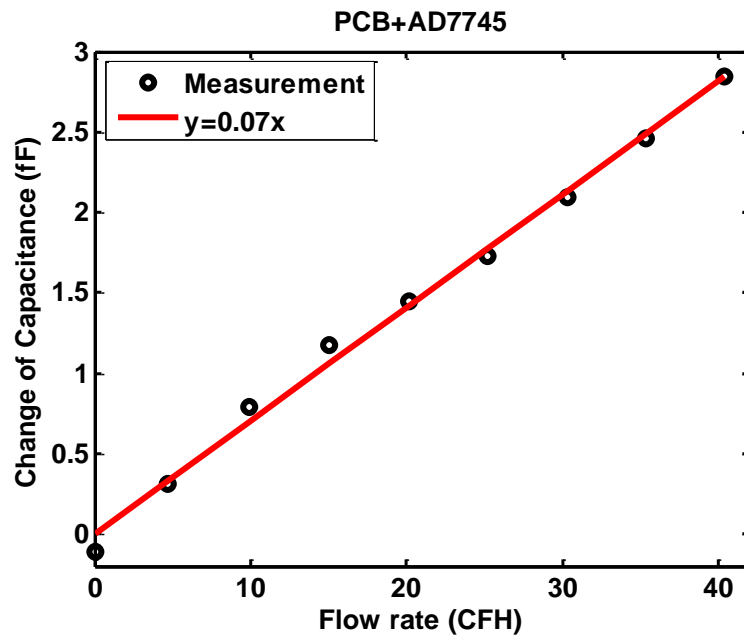
Figure 6.11. Measurement of 8 groups of floating element sensor arrays on a CPGA with AD7747 electronics in the 0.30 mm high laminar flowcell: (a) time domain capacitance data at each flow rate, (b) change of capacitance averaged at each flow rate in one cycle with linear fitting, and (c) repeatability in five cycles.

PCB Package + AD7745 Electronics

The probe sensor assembled the MEMS PCB (8 groups are packaged) on one side with the AD7745 electronics on the other side is also flush mounted in the 0.3 mm high flowcell and calibrated at the same flow conditions: 30 sec settling, 30 sec measurement, and 5 cycles. The characterization results are shown in Figure 6.12. Compared with 8 groups on CPGA associated with AD7747, AD7745 electronics demonstrates similar sensor sensitivity and drifting coefficient after a few hours, 70 aF/CFH up to 40 CFH, and 10 aF/min. However, the probe sensor performs with relative high noise, low resolution and low dynamic range. A triple standard deviation is resulting in a triple noise density at the same sampling rate. The higher noise suggests the larger loading effects on the electronics due to the PCB/tube packaging process is more complicated than the CPGA packaging on a target of the package size reduction. As the first generation, it is acceptable and the improvement of PCB packaging and the connection with electronics will be the future work. Thereby the dynamic range is 35 dB at an Hz band.



(a)



(b)

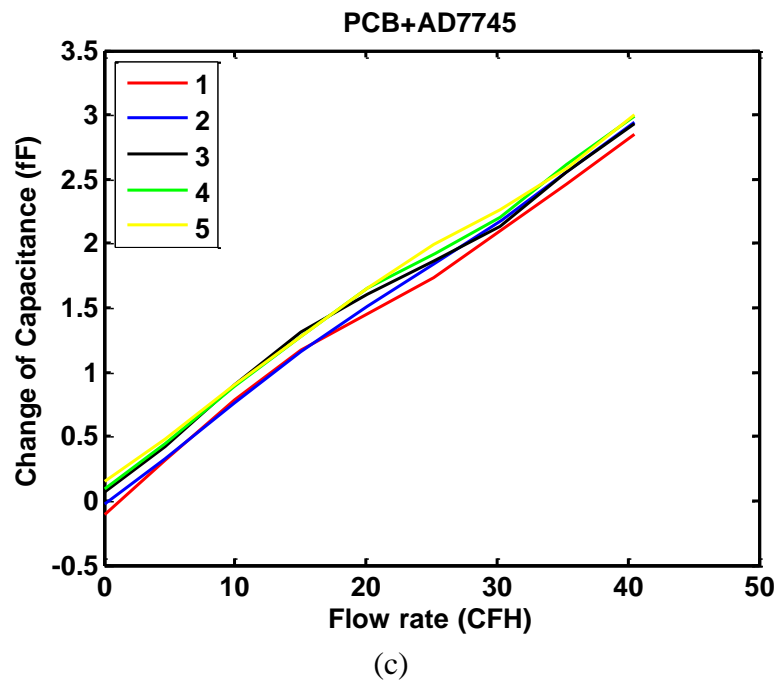


Figure 6.12. Measurement of the probe sensor (8 active groups) with AD7745 electronics in the 0.30 mm high laminar flowcell: (a) time domain capacitance data at each flow rate, (b) change of capacitance averaged at each flow rate in one cycle with linear fitting, and (c) repeatability in five cycles.

Summary

So far, the primary measurement of three floating element shear stress sensor approaches, with respect to flow rate and without explicit comparison to the wall shear stress and pressure gradient, has been accomplished. As Table 6.1 indicated, the CPGA packaging along with AD7747 electronics is the best option, with lower noise and higher resolution. Hence, this setup is used in the next section to determine the sensitivity of shear stress and pressure gradient.

Table 6.1. Characterization comparison of various packaging and electronics schemes at the labminar flowcell test.

	CPGA+MS3110	CPGA+AD7747	PCB+AD7745
Number of group	10	8	8
Sensitivity	$63 \mu V/CFH$	$62 aF/CFH$	$70 aF/CFH$
Standard Deviation	$89 \mu V$	$22 aF$	$63 aF$
Sampling Rate	$2.3 Hz$	$2.9 Hz$	$2.9 Hz$
Noise Density	$83 \mu V/rtHz$	$18 aF/rtHz$	$52 aF/rtHz$
Drift Coefficient	$16 \mu V/min$	$7 aF/min$	$10 aF/min$
Linearity	$> 40 CFH$	$> 40 CFH$	$> 40 CFH$
Dynamic Range (in 1 Hz band)	$> 30 dB$	$> 43 dB$	$> 35 dB$

6.2.4 Shear Stress Measurement

In order to address an important concern regarding the sensitivity of floating element sensors to pressure gradients, as described in chapter 3, the sensor has been tested in three laminar duct flow configurations, allowing separate experimental determination of the sensitivity to shear stress and pressure gradient.

Experimental Result

The sensor chip is packaged in CPGA, detected using AD7747 electronics, and tested in the laminar flow cell at 0.3, 0.5 and 0.53 *mm* duct heights. The pressure gradient measurements at all flowcells were already presented in Figure 6.5. The reader is reminded that 8 of the 16 groups on the chip are connected in parallel, so the output is the total capacitance change from 128 elements.

Followed by the 0.3 *mm* flowcell test described previously, the flowcell is replaced by the other two, and the identical measurements are conducted and recorded. Figure 6.13 shows the average change in capacitance as a function of the flow rate for the three different channel heights.

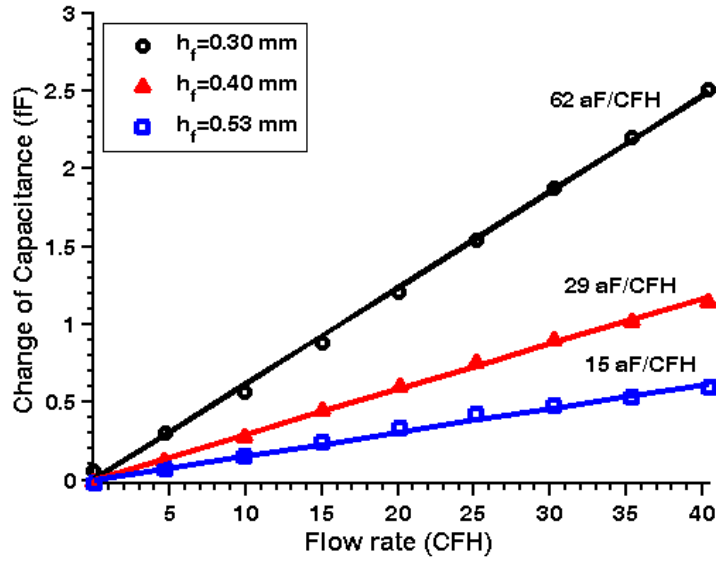


Figure 6.13. Measured change in capacitance vs. flow rate for all three channel heights. Best-fit lines are also shown.

Using the sensitivity model given in Eq. (3.24) and (3.25), it is postulated that the change in capacitance can be related to the shear stress and pressure gradient by

$$\Delta C = S_2 \tau_{yx} + S_3 \frac{\partial P}{\partial x} \quad (6.11)$$

For each flow condition the pressure gradient and the shear stress are known, either from the flow rate according to Eq. (6.6) and (6.7), or from direct measurement of pressure gradient. There are 24 non-zero flow conditions to evaluate and two constants to fit. This becomes a least squares problem; essentially we are fitting a plane to the data in shear stress-pressure gradient space. A linear least squares fit was performed to the 24 data points to determine the two sensitivities. It is again emphasized that these sensitivities are for 8 groups of elements (128 individual elements) acting in

parallel.

$$\begin{aligned} S_2 &= 77.0 \text{ aF} / \text{Pa} \\ S_3 &= -15.8 \text{ aF} / (\text{Pa} / \text{mm}) \end{aligned} \quad (6.12)$$

The norm of the residual is 56.6 aF , corresponding to 0.74 Pa of error. If, on the other hand, the pressure gradient sensitivity were neglected; that is, if we force $S_3=0$, then the best fit is $S_2=173 \text{ aF/Pa}$. For this case, the norm of the residual is 434 aF , corresponding to 2.5 Pa of error. A comparison of the measured vs. actual wall shear stress is given in Figure 6.14 for the two cases. Correcting for pressure gradient sensitivity improves the accuracy of the measurement.

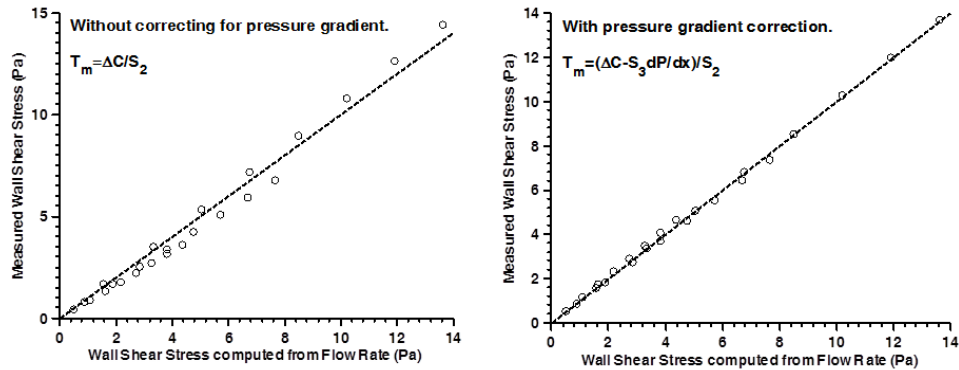


Figure 6.14. Comparison of shear stress measured by the MEMS sensor (y-axis) to shear stress computed from the volume flow rate (x-axis). All 24 non-zero flow conditions are plotted as open circles. The dashed line is the unit line, indicative of an accurate measurement. The plot on the left assumes no pressure gradient sensitivity. The plot on the right corrects for the pressure gradient using the measured sensitivity as in Eq. (6.11) and (6.12).

Discussion

It is quite significant that correcting for pressure gradient sensitivity improves accuracy for these 3 flow cases, but the result has even greater

importance than simply improving accuracy in laminar flow. If the sensor were to be used in a different flow regime, the substantial sensitivity to pressure gradient could cause inaccurate measurements of shear if neglected. For example, if the actual wall shear were 10 Pa in a turbulent flow with zero pressure gradient, but pressure gradient effects were neglected in the calibration, then the user would think the sensor shear sensitivity was 173 aF/Pa, rather than the actual sensitivity of 77 aF/Pa. Thus, the sensor would suggest that the wall shear was $(77/173) (10 \text{ Pa}) = 4.4 \text{ Pa}$, a large error.

The experiments conducted in this work are not sufficient to demonstrate that the model of Eq. (6.11) and (6.12) is fully sufficient for describing sensitivity to all kinds of flow, such as TBLs, turbulent duct flows, separated flows, or a variety of other flows of interest. However, these experiments do demonstrate that pressure gradient effects are a necessary consideration in calibrating floating element sensors and should not be neglected.

With the measured sensitivities in hand, it is now possible to go back to the electromechanical model developed in Eq. (3.24) and (3.25) to see what the effective surface area and effective volume of the element are. Keep in mind that there are 128 elements acting in parallel in the experiment, so the sensitivity will be 128 times that of Eq. (3.24) and (3.25). Using the measured dimensions from Table 4.1, and taking the modulus of electroplated Nickel to be $E=205 \text{ GPa}$ [44], the effective surface area of the element is

$$\Delta x \Delta z = \frac{Edw^3}{128 \cdot N \epsilon L^3} S_2 = 0.086 \text{ mm}^2 \quad (6.13)$$

which is very close to the actual physical surface area of the shuttle, 0.085 mm^2 . The effective volume of the element is

$$\Delta x \Delta y \Delta z = \frac{-Edw^3}{128 \cdot N \epsilon L^3} S_3 = 1.8 \cdot 10^{-2} \text{ mm}^3 \quad (6.14)$$

which is more than an order of magnitude larger than the physical volume of the shuttle, $7.5 \cdot 10^{-4} \text{ mm}^3$. On this basis it is concluded that the element shows the sensitivity to surface shear that would be predicted based solely on the physical surface area, but considerably more sensitivity to pressure gradient than would be predicted based on the physical volume. It seems likely that the increase in pressure gradient sensitivity is due to two factors: (1) the complexities of the flow around the microscale geometries of the beams, combs, and bumps leading to changes in pressure close to the element features (2) the topology of the package contributing to changes in the flow pattern at the scale of the entire chip, resulting in changes to the fluidic forces.

It is important to determine the mechanisms that lead to the increased pressure gradient sensitivity. Initial two and three dimensional computational fluid dynamics results support the idea that flow around the edges of the element, the combs and the beams result in substantial increases in the pressure loading on the structure. It may be that decreasing the size of the gaps around structural elements such as the beam tethers can reduce pressure gradient sensitivity. However, additional analysis and experimental work is required to explore the mechanisms.

6.3 Turbulent Boundary Layer Test

This section will describe the characterization of the floating element shear stress sensor array under a turbulent boundary layer (TBL) at an indraft windtunnel at the NASA Ames Research Center (NARC). The sensors were fabricated and packaged at Tufts University, then shipped to California for experiments.

6.3.1 Experimental Setup

The wind tunnel to calibrate the shear stress sensor is in the fluid mechanics laboratory at NARC. The tunnel is an open circuit indraft tunnel with a $38\text{ cm} \times 38\text{ cm}$ square cross-section with a maximum flow speed of 62 m/s . A settling chamber with honeycomb and 8 mesh screens, a rounded bell mouth inlet, and a smooth 8.5 m long square to round diffuser contribute to a low turbulent intensity at the inlet to the test section. Suction to produce flow is provided by a 75 hp centrifugal blower. The MEMS shear sensor probe is flushed mounted into the floor plate at a location 65 cm downstream from the exit of the contraction section. The test setup is shown in Figure 6.15.

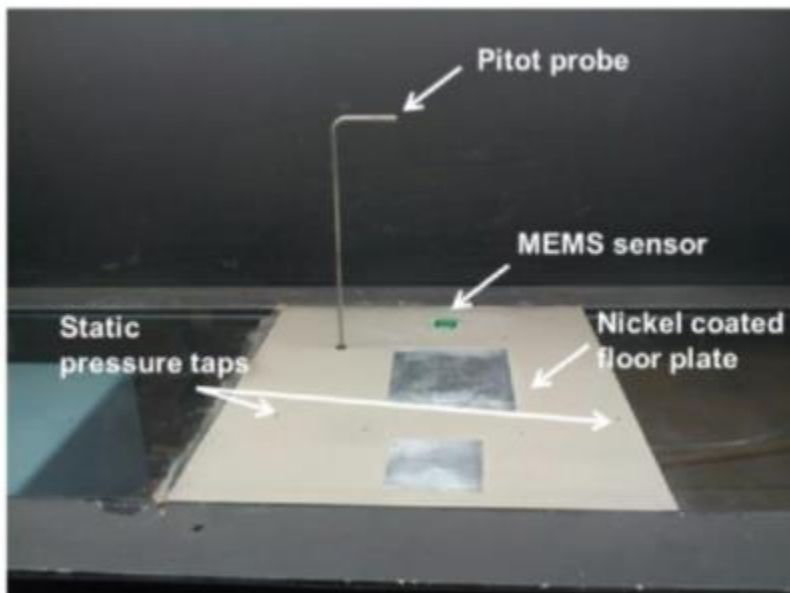
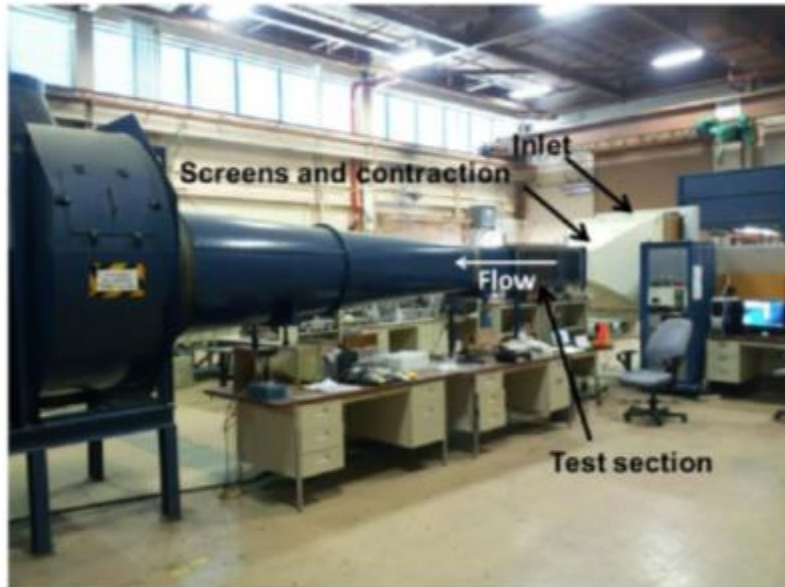


Figure 6.15. (Top) Photographs of the flow facility and the test section. (Bottom) The MEMS sensor is flush mounted in a nickel painted acrylic plate in the floor of the test section, 65 cm from the end of the contraction, a pitot probe is used to measure the free stream velocity and boundary layer profile.

The floor plate used in the experiment is cast acrylic. In initial testing, the sensor exhibited substantial drift and hysteresis. It was determined that this was due to tribological charging of the insulating acrylic plate. The effect had not been observed when testing in a conducting aluminum plate of

the laminar flowcell. The sensitive capacitance measurement used in this device has the potential to be very sensitive to charging in the local environment. To combat this problem, the acrylic plate was painted with a conductive nickel-based spray paint, and grounded. This surface treatment removed the drift and hysteresis.

6.3.2 Shear Stress Measurement

The tunnel is run at four discrete flow speeds by controlling blower RPM. During testing, a pitot/static probe is used to measure dynamic pressure near the flow centerline to estimate free stream velocity. The dynamic pressure and shear stress are recorded simultaneously during the tests at 1 sample per second. Table 6.2 gives the four conditions.

Table 6.2. Flow conditions for tunnel testing: The measured flow speed is shown. The predicted skin friction and boundary layer thickness are computed using $1/7^{\text{th}}$ power law correlations.

Flow Speed (m/s)	Ma	$Re_x (\times 10^6)$	C_f	δ (mm)	τ_w (Pa)
17.4	0.05	0.74	0.0039	15	0.56
34.4	0.10	1.5	0.0036	14	2.5
52.0	0.15	2.2	0.0034	13	5.3
61.7 (max)	0.18	2.6	0.0033	13	7.6

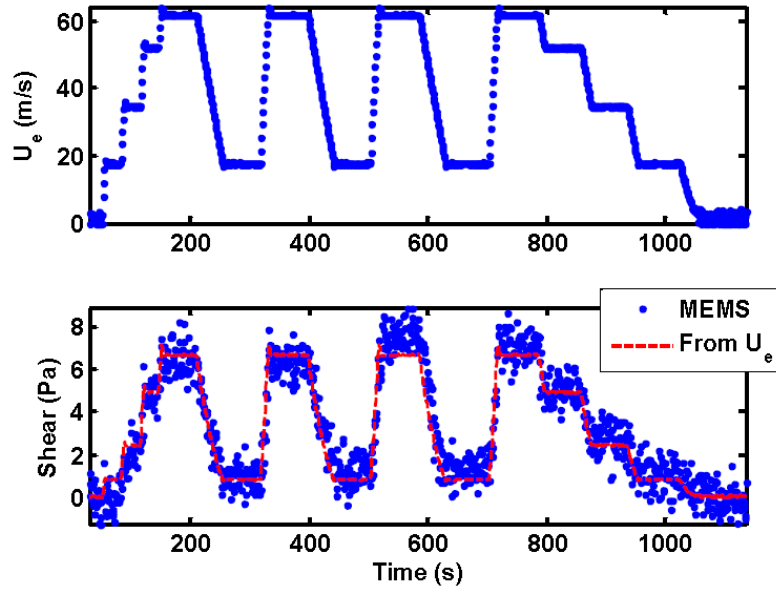
The flow speed is the measured speed from the pitot/static probe, assuming an air density of $\rho=1.2 \text{ kg/m}^3$. Mach number and Reynolds number based on plate length are computed from the flow speed using a speed of sound $c=343 \text{ m/s}$ and kinematic viscosity for air of $\nu=1.5 \cdot 10^{-5} \text{ m}^2/\text{s}$. The skin

friction coefficient and boundary layer thickness are estimated from a 1/7th power law [37]

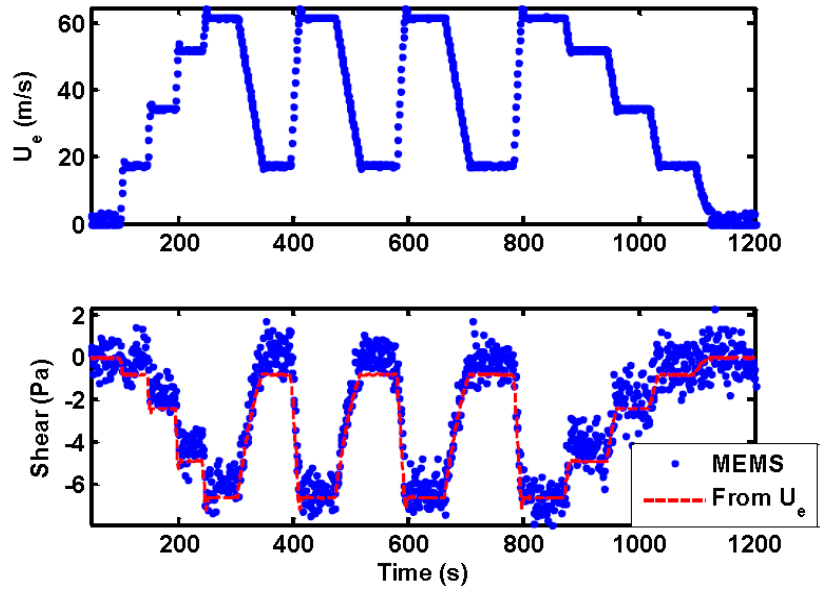
$$C_f = 0.027 \text{Re}_x^{-1/7} \quad (6.15)$$

$$\delta = 0.16x \text{Re}_x^{-1/7} \quad (6.16)$$

The tunnel is run between these conditions, stepping up, then holding at the maximum speed, stepping down to minimum speed, back up to maximum speed, and so on for 4 cycles before stepping down through the four speeds back to zero. Three tests are run: one with the sensor aligned with the flow, one with the sensor aligned opposite the flow, and one with the sensor aligned in the cross-flow direction. The results are shown in Figure 6.16. The sensor accurately captures the changing shear stress in real time. When rotated opposite to the flow, the sign flips on the output, as expected. When oriented in the cross-flow direction, no change is observed in the sensor output. This is a strong indication that the sensor is measuring shear, and not temperature, humidity, or other scalar quantities. In addition, the measured streamwise pressure gradient in the duct is low, less than 0.12 Pa/mm, so it seems unlikely that the sensor is responding to pressure gradient rather than shear stress.



(a)



(b)

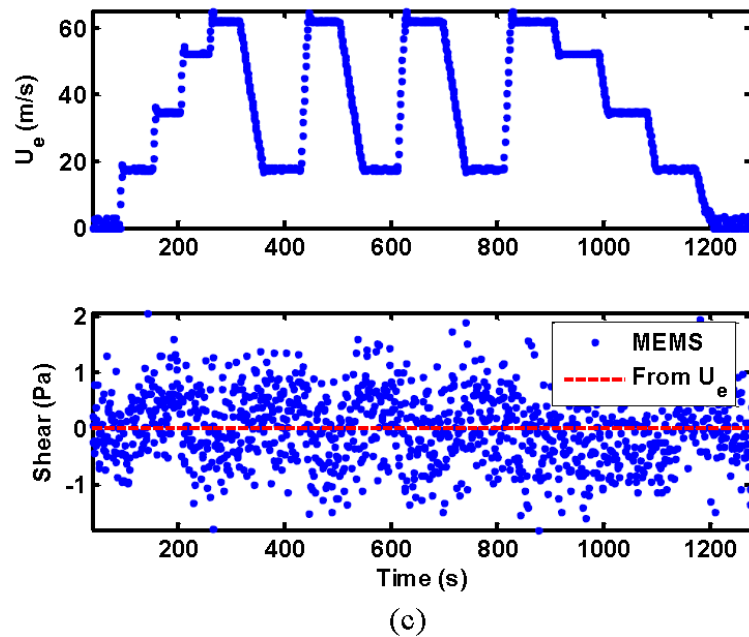


Figure 6.16. The top panels in each plot show the free stream velocity measured by the pitot/static probe. The bottom panels show a comparison between the measured shear stress from the MEMS sensor, and the shear stress computed from the velocity using the correlation (a) MEMS sensor oriented with the flow. (b) MEMS sensor oriented opposite to the flow direction. (c) MEMS sensor oriented in the cross-flow direction.

The best fit between the MEMS output and the shear computed from velocity is achieved with a sensitivity of 90 aF/Pa . Laminar flow calibrations reported previously gave similar results of 77 aF/Pa . Referring back to Eq. (3.24) and the measured dimensions of the element in Table 4.1, the approximate expected sensitivity of 128 active elements can be computed based on the physical surface area of the shuttle, 76 aF/Pa . This prediction and laminar flow test are both close to the best fit result from the tunnel tests. The slight difference may come from two sources: (i) experimental error in surface shear, dominated by the accuracy of the boundary layer profile data and the model fit to the boundary layer profile used to extract the wall shear from flow velocity, (ii) neglecting the effects of the surface bumps and sensor topology on the fluid interaction forces. The pressure gradient sensitivity is not a concern as pressure gradient is very low.

In a no flow condition, mounted in the tunnel in an identical setup to that used for flow testing, the measured standard deviation of measured shear stress is 72 aF with a 1 Hz sample rate. The noise density of the capacitance measurement is therefore 99 aF/rHz according to Eq.(6.9), which is equivalent to 1.1 Pa/rHz . An identical calculation performed on the data for the cross-flow case shown in Figure 6.16_(c) results in 0.9 Pa/rHz . Thus, the fluctuations in shear shown in Figure 6.16_(c) are electronic noise, not real fluctuating shear stress components.

It is also noted that the noise density of probe sensor in the windtunnel

test is double of Table 6.1 measured in the laminar flowcell and much higher than the manufacturing report for the AD7745 chip. More work needs to be done to determine sources of additional noise, such as EMI, power supply fluctuations, or ground noise.

A slow drift in the capacitance of the MEMS sensor, between 0.2-0.5 *aF/sec*, are experienced in the three runs described here. This is equivalent to a drift of approximately 0.1-0.3 *Pa/min*. The output shown in Figure 6.16 is detrended by subtracting out a linear fit between the data at zero flow condition at the beginning and end of the run. This effectively removes the majority of the drift.

The temperature in the tunnel during the run is between 20°C and 22°C as measured by a thermocouple in the flow. The temperature of the MEMS sensor electronics is more stable, varying between 21°C and 21.5°C, as measured by the internal temperature sensor in the AD7745. No correlation is seen between temperature and sensor output in tunnel testing. However, more recent results do show both temperature and humidity sensitivity for the device, issues that will be explored in future work.

Chapter 7

Conclusion

In this chapter, a summary of the work presented in this dissertation as well as the key results contributed will be given. The future work proposals relating to chapter 3 to 6: the design, fabrication, packaging, and characterization of MEMS floating element shear stress sensor arrays will conclude the dissertation.

7.1 Hardware

A MEMS floating element shear stress sensor with bumps array has been designed in a 1×1 cm chip. The array consists of 256 individual floating elements (16 groups), and each element supports 35 bumps on the top surface. A unique array-based floating element shear stress sensor with surface bumps is developed with the ultimate goal of measuring local shear stress at small spatial scales. The chip includes 16 individually addressable groups in a 4×4 array with a spatial resolution of 2 mm. This is the first demonstration in the literature of an array-on-a-chip shear stress sensor, and also the first demonstration of surface bumps to increase interaction with the flow.

The sensor was fabricated using four layers of surface micromachining including copper & nickel electroplating. The fabrication is conducted on a glass substrate. The process consists of a $0.3 \mu\text{m}$ thick electrical interconnect layer, a $5.2 \mu\text{m}$ air gap separation using a copper sacrificial layer and wet etch release step, a $8.8 \mu\text{m}$ thick electroplated nickel structural layer, and $11.7 \mu\text{m}$ high electroplated nickel bumps. This process is not unique in the literature, it is similar to other “LIGA-like” processes that have been demonstrated by various groups, but it is the first application that we are aware of this low cost, low stray capacitance nickel-on-glass process to floating element shear sensor fabrication.

The MEMS chip was then wire bonded in a commercial ceramic package (CGPA) and epoxy encapsulated. Both analog and digital electronics were

designed and demonstrated using commercial MS3110 capacitance to analog, or AD7747 capacitance to digital readout chips. The differential measurement using the AD7747 demonstrates a detectable wall shear stress range up to 13 Pa with less than 1% nonlinearity in the laminar flowcell. The maximum demonstrated linear range is limited by the testing setup, not the sensor; to date we have not been able to produce higher shear than 13 Pa in a laminar flow setup. The calibration of a chip with 8 active groups (128 elements) in parallel shows a sensitivity of 77 aF/Pa at a noise density of 0.23 $Pa/rtHz$ at low frequencies (below 1.5 Hz), thereby the dynamic range is greater than 43 $dB/rtHz$. A DC voltage drift was observed during operation. The drifting coefficient saturates at approximately 0.1 Pa/min . This is not the highest resolution achieved by a MEMS shear sensor in the literature, but it is one of the highest maximum shear stress levels calibrated.

7.2 Operation

A major finding of this dissertation is that for surface shear sensors of this type, it is critical to measure and include a correction for pressure gradient sensitivity in order to achieve accurate measurements of surface shear stress. Experiments conducted in three different height flow ducts allowed independent determination of the sensitivity to surface shear (77.0 aF/Pa) and pressure gradient (-15.8 $aF/(Pa/mm)$). As far as we are aware, this work gives the first published experiment specifically distinguishing these two

sensitivities for a MEMS floating element sensor.

In a second generation device, a more highly integrated packaging method was developed to replace the large CPGA package. For this integrated system, a 25 mm diameter and 13 mm long cylindrical tube housed both the MEMS floating element array chip and AD7745 readout electronics. As far as we are aware, this package is the most integrated MEMS shear sensor system in existence. The resolution for the AD7745 chip in the integrated package was somewhat lower than the AD7747 chip used with the CPGA package. This was unexpected, as the AD7745 chip is expected to have better resolution. The cause is uncertain but is expected to be related to other aspects of the integrated packaging system, such as the PCB package, shielding scheme, or conductive ink interconnects.

The probe was characterized under a turbulent boundary layer in a 38 × 38 cm test-section inflow wind tunnel. Real time shear was measured as tunnel free stream velocity varied from no flow up to 62 m/s. Shear stresses up to 6.5 Pa were measured, consistent with expectations based on the measured boundary layer profile and zero pressure gradient flat plate boundary layer theory. Sensor sensitivity in this setup was 90 aF/Pa, which is very similar to theoretical predictions and laminar flow test result. Resolution was 1 Pa/rtHz, similar to the result in the laminar flowcell test. Orientation dependence of the sensor output was verified, demonstrating the ability to measure direction as well as magnitude of the shear stress. Some drift is also

observed, although this is effectively removed using a calibration procedure.

An important practical issue related to deployment in a tunnel was discovered during testing. Due to the small capacitance changes being measured and the high sensitivity of the readout electronics, the sensor is strongly influenced by the presence of accumulated charge in close proximity to the measurement location. It was noted that the sensor experienced substantial drift and hysteresis when operating in an insulating floor plate (cast acrylic). By painting the floor plate with conducting nickel paint, and carefully grounding the paint and the sensor housing, drift and hysteresis were substantially reduced.

7.3 Future Work

There are several improvements suggested by this work which should be pursued in future work. Demonstration of next generation sensor with higher sensitivity and accuracy, less noise, and a larger dynamic range is the first priority for future work. The linearity up to 13 Pa shear stresses is limited by the current flow testing setup, not the sense itself. Therefore, the sensor test at 40 Pa (see Table 2.2) or even higher shear stress is a second priority task in the future. The success of this will contribute that the floating element sensor has an ability to survive and operate at the real condition of aircrafts. Details of these recommendations are described below.

7.3.1 Design

7.3.1.1 Sensitivity Improvement

The comb finger was used as the structure to convert deflection to an electrostatic measurement. Figure 7.1 shows a new floating element design with a long straight horizontal gap replacing the series of combs. This architecture can give a higher sensitivity while also reducing fabrication difficulties. However, it may introduce higher nonlinearities.

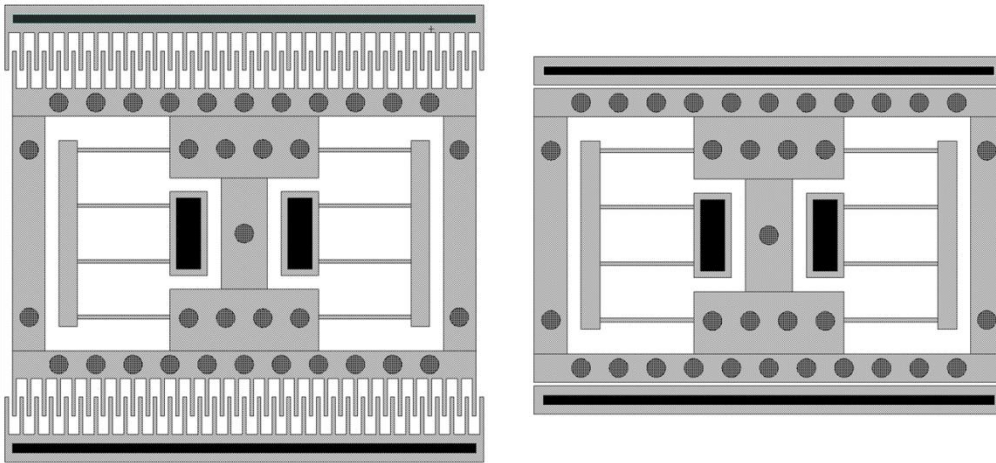


Figure 7.1. (Left) Current floating element. (Right) New floating element design: a straight capacitor substitutes the comb finger.

The static capacitance of a new element is given by

$$c = 2 \frac{\epsilon t b}{d} \quad (7.1)$$

where d is the gap, t is the out of plane thickness, and b is the horizontal length.

If the center shuttle is driven at x displacement, the sensing movement of parallel plates will be a gap change (change in d) instead of an overlap change as with the combs. The change of capacitance is a function of the change of

($d-x$)

$$\frac{\partial c}{\partial x} = -2 \frac{\epsilon t b}{(d-x)^2} \quad (7.2)$$

The motion of current floating element is expect to move only a few nanometers at 13 *Pa* shear stress and d is maintained at 4 μm , the displacement should be much smaller than the inertial gap, $x \ll d$, for almost flow applications. Then, Eq. (7.2) can be simplified into

$$\frac{\partial c}{\partial x} \approx \frac{-2\epsilon t b}{d^2} \quad (7.3)$$

Compared with the sensitivity of comb finger in Eq. (3.19) and using the current geometry: 64 fingers in an element, 4 μm gap, $L=500 \mu m$, the sensitivity is doubled theoretically. Two additional benefits about the comb finger replacement are that the fabrication in the floating element layer will be easier, especially lithograph, and the overall size reduction. However, some drawbacks are the output is now more nonlinear, and, as the stiffness in the collapse direction is now reduced, there may be more problems with stiction failure during fabrication.

Besides the comb finger replacement, other modifications of the element geometry are also able to improve the sensitivity, for instance, making the gap (d) of parallel plates smaller or the change of other parameters in Eq. (3.20). Increasing the size of the top surface of the shuttle and removing surface roughness (the bumps) will contribute to increase the shear stress sensitivity and reduce the pressure gradient sensitivity. However, increasing surface

area will introduce more problems with stiction during fabrication [45]. The air gap below the shuttle can be increase to address the issue.

Adding additional metal (Cr/Au) planes on the glass below the comb finger can act as additional active capacitance. As the center shuttle moves over, the capacitance between new metal planes and comb finger changes. The disadvantage is that it will increase the parasitic capacitance.

7.3.1.2 Yield Improvement

The best achieved yield for a single chip is 11 out of 16 groups active so far, and most cases are 50%. An effort to improve the yield should be undertaken in the future. Although the exact reason for failed groups is not clear, a possible solution is to have the center shuttles on the same row combined physically, as shown on the right hand side of Figure 7.2. It might be helpful to avoid the stiction down to the substrate below, which is a possible cause of failure. This change is also able to remove some gold wires underneath, particularly any asymmetric wiring, which may also be a cause of failure. Switching to a single long gap instead of multiple fingers may also improve yield, by reducing the number of thin gaps in the design. Finally, reducing the size of the chip from 1 cm^2 to $5\text{ mm} \times 5\text{ mm}$ or smaller, with a corresponding reduction in the number of elements, will improve the odds of full yield.

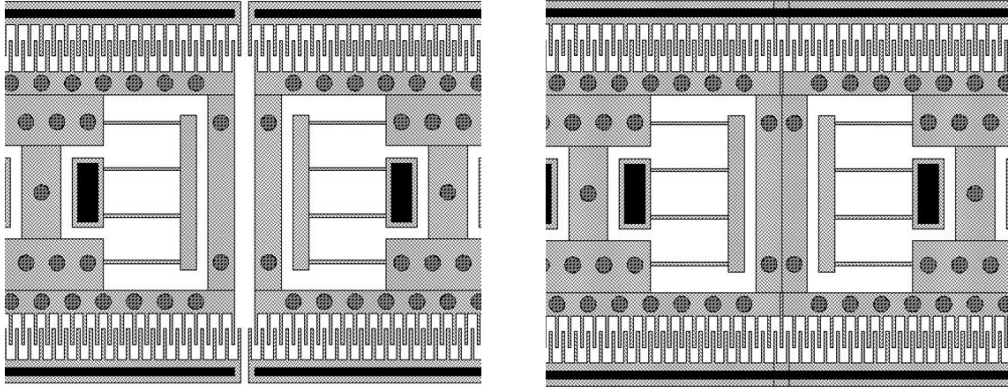


Figure 7.2. (Left) 25 μm gap between neighbor elements in current group layout. (Right) New group design with all elements connected laterally.

7.3.1.3 Pitch size reduction

In the mask layout design (see Appendix A.4), shrinking the pitch size of groups will release more margin on the edge of chip. This is useful to ease the difficulty of alignment between the PCB and the MEMS chip in the packaging step, also reducing fluid influence across the chip due to those gaps. The current design is able to produce 70 μm spare spaces on top and bottom sides. Changing in comb finger (mentioned above) will enlarge the margin significantly.

7.3.1.4 Array Design

All elements on a sensor chip are aligned unidirectional to the flow direction in the current design. If the 50% elements are designed and oriented perpendicularly to others, the sensor can be considered as bidirectional. The benefit is bidirectional sensor is capable of measuring the fluctuated velocity components (u_x, u_y) in the averaged flow direction and cross-flow direction under a turbulent boundary layer.

7.3.2 Fabrication

7.3.2.1 Sacrificial Layer Improvement

For the device described here, two lithography steps are required to produce one sacrificial layer. Figure 7.3 shows a proposal to achieve a $5\ \mu\text{m}$ sacrificial layer within one lithographic step. The key is that if more than $5\ \mu\text{m}$ LOR resist followed by AZ9245 is patterned and undercut, this can separate the seed layer from the anchor to sacrificial areas. The photoresist pattern is used in the copper plating step without liftoff and second lithography. Liftoff is applied afterwards.

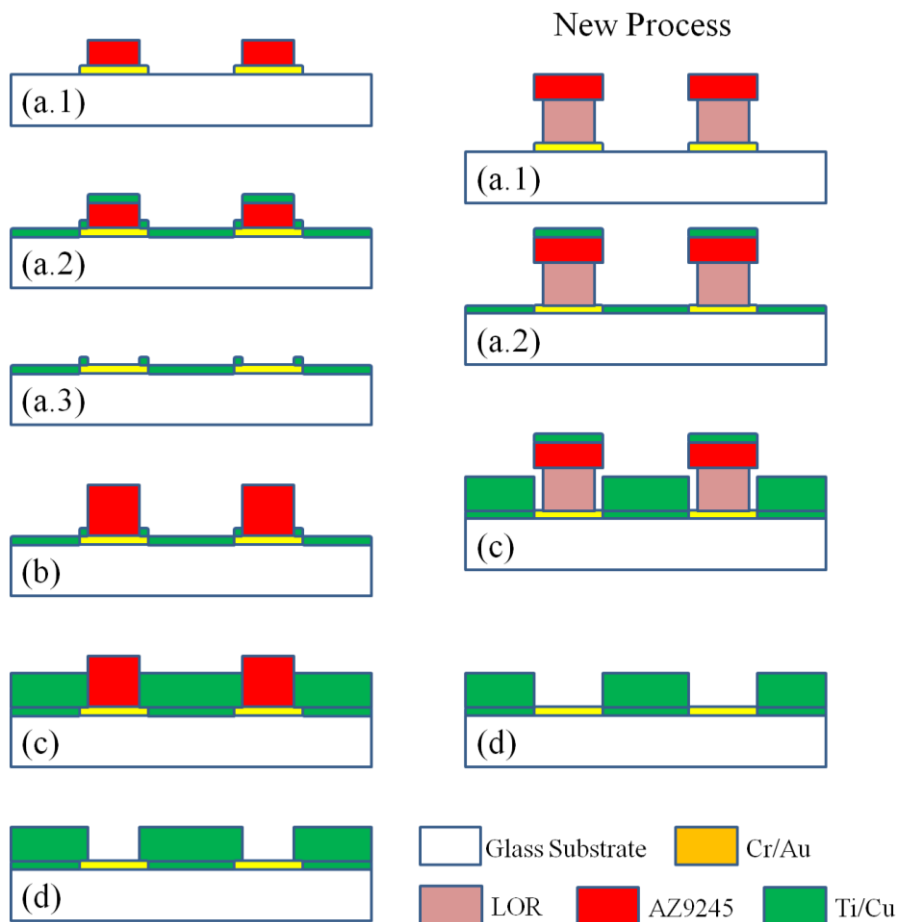


Figure 7.3. Fabrication improvement at the sacrificial layer: reduce one lithography step.

7.3.2.2 Minor Recommendations

First, as was mentioned in chapter 4, the anchor area under the comb fingers is 10 μm wide, which is slightly narrow for LOR resist application. 15-20 μm width may be better for the next mask design. Second, during the development of photoresist in a beaker, such as AZ series photoresist in AZ400K developer, a non-uniform issue is always observed. This might be solved if switching into a large petri dish where the wafer can lay down horizontally.

7.3.3 Packaging

7.3.3.1 AD7746 Instead of AD7745

Once a higher yield is achieved, a next step can be to implement AD7746 instead of AD7745 readout. The AD7746 has two input channels which allow two things. First, two output capacitance of either top/bottom or left/right groups are separated to give two independent measurements on chip. Second, if a reference set of floating elements is used on one channel and physically anchored down, so no deflection is possible, any change in capacitance in the reference channel is from environmental parameters, such as temperature, humidity, and local charge fluctuation. Due to the physically identical nature of the two sensor sets on chip, the anchored set should act as an excellent reference to reduce unwanted environmental sensitivity.

7.3.3.2 Grounding of Aluminum tube

The ground pin of the AD7745 electronics can be used to ground the

aluminum tube. An additional via on the edge and a wire connected the GND via to new via should be added to the current PCB in Figure 5.13. Once it is assembled in the aluminum tube, a small amount of conductive epoxy can be easily applied on the new via through the inner wall of the tube.

7.3.3.3 Ink Printing Improvement

The conductive ink setup has some potential to improve. First, the speed of the micro stage as well as the syringe moving speed is a major limit to achieve a fine ink line. Second, automated drawing between every pair of pads and pins can be implemented by setting the travelling distance, if the package surface is more uniform.

7.3.4 Characterization

In order to characterize the floating element sensor at higher shear stresses (above $13 Pa$), the height of the next flowcell (h_f) is reduced at $0.2 mm$. If the width is as same as before, $28 mm$, according to Eq. (6.4)-(6.8), (i) the Reynolds number is independent with h_f so the flow is maintained at the laminar region, (ii) the flow is still fully developed before the pressure taps because the entrance length is proportional to h_f , (iii) the pressure gradient as well as the shear stress at 0 to 40 CFH are predicted in Figure 7.4. Therefore, the new flowcell should be able to generate a maximum of $30 Pa$ shear stress of laminar flow and the centerline velocity up to Mach number of 0.25 ($84 m/s$). As the flow channel becomes smaller, the sensor packaging topology must also be reduced.

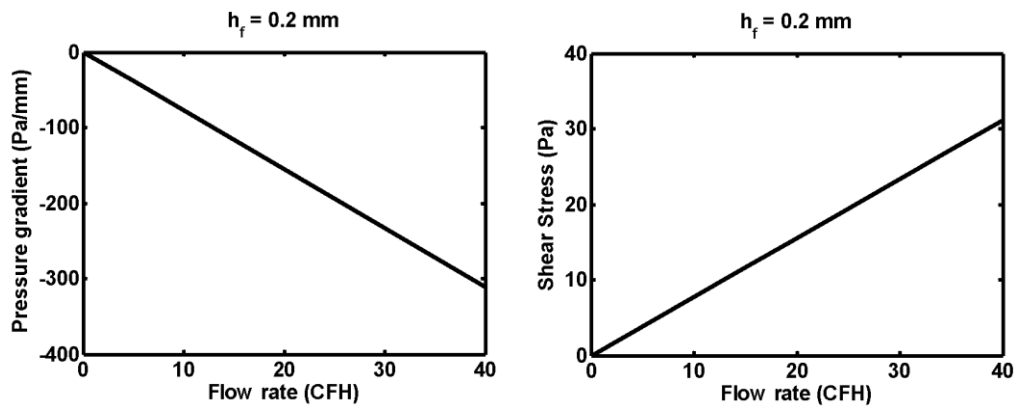


Figure 7.4. (Left) Prediction of pressure gradient and (right) shear stress as a function of flow rate at 0.2 mm duct height.

7.3.5 Feedback control

Closed loop feedback control to rebalance the sensor shuttle in the sensor of its operating range may also be a fruitful avenue for future work. In order to implement this, the sensor has to have the sensing and driving components separately. So, one idea is to split the comb fingers into two sections. The new floating element in Figure 7.5 has four channels: inner top, inner bottom, outer top, outer bottom. Then, the inner set or outer set are going to use to either sense the shear stress (flow) or drive the center shuttle by applied voltage.

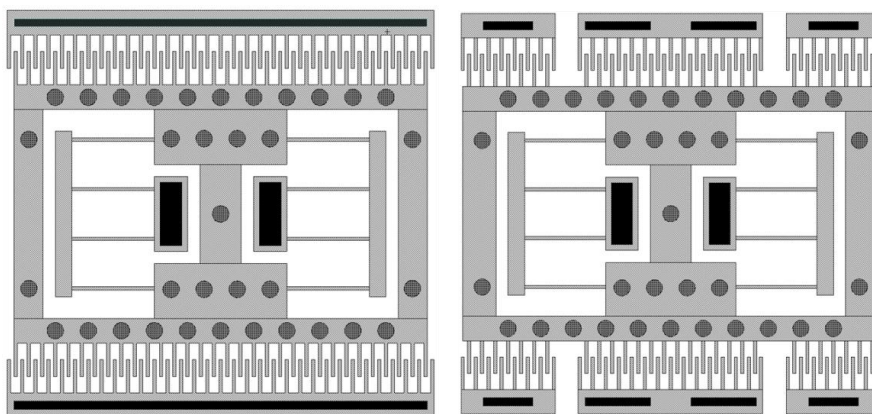


Figure 7.5. Separation of comb finger for the feedback control application.

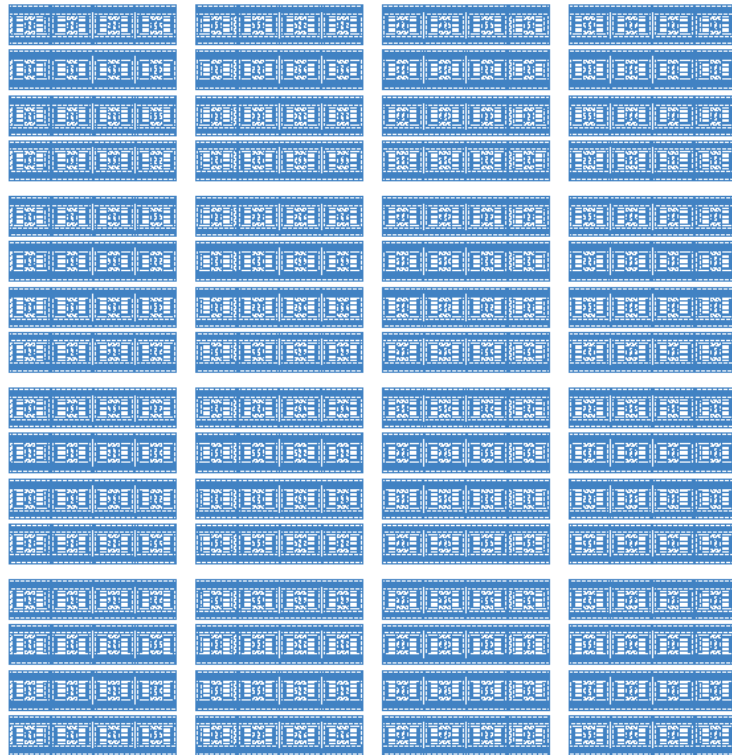
Appendix A

Mask Layout

A.1 Metal Layer Mask



A.4 Floating Element Layer Mask



A.5 Bump Layer Mask



Appendix B

Fabrication Runsheet

Process Name: Surface Micromachining

Mask: Tufts_SM3

Process Goal: Micromachine various surface micromachined devices with a copper sacrificial layer, nickel structural and hairpost layer, and Cr/Au interconnect.

Author: Zhengxin Zhao, Minchul Shin, Robert White

Revision Date: Apr 13, 2013

Refer to SOPs: “Standard Lithography”, “OAI Aligner”, “Laurell Spinner”, “NSC-3000 Sputter”, “March RIE”, “Copper Electroplating”, “Nickel Electroplating”, “LOR Liftoff”.

Starting Substrates: 100±2mm Soda Lime 550±50µm Thick DSP (60/40) W/Rounded Edges & Primary Flat Only.

Lab Temperature: Lab Relative Humidity:

<u>Step Name</u>	<u>Parameters</u>	<u>Measurements/Comments</u>	<u>Date Complete</u>
1. Examine mask	Microscope.		
2. O₂ Clean	200W, 120sec, 100% O ₂ (~300 mT) in March RIE		
3. Lithography	LOR20B: 500 rpm 4sec, 2000 rpm 45sec, 200C 5min softbake; AZ9245: 500 rpm 5 sec spread, 4500 rpm 60 sec spin, 115C 1 min 30 sec softbake, 20 sec exposure (hard contact), 2 min 20 sec develop in AZ400K:water 1:3, 2 x 2 DI water rinse, air gun dry	<u>Notes:</u> LOR20B: <u>2000 rpm = 2.0 µm</u> AZ9245: <u>4500 rpm = 3.0 µm</u>	
4. O₂ Descum	150W, 30 sec, 100% O ₂ (280 mT) plasma descum in March RIE	<u>Etch rate ~ 0.4 µm/min</u>	

5.Sputter Cr/Au	Pump down for > 1 hour (<5e-5 torr). Use 60 sec target clean. Sputter on 75 nm Cr (200 W), 225 nm Au (150 W) at 5 mT	Cr: 3 A/sec Au: 7.5 A/sec	
6. Liftoff	Heating Remover 1165 to 60C for > 5hr. (No need for swab and sonicator). Don't let metal particles settle out and dry in place!!! Rinse with IPA, 2 x DI water. Air gun dry.	Measure metal thickness and roughness	
7. Lithography	HMDS/SPR220-3 500 rpm 4 sec spread, 3000 rpm 30 sec spin, 115C 90secsoftbake, 8sec exposure (hard contact), 90 sec 115C PEB, 2 min 15 sec develop MFCD26, 2 x 2 DI water rinse, air gun dry	<u>Notes:</u> <u>3000rpm=2.1</u> <u>µm</u>	
8. O₂ Descum	150 W, 30 sec, 100% O ₂ (280 mT) plasma descum in March RIE		
9. Sputter Ti/Cu	Pump down for >1 hours. Sputter on 30 nm Ti (150 W), 300 nm Cu (200 W), at 5 mT	<u>Ti = 0.6 A/sec</u> <u>Cu = 4 A/sec</u>	
10.. Liftoff	Liftoff Ti/Cu in acetone, with agitation, swabbing, and sonication as needed. Be careful not to let metal particles settle out and dry in place!!! Rinse with acetone/IPA, 2 x DI water. Air gun dry.	Measure metal thickness and roughness	
11. Lithography	HMDS/AZ9245 500 rpm 5 sec spread, 1000 rpm 60 sec spin, 115C 2.5 min softbake, 35 sec exposure (hard contact), 5 min develop in AZ400K:water 1:3, 2 x DI water rinse, air gun dry	<u>Notes:</u> 1000 rpm = 8 µm thick	
12.. O₂ Descum	150 W, 30 sec, 100% O ₂ (280 mT) plasma descum in March RIE		
13.. Copper oxide etch	Etch copper oxide off in Copper Plating solution for 3min, 2 x 2 min water rinse and immediately into nickel plating solution.		

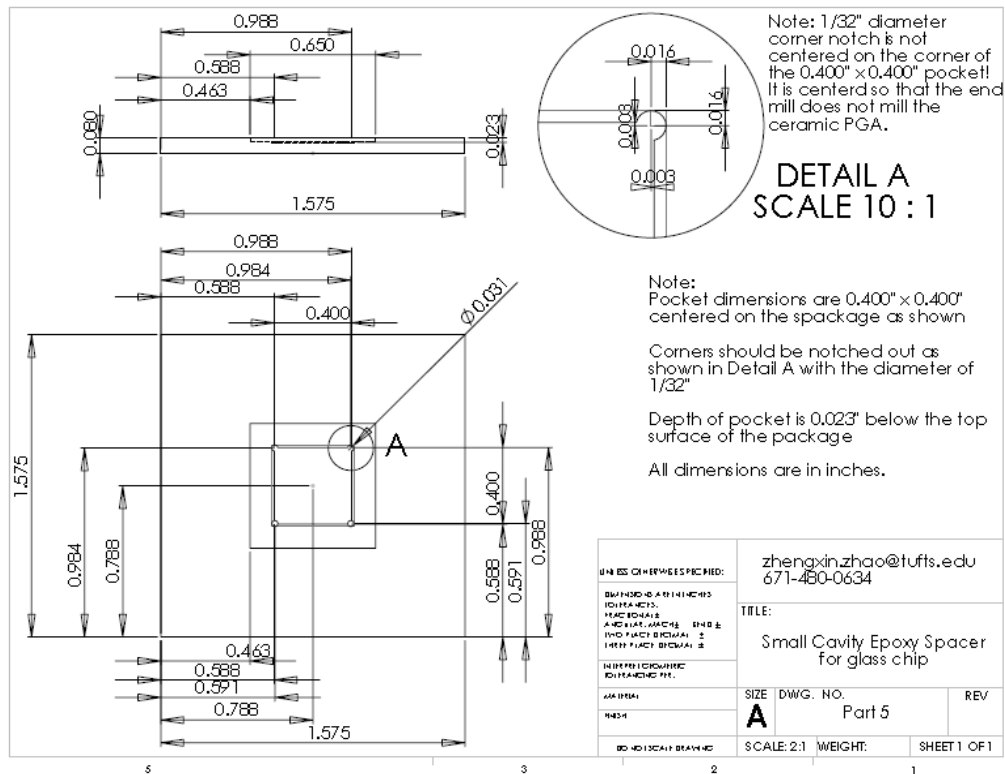
14. Copper Electroplating	Plate on thick Cu (filter). See Cu plating SOP. TECHNICAL COPPER FB BATH RTU, room temp, 5 mA/cm ² results in 150 nm/min. 2 x DI water rinse.	<u>Notes:</u> Wafer area = 78 cm ²	
15.. Strip Photoresist	5 minute acetone soak, 2 min IPA, 2 min x 2 water, air dry,		
16. O₂ Descum	200W, 120sec, 100% O ₂ (300 mT) in March RIE		
17. Lithography	HMDS/AZ9260, 500 rpm 5 sec spread, 1500 rpm 60 sec spin 115C 2.5 min softbake, 1 st : 80 sec EBR exposure, 7 min Develop, 2 nd : 19 exposure, 8~9 min develop, AZ400K:water 1:3, 2 x 2 DI water rinse, air gun dry	<u>Notes:</u> <u>1500 rpm = 9~10 um</u>	
18. O₂ Descum	150W, 30 sec, 100% O ₂ (280 mT) plasma descum in March RIE		
20. Copper oxide etch	Etch copper oxide off in Copper Plating solution for 3min, 2 x 2 min water rinse and immediately into nickel plating solution.		
21. Nickel Electroplating	Plate on thick Ni. See Ni plating SOP. NICKEL SULFAMATE SEMI BRIGHT RUT MECHANICAL AGITATION, 50C, 5 mA/cm ² results in 100 nm/min.	<u>Notes:</u> SM3 structure mask has an area of 30.74cm ²	
22. Strip Photoresist	10 minute acetone soak, 5 min IPA, 5 min water		
23. Lithography	HMDS/AZ9260, 500 rpm 5 sec spread, 800 rpm 60 sec spin 100C 3 min softbake, 1 st : 90sec EBR exposure, 6 min Develop (acetone swab 300 rpm as needed), 2 nd : 45 sec exposure (UV filter), 8-10 min develop, AZ400K:water 1:3, 2 x 2 DI water rinse, air gun dry	<u>Notes:</u> <u>800 rpm = 16 um</u>	

24. O₂ Descum	150W, 120 sec, 100% O ₂ (280 mT) plasma descum in March RIE		
25. Nickel Electroplating	Plate on thick Ni. See Ni plating SOP. NICKEL SULFAMATE SEMI BRIGHT RUT MECHANICAL AGITATION, 50C, 5 mA/cm ² results in 100 nm/min.	<u>Notes:</u> A current of 0.06A gives a rate of 200 nm/min	
26. Protect wafer	Spin on HMDS/AZ9245 at 2000 rpm, softbake 115C, 2 mins.		
27. Dice wafer	MA dicing saw – dice into individual dies		
28. Strip Photoresist	10 min acetone soak, 5 min IPA, 5 min x2 water		
29. O₂ Clean (If necessary)	200W, 120 sec, 100% O ₂ (280 mT) plasma clean in March RIE		
30. Copper Wet Etch (Release)	1:1:18 CH ₃ COOH: H ₂ O ₂ : Water 1 day, 10min x2 DI water rinse, IPA 10 min, Methanol 30 min, 2hr dry in drybox at reduced relative humidity.	RH in drybox during dry:	

Appendix C

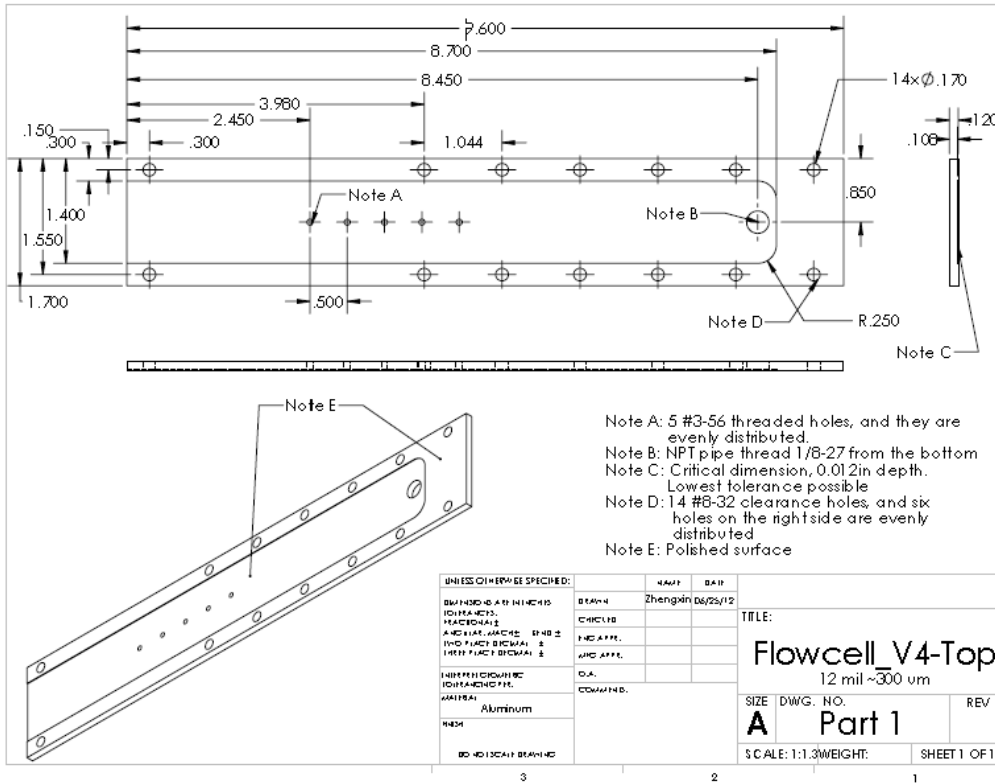
CAD Drawing

C.1 Cavity of CPGA Package (dimension in inch)

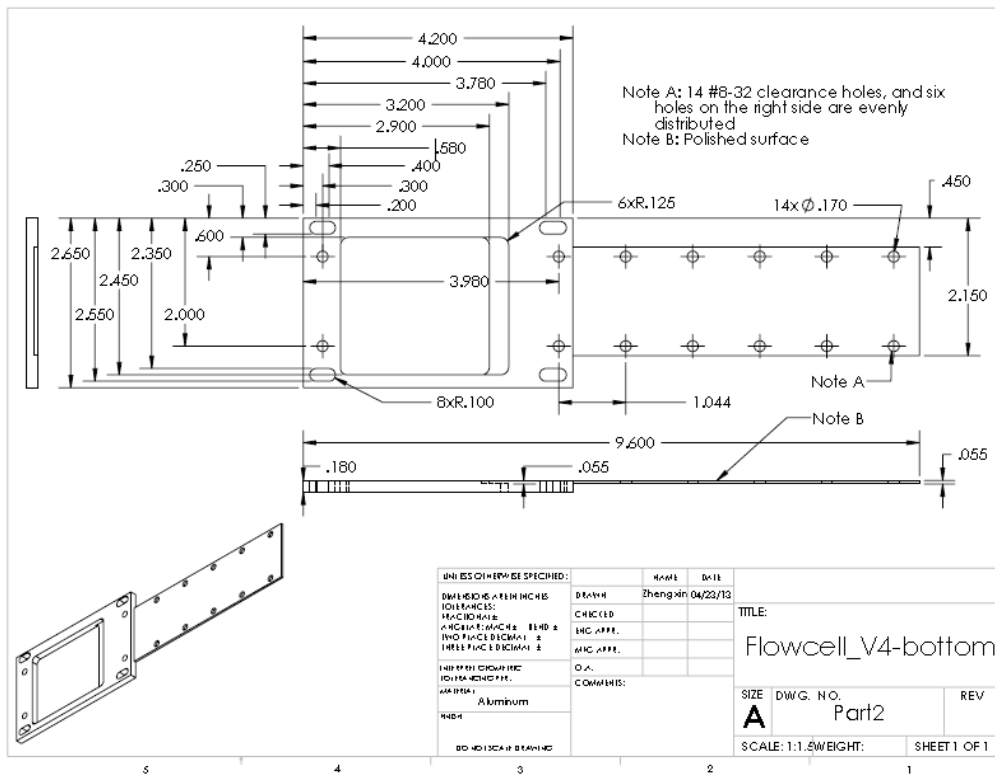


C.2 Flowcell cell (dimension in inch)

Top plate (300 μm high channel):



Bottom plate:



Appendix D

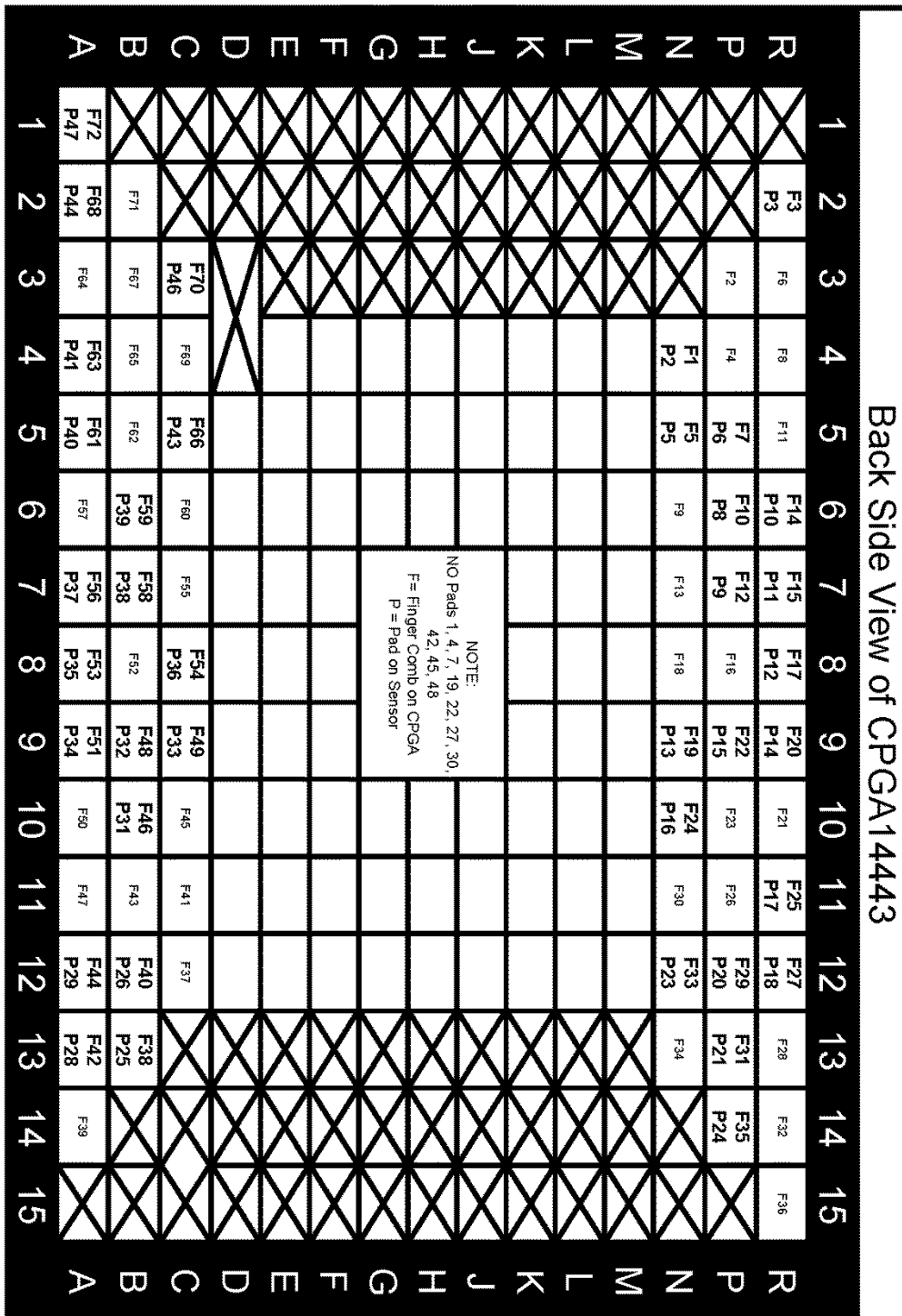
CPGA Pinout

D.1 CPGA pin to sensor group to chip pad

Package Pin	Sensor Group	Chip Pad		Chip Pad		Sensor Group	Package Pin
1	1,1	2	Top	Top	47	1,4	72
2							71
3		3	Bottom	Bottom	46		70
4							69
5	1,2	5	Top	Top	44	1,3	68
6							67
7		6	Bottom	Bottom	43		66
8							65
9							64
10	2,1	8	Top	Top	41	2,4	63
11							62
12		9	Bottom	Bottom	40		61
13							60
14	2,2	10	Com	Com	39	2,3	59
15		11	Top	Top	38		58
16							57
17		12	Bottom	Bottom	37		56
18							55
19	3,1	13	Com	Com	36	3,4	54
20		14	Top	Top	35		53
21							52
22		15	Bottom	Bottom	34		51
23							50
24	3,2	16	Com	Com	33	3,3	49
25		17	Top	Top	32		48
26							47
27		18	Bottom	Bottom	31		46
28							45
29	4,1	20	Top	Top	29	4,4	44
30							43
31		21	Bottom	Bottom	28		42
32							41
33	4,2	23	Top	Top	26	4,3	40
34							39
35		24	Bottom	Bottom	25		38
36							37

D.2 Pinout on the backside of CPGA.

Ridge is here



Bibliography

- [1] M. Sheplak, L. Cattafesta, T. Nishida and C. B. McGinley, "MEMS shear stress sensors: promise and progress," *24th AIAA Aerodynamic Measurement Technology and Ground Testing Conference, Portland, OR, 28 Jun –1 Jul, 2004.*, 2004.
- [2] J. W. Naughton and M. Sheplak, "Modern developments in shear-stress measurement," *Prog. Aerospace Sci.*, vol. 38, pp. 515-570, 2002.
- [3] L. Löfdahl and M. Gad-el-Hak, "MEMS-based pressure and shear stress sensors for turbulent flows," *Measurement Science and Technology*, vol. 10, pp. 665, 1999.
- [4] K. Winter, "An outline of the techniques available for the measurement of skin friction in turbulent boundary layers," *Prog. Aerospace Sci.*, vol. 18, pp. 1-57, 1979.
- [5] H. Fernholz, G. Janke, M. Schober, P. Wagner and D. Warnack, "New developments and applications of skin-friction measuring techniques," *Measurement Science and Technology*, vol. 7, pp. 1396, 1996.
- [6] C. Ho and Y. Tai, "Micro-electro-mechanical-systems (MEMS) and fluid flows," *Annu. Rev. Fluid Mech.*, vol. 30, pp. 579-612, 1998.
- [7] Y. J. Li, J. H. Haga and S. Chien, "Molecular basis of the effects of shear stress on vascular endothelial cells," *J. Biomech.*, vol. 38, pp. 1949-1971, 2005.
- [8] C. Tropea, A. L. Yarin and J. F. Foss, *Springer Handbook of Experimental Fluid Mechanics*. Springer, 2007.
- [9] T. Stanton, D. Marshall and C. Bryant, "On the conditions at the boundary of a fluid in turbulent motion," *Proceedings of the Royal Society of London. Series A*, vol. 97, pp. 413-434, 1920.
- [10] J. Preston, "The determination of turbulent skin friction by means of Pitot tubes," *Journal of the Royal Aeronautical Society*, vol. 58, pp. 109-121, 1954.
- [11] Link, "http://www.engineeringtoolbox.com/pitot-tubes-d_612.html," .
- [12] J. A. Schetz, "Boundary layer analysis," *NASA STI/Recon Technical Report A*, vol. 93, pp. 14688, 1993.

- [13] L. Tanner and L. Blows, "A study of the motion of oil films on surfaces in air flow, with application to the measurement of skin friction," *Journal of Physics E: Scientific Instruments*, vol. 9, pp. 194, 1976.
- [14] D. J. Monson, G. G. Mateer and F. R. Menter, "Boundary-layer transition and global skin friction measurement with an oil-fringe imaging technique," 1993.
- [15] D. Driver, "Application of oil-film interferometry skin-friction measurement to large wind tunnels," *Exp. Fluids*, vol. 34, pp. 717-725, 2003.
- [16] B. Van Oudheusden, "Silicon thermal flow sensors," *Sensors and Actuators A: Physical*, vol. 30, pp. 5-26, 1992.
- [17] L. Löfdahl, V. Chernoray, S. Haasl, G. Stemme and M. Sen, "Characteristics of a hot-wire microsensor for time-dependent wall shear stress measurements," *Exp. Fluids*, vol. 35, pp. 240-251, 2003.
- [18] E. Kävesten, C. Vieider, L. Löfdahl and G. Stemme, "An integrated pressure—flow sensor for correlation measurements in turbulent gas flows," *Sensors and Actuators A: Physical*, vol. 52, pp. 51-58, 1996.
- [19] R. J. Goldstein, *Fluid Mechanics Measurements*. Taylor & Francis, 1996.
- [20] R. Savelsberg, M. Schiffer, E. Obermeier and I. P. Castro, "Calibration and use of a MEMS surface fence for wall shear stress measurements in turbulent flows," *Exp. Fluids*, vol. 53, pp. 489-498, 2012.
- [21] T. von Papen, U. Buder, H. D. Ngo and E. Obermeier, "A second generation MEMS surface fence sensor for high resolution wall shear stress measurement," *Sensors and Actuators A: Physical*, vol. 113, pp. 151-155, 2004.
- [22] T. Von Papen, H. Steffes, H. Ngo and E. Obermeier, "A micro surface fence probe for the application in flow reversal areas," *Sensors and Actuators A: Physical*, vol. 97, pp. 264-270, 2002.
- [23] M. A. Schmidt, R. T. Howe, S. D. Senturia and J. H. Haritonidis, "Design and calibration of a microfabricated floating-element shear-stress sensor," *Electron Devices, IEEE Transactions on*, vol. 35, pp. 750-757, 1988.
- [24] T. Pan, D. Hyman, M. Mehregany, E. Reshotko and S. Garverick, "Microfabricated shear stress sensors, part 1: design and fabrication," *AIAA J.*, vol. 37, pp. 66-72, 1999.

- [25] D. Hyman, T. Pan, E. Reshotko and M. Mehregany, "Microfabricated shear stress sensors, Part 2: Testing and calibration," *AIAA J.*, vol. 37, pp. 73-78, 1999.
- [26] M. P. Patel, E. Reshotko and D. Hyman, "Microfabricated shear-stress sensors, Part 3: Reducing calibration uncertainty," *AIAA J.*, vol. 40, pp. 1582-1588, 2002.
- [27] J. Zhe, V. Modi and K. R. Farmer Jr, "A microfabricated wall shear-stress sensor with capacitive sensing," *Microelectromechanical Systems, Journal of*, vol. 14, pp. 167-175, 2005.
- [28] V. Chandrasekharan, J. Sells, J. Meloy, D. P. Arnold and M. Sheplak, "A Microscale Differential Capacitive Direct Wall-Shear-Stress Sensor," *Microelectromechanical Systems, Journal of*, vol. 20, pp. 622-635, 2011.
- [29] V. Chandrasekharan, J. Sells, J. Meloy, D. Arnold and M. Sheplak, "A metal-on-silicon differential capacitive shear stress sensor," in *Solid-State Sensors, Actuators and Microsystems Conference, 2009. TRANSDUCERS 2009. International*, 2009, pp. 1537-1540.
- [30] J. Shajii, K. Ng and M. A. Schmidt, "A microfabricated floating-element shear stress sensor using wafer-bonding technology," *Microelectromechanical Systems, Journal of*, vol. 1, pp. 89-94, 1992.
- [31] A. A. Barlian, S. Park, V. Mukundan and B. L. Pruitt, "Design and characterization of microfabricated piezoresistive floating element-based shear stress sensors," *Sensors and Actuators A: Physical*, vol. 134, pp. 77-87, 2007.
- [32] A. Padinanabhan, H. Goldberg, K. Breuer and M. Schmidt, "A SILICON MICROMACHINED FLOATING-ELEMENT SHEAR-STRESS SENSOR 'WITH OPTICAL POSITION SENSING BY PHOTODIODES,'" 1995.
- [33] A. Padmanabhan, H. Goldberg, K. D. Breuer and M. A. Schmidt, "A wafer-bonded floating-element shear stress microsensor with optical position sensing by photodiodes," *Microelectromechanical Systems, Journal of*, vol. 5, pp. 307-315, 1996.
- [34] A. Padmanabhan, M. Sheplak, K. Breuer and M. Schmidt, "Micromachined sensors for static and dynamic shear-stress measurements in aerodynamic flows," in *Solid State Sensors and Actuators, 1997. TRANSDUCERS'97 Chicago., 1997 International Conference on*, 1997, pp. 137-140.
- [35] Link, "http://en.wikipedia.org/wiki/Boundary-layer_thickness," .

- [36] Link, "http://www.cortana.com/Drag_Description.htm," .
- [37] F. M. White, *Viscous Fluid Flow*. McGraw-Hill Higher Education, 2006.
- [38] G. Zilliac, T. Pulliam, M. Rivers, J. Zerr, M. Delgado, N. Halcomb and H. Lee, "A Comparison of the Measured and Computed Skin Friction Distribution on the Common Research Model," *AIAA Paper*, vol. 1129, 2011.
- [39] T. Pan, D. Hyman, M. Mehregany, E. Reshotko and B. Willis, "Characterization of microfabricated shear stress sensors," in *Instrumentation in Aerospace Simulation Facilities, 1995. ICIASF'95 Record., International Congress on*, 1995, pp. 6/1-6/7.
- [40] Link, "http://en.wikipedia.org/wiki/Couette_flow," .
- [41] Y. Chen and E. Reshotko, "Study of flow around a MEMS shear-stress sensor element," in *APS Division of Fluid Dynamics Meeting Abstracts*, 2001, .
- [42] N. Kastor, Z. Zhao and R. D. White, "Modeling of a MEMS Floating Element Shear Sensor," *In the Proceedings of the Materials Research Society, MRS Fall Meeting*, 2013.
- [43] J. R. Burns, R. D. White and J. S. Krause, "Low profile packaging for MEMS aero-acoustic sensors," in *MRS Proceedings*, 2012, pp. mrsf11-1415-tt01-03.
- [44] J. Luo, A. Flewitt, S. Spearing, N. Fleck and W. Milne, "Young's modulus of electroplated Ni thin film for MEMS applications," *Mater Lett*, vol. 58, pp. 2306-2309, 2004.
- [45] C. Mastrangelo, "Adhesion-related failure mechanisms in micromechanical devices," *Tribology Letters*, vol. 3, pp. 223-238, 1997.